ABSTRACT

Title of Document: RESPONSE AND DURABILITY OF LARGE
RADIUS OF GYRATION STRUCTURES
SUBJECTED TO BIAXIAL VIBRATION

Matthew Ross Ernst, Master of Science, 2013

Directed By: Dr Abhijit Dasgupta,
Department of Mechanical Engineering

Multiaxial vibration tests were conducted using an electrodynamic shaker capable of controlled vibration in six degrees-of-freedom. The test specimen consisted of six large inductors insertion mounted on a printed wiring board. Average damage accumulation rate was measured for random excitation in-plane, out-of-plane, and both directions simultaneously. Under simultaneous biaxial excitation, the damage rate was found to be 2.2 times larger than the sum of the in-plane and out-of-plane rates. The conclusion was that multiple-step single-degree-of-freedom testing can significantly overestimate the durability of some structures in a multiaxial environment.

To examine the mechanics behind this phenomenon, the response of a simple rod structure was analyzed with the finite element method. Axial vibrations, which produce negligible stress on their own, were found to contribute significant additional stress when combined with transverse vibration.   This additional stress contribution was found to be highly dependent on the frequency ratio and phase relationship between the two participating axes.

RESPONSE AND DURABILITY OF LARGE RADIUS OF GYRATION
STRUCTURES SUBJECTED TO BIAXIAL VIBRATION

By

Matthew Ross Ernst

Thesis submitted to the Faculty of the Graduate School of the
University of Maryland, College Park, in partial fulfillment
of the requirements for the degree of
Master of Science
2013

Advisory Committee:
Professor Abhijit Dasgupta, Chair
Professor Sung Lee
Professor Bongtae Han

Dedication

I dedicate this thesis to my wife who has supported my decision to pursue further studies, encouraged me along the way, and put up with more than one day of screaming kids and dirty diapers to make it possible.

Acknowledgements

I want to acknowledge the many people and groups whose contributions made this thesis possible.

My advisor, Professor Abhijit Dasgupta, is responsible for laying much of the groundwork for this thesis long before I became his student. Without his involvement it is hard to imagine all the people, equipment, and funding being pulled together to accomplish it. In addition, he spent countless hours in discussions with me, reviewing results, editing drafts and critiquing presentations.

A Ph.D. student of Dr. Dasgupta's and Engineer at the Army Research Laboratory, Ed Habtour, originally worked on this project before his research focus shifted. He designed the test specimen and obtained agreement from the interested parties on the original test matrix. He also provided me with the instruction necessary to operate the TEAM Tensor shaker table and we jointly conducted the initial (Fall) round of durability tests. Throughout the latter stages of this project Ed has continued to provide me with great advice and counsel.

In addition to Dr. Dasgupta and Ed, the entire A-team (Dr Dasgupta's research group) provided an untold number of quick consultations concerning the project and at least as many laughs around the office.

Table of Contents

Appendix A TE6-900 Vibration Test System Specifications

Appendix B Lead Temperature Rise during Testing

Appendix C Response Data

Appendix D Modeling a Random Vibration Boundary Condition

Appendix E MATLAB script for generating a time domain vibration signal from a PSD definition and random phase assumption.

Appendix F Computational Strategies to Minimize Transient Response during Time-Domain Analysis of Structures under Vibratory Loading

Appendix G A Description of the Test Specimen Finite Element Model

Bibliography

List of Tables

List of Figures

1. Introduction

1.1 Background

Electronic assemblies often serve in environments subject to vibratory loading. These vibratory loads can cause failures due to fatigue damage accumulation in critical components such as structural elements or component electrical interconnections. It is therefore critical for engineers to be able to accurately assess the damage accumulation rate due to vibration-induced fatigue to verify adequate reliability over a product's lifetime. Commonly, vibration shakers are employed during product development to assess reliability and ensure product safety before it enters production or service. Until recently, test labs using electro-dynamic (ED) shakers have been restricted to single-axis-at-a-time methods due to a lack of multiple-axis test equipment. Still today, many consider newly available multiple degree-of-freedom ED test equipment too expensive. The repetitive–shock (RS) shakers used for combined temperature-vibration highly accelerated life testing (HALT©) do produce excitation along multiple axes at an affordable cost, but their PSD profile (spectral content) is not controllable along even one axis, let alone along multiple independent axes. This study therefore focuses only on ED shakers and compares multiple-step single-axis-at-a-time test methods with true simultaneous multiple-axis test methods.

1.2 Literature Review

The military standard for vibration testing is MIL-STD-810G [1]. MIL-STD-810G method 514.6 details general guidelines for single exciter (single axis) testing. It gives procedures for a variety of vibration test types (stress screens, durability tests,

acceptance tests, etc), best practices for combining vibrations tests with other test methods, as well as typical vibration profiles for common classes of military vehicles and situations. Use of the sequential uniaxial vibration testing is generally accepted in the standard. Method 527, which is new in the most recent revision of the standard, details guidelines for multiple-exciter testing including simultaneous multiple axis testing. In this revision, the scope of Method 527 is still very limited. With respect to multiple axis testing, the document establishes terminology and general test procedures, but makes no attempt to specify when multiple axis methods should be employed instead of single axis methods, other than to say it should be used when the dynamic environment is "defined in more than a single-degree-of-freedom (SDOF)."

The only commercial standard requiring multiaxial testing is IEEE 344 [2]. This standard governs the seismic testing of components used in nuclear power plant construction. It requires biaxial excitation of the object during seismic event testing.

The most applicable Society of Automotive Engineers standard concerning environmental vibration testing of electronic components is the Handbook for Robustness Validation of Automotive Electrical/Electronic Modules, SAE J1211 [3]. Previous versions of this standard, which are now included in SAE J2837 [4], provided typical vibration environments for common vehicle locations. The standard primarily addressed the identification of intermittent/electrical contact failures due to vibration rather than durability/fatigue failures. The 2009 version of the standard [3]

was drastically changed to address a change in approach to reliability within the industry. The standard now primarily addresses how to define an application profile and design for robustness rather than test for robustness. As a result most of the specific test guidance has been removed.

ISO 16750-3 [5] provides road vehicle vibration test specifications similar to SAE J2837 [4]. It directly states tests should be "performed in each plane of the device under test".

The U.S. Navy has published a document which addresses manufacturing screening procedures for electronic components and systems. These procedures can be found in NAVMAT P-9492 [6]. One section is dedicated to vibration testing. It gives specific findings for the type, level and duration of vibration screening which were found to be most effective for discovering defective components in electronic assemblies.

Several papers have addressed multiple-degree-of-freedom (MDOF) test equipment in general and their ability to accurately replicate a specified environment. Habtour et al [7] provided a literature review of the current status of multiaxial vibration testing and a comparison of several shaker technologies including hydraulic, repetitive shock (RS) and electro-dynamic (ED) technologies. It referenced work by Choi et al [8] who compared vibration response to MDOF ED shaker excitation to those obtained from a repetitive shock (RS) shaker typically used in industry for screening electronic product designs. They discussed the advantages of being able to

control the spectral profile and coherence between axes in an ED shaker. On the other hand, the RS shaker focuses most of its energy at higher frequency levels, thus making it valuable for stiff and light test specimens. Smallwood and Gregory [9] provided an evaluation of the MDOF shaker used for the tests reported in this thesis. They concluded the Tensor TE6-900 shaker was adequate for testing small components in multiple axes up to useful levels. Their evaluation of the shaker table provides increased confidence in the results of the experimental work in this thesis.

Several researchers have noted the limitations of the multiple-step uniaxial vibration method. These include Himelblau et al [10], Whiteman and Burman [11], French et al, [12] Gregory et al [13], and Habtour et al [14].

Himelblau et al [10] performed experiments on a specially-designed shaker table capable of multiaxial translational motion. They compared the response of a critical component in a large aerospace electronics assembly under single axis and simultaneous multiaxial vibration conditions. Stress spectrums were computed from the measured responses. A fatigue model was employed which utilized the stress spectrum and an S-N curve to compare the damage accumulation between the multiaxial test and the summation of damage under three orthogonal uniaxial tests. They concluded that simultaneous tri-axial excitation would cause approximately twice as much damage as the multi-step single-axis-at-a-time excitation.

In 2002, Whiteman and Burman [11] conducted experimental work on the same test equipment as Himelblau et al [10]. Their test specimens were simple notched aluminum cantilevered beams. They reported significant differences in time-to-failure between the simultaneous multiaxial test method and the multi-step single-axis-at-a-time method. Additionally, they conducted experiments to analyze the effect of test order on the single-axis-at-a-time method. Their results were surprising in that they reported pre-testing the beam with axial vibration increased the durability under transverse vibration.

French et al [12] also conducted MDOF experiments on notched cantilevered beam specimens. They found the specimens failed after a mean time of 760 seconds under simultaneous biaxial vibration. When vibration was applied sequentially in each axis, the specimens only survived a mean time of 536 seconds in the second axis after 760 seconds in the first axis. Thus it was concluded that the multi-step uniaxial test resulted in different time-to-failure results than simultaneous multiaxial testing. This differed from previous tests in that multiple uniaxial tests were found to be more damaging than the simultaneous multiaxial test. Also, they found that multi-step uniaxial excitation produced different crack propagation patterns than simultaneous multiaxial excitation.

Gregory et al [13] performed tests on a beam with lumped mass structure using a MDOF shaker very similar to the one used in this thesis to examine the response under single and multi-axis inputs. In addition they performed linear finite element

analysis (FEA) of the structure. Their experimental work showed significant differences in the magnitude, location and direction of the acceleration and strain measured in the beam. These results all indicate that multiaxial vibration could initiate failure modes which would not be present during single-axis vibration.

Ayen and Çelik [15] performed a frequency domain finite element analysis of an aircraft structural element subject to vibration fatigue. They analyzed the FEA results using the rainfall approach and showed that damage accumulation was 30-70% greater, depending on location, for multiaxial vibration. Since this was based purely on a linear FEA analysis, the increase in damage rate was solely due to some locations experiencing stresses under both load conditions. The multiaxial fatigue analysis accounts for the summation of these stresses while the uniaxial method does not. They concluded that simultaneous multiaxial application of vibration would greatly improve test realism.

The experimental work in this thesis builds upon previous experimental work in [11], [12] and [13] by demonstrating the inadequacy of the multi-step single-axis-at-a-time testing method for realistic electronic packages. Furthermore, this thesis uses finite element modeling techniques to understand the effects of multi-axis vibration on the response magnitudes and stress levels observed in simple structures. It improves upon previous FEA work in this area by performing the FEA work in the time-domain where non-linearity can be accommodated.   In doing so, it studies the extent to which geometric non-linearity could contribute to the cross-axis synergy in the

response and durability results under MDOF excitation. The nonlinear interactions

between the responses along different axes are shown to explain one reason why the

simultaneous MDOF response is greater than the sum of the individual SDOF

responses. The sum of the experimental and modeling results are useful for

establishing new guidelines on when vibration test methods utilizing uniaxial test

equipment to approximate damage accumulation in multiaxial environments should

be rejected in favor of test methods utilizing test equipment capable of true

simultaneous multiaxial vibration.

2. Durability Test Set-up

Section 2 will present the test set-up. Later sections will present the characterization

of the specimen response and durability results for MDOF excitation.

2.1 Test Specimen Description

This section will describe the test specimen, its fixturing, and instrumentation.

2.1.1 Physical Design
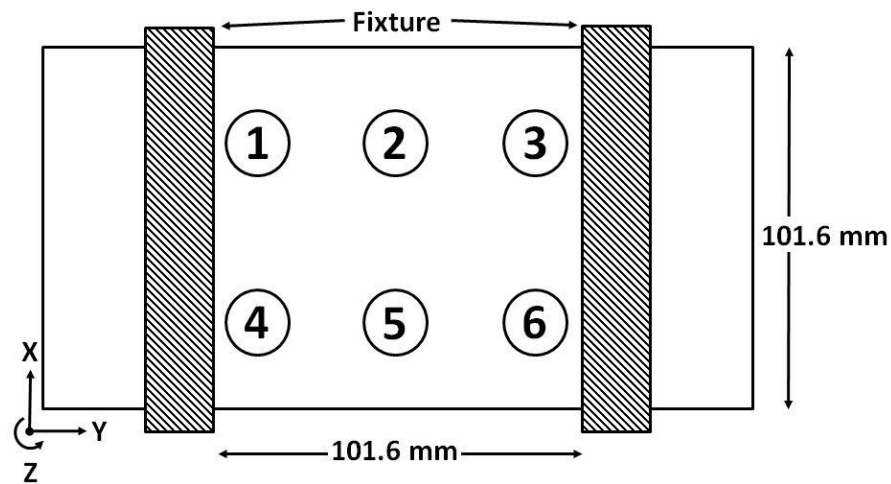
Figure 1: Test Specimen Schematic

The specimen under test was a printed wiring assembly (PWA) comprised of a four

layer FR-4 fiberglass/epoxy circuit board with six insertion mounted inductors.

Figure 1 shows the dimensioned layout of the assembly with component labels and a

XYZ coordinate system for reference. This reference system and component

numbering scheme are used throughout this document. The sensors shown in Figure 1

are discussed in detail later in Section 2.2.2. The inductors were mounted to the

circuit card such that the two connection points were oriented along the Y axis. This

resulted in the components being less stiff in the X direction than the Y direction.

SAC305 solder was used for the interconnects.

Figure 2: External View of Inductor
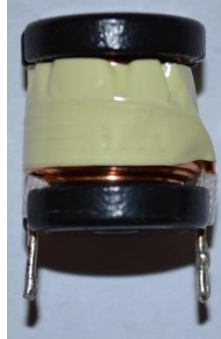
Figure 3: Inductor with Shrink Wrap Removed
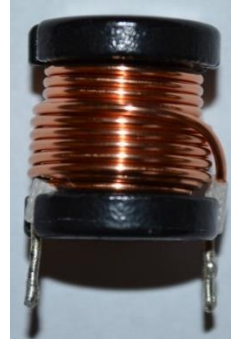
Figure 4: Inductor with Tape Wrap Removed
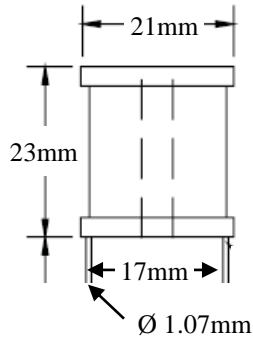
Figure 5: Inductor Dimensions

Figure 6: Outside Wrap of Coil (Stiff Lead)
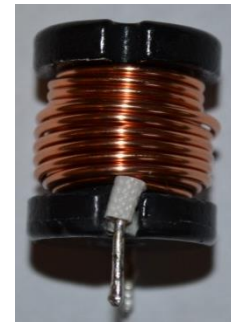
Figure 7: Inside Wrap of Coil (Compliant Lead)

Details of the inductor construction can be seen in Figure 2 through Figure 7. The

inductors were Bornes 5604-RC type inductors, weighing approximately 23 grams

each, and composed of 1.07 mm film insulated copper wire wound around a ferrite

bobbin core. Additionally, small insulating sleeves were around the copper wire

where it exited the bobbin. Adhesive tape was wrapped around the copper windings

and shrink wrap tubing covered the outside of the inductor. Figure 6 and Figure 7

show that the wire coil winding created an asymmetry in the construction which was

not immediately apparent before the physical tear-down of the component. The effect

of this was to form lead junctions of different stiffness. The lead corresponding to the outside coil wrap was held tightly in place by the shrink wrap while the inner coil wrap was relatively unrestrained, creating a comparatively compliant lead. These lead stiffness differences are discussed in detail in Appendix G.

2.1.2 Fixturing and Instrumentation
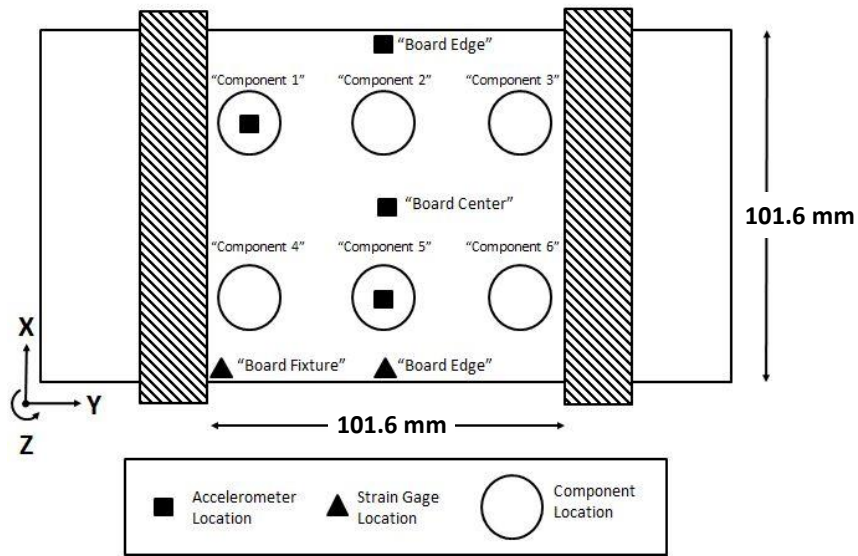
Figure 8: Diagram of Durability Specimen with Sensors Labeled
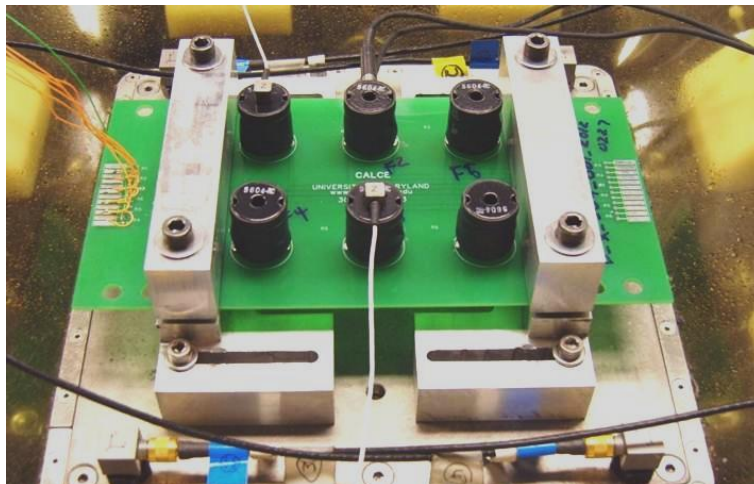
Figure 9: Photograph of the Durability Specimen on Shaker Table

The circuit card was rigidly clamped to the shaker table along two edges with aluminum fixture clamps. The unsupported span between the clamps was 101.6 mm. A torque of 15 N-m was used on each of the four screws holding the clamp. The inductors were electrically connected to pads on the edge of the card to allow monitoring of interconnect resistance during the tests. Eight tri-axial accelerometers were used during the tests. To monitor and control excitation, four Dytran 3263A2T accelerometers were mounted on the table top at the four corners. Components one and five each had a Dytran 3133A3 accelerometer mounted on the top center of the component body. Additionally, Dytran 3243M2 accelerometers were mounted on the bottom-side center of the board and top-side rear edge of the board. Figure 8 shows a labeled schematic and Figure 9 shows a photo of the test specimen mounted on the shaker table.

2.1.3 Mode Shapes and Frequencies
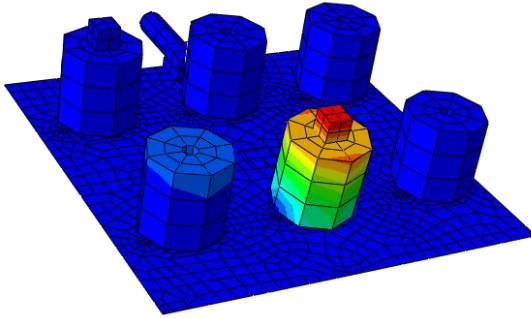
Figure 10: Vibration Mode I (68-90 Hz)
Modes II-VI similar for each component
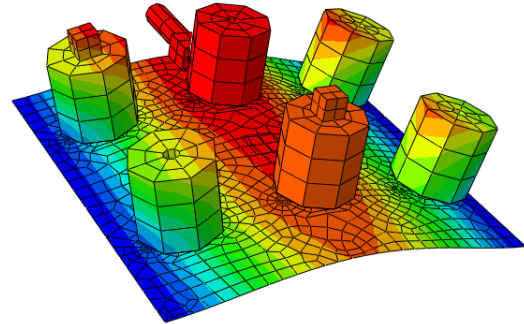
Figure 11: Vibration Mode VII (176 Hz)
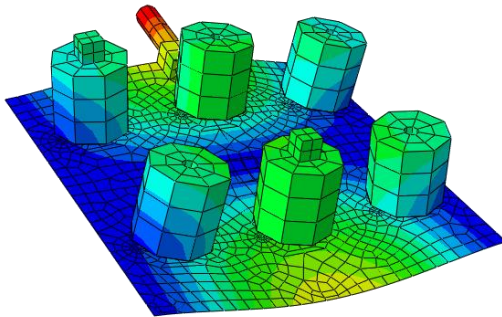
Figure 12: Vibration Mode VIII (214 Hz)
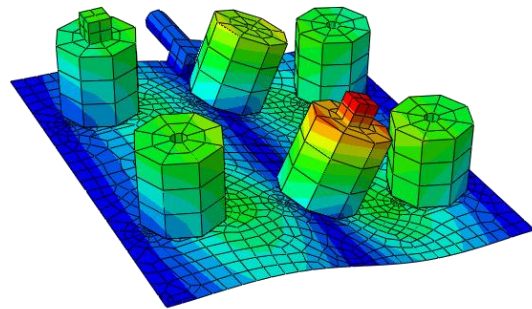
Figure 13: Vibration Mode IX (387 Hz)

Simple finite element models were developed to conduct an approximate modal analysis. Details of the model are presented in Appendix G. The FEA results show that the first six vibration modes of the specimen are deflection of each component in the X direction. Each component had a slightly different frequency.   A depiction of one of these modes which is similar to the other five is shown in Figure 10. As described later in Section 3.2.1, the measured frequency of these modes was generally between 68 and 90 Hz, although the exact frequency depended on several factors including component location on the card, presence of an accelerometer on top, manufacturing variability, and damage accumulated in the lead. Modes VII and VIII of the system corresponded to [0,2] transverse bending of the board and [1,2] twisting of the board as shown in Figure 11 and Figure 12. The corresponding modal

13

frequencies were measured to be approximately 176 Hz and 214 Hz. The next higher

mode of the system is a [0,3] mode as shown in Figure 13. The response frequency

for this mode was seen through FEA to be approximately 387 Hz and was above the

frequency range of the input excitation, as discussed later. Since this was above the

input excitation maximum frequency, no excitation of this mode or higher order

modes was observed. Details of the experimental response can be found in Section 3.

2.3 Test Equipment Description

Figure 14: TEAM TENSOR TE6-900 Shaker Table
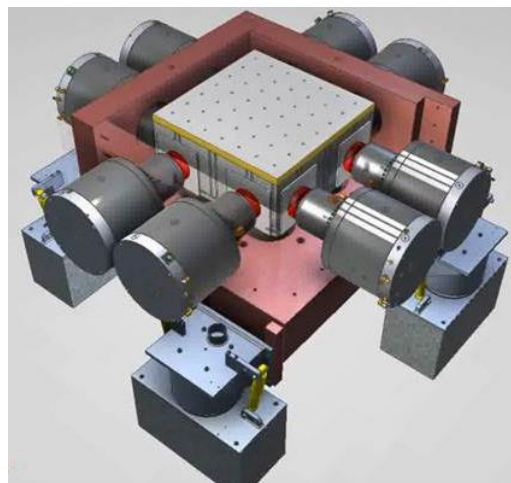
Figure 15: Schematic of TEAM TENSOR TE6-900 Shaker Arrangement†

†Image used with the permission of Team Corporation. Design covered by multiple patents.

Testing was performed on a TEAM Corporation TENSOR TE6-900 six degree-of-freedom shaker table as shown in Figure 14. Four electrodynamic shakers are used in each of the three orthogonal axes to drive an 8" x 8" table. An exploded view of the shaker arrangement is shown in Figure 15. This table was capable of producing controlled motion in all 6 rigid body modes. However, during the testing conducted for this thesis, only translational motion in two of the axes (X and Z) was used in order to reduce test complexity.

Each of the orthogonal directions within the plane of the table used two opposed sets of shakers. The out-of-plane direction placed all four shakers under the table with a system of pre-tensioned elastic cords to oppose the out-of-plane shakers. This design resulted in very good isolation of the in-plane motion from the out-of-plane motion, but less isolation of the out-of-plane motion from the in-plane. Approximately 20% of the motion from the in-plane direction was transferred to the out-of-plane direction versus less than 1% transferred from the out-of-plane direction to the in-plane direction. As a result, low levels of out-of-plane motion could not be completely eliminated during in-plane testing. Further information on the TEAM Corporation TE6-900 shaker table is available in Reference [16] and Appendix A. Control, data acquisition and in-test monitoring was conducted using a Data Physics Abacus$^{©}$ data acquisition unit and Signal Star$^{©}$ software.

2.4 Experiment Design

This section will address the vibration profile and test matrix design.

    2.4.1 Excitation Profile

The random vibration excitation levels used for the durability test were based on the electronics screening profile recommended in the U.S. Navy's manufacturing screening program document NAVMAT P9492 [6]. This profile's frequency range was modified to better accommodate the test specimen and project goals. The original NAVMAT profile called for vibration up to 2000 Hz. In order to reduce the complexity of the test article's response, the excitation profile in this study (CALCE profile) was truncated at 320 Hz, with a roll-off starting at 250 Hz. The purpose was to limit the response to the first three modes (one component deflection mode and two PWB deflection modes, shown earlier in Figures 10-13). The power spectral density (PSD) function for the NAVMAT P9492 profile and the durability test profile can be seen in Figure 16. This profile was applied according to the specifications of the next section. Total G_{rms} from 20Hz to 320Hz for the CALCE profile was 3.14 G_{rms}. For clarity, Table 1 specifies the break points for the profile used.
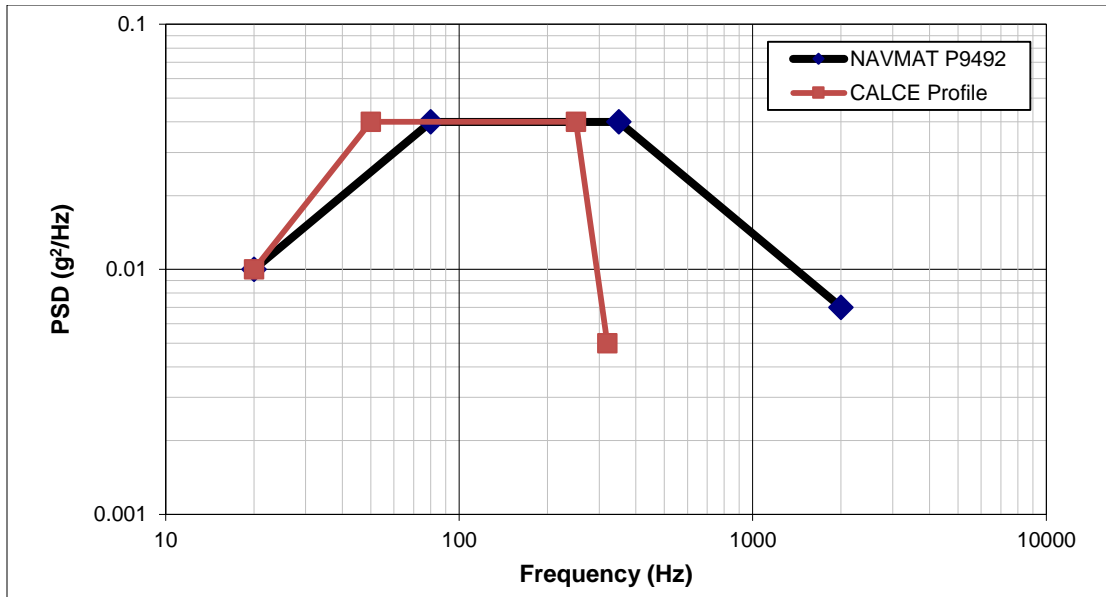
Figure 16: Vibration Power Spectral Density Functions

Table 1: Input PSD Break Points

Frequency (Hz)	PSD (g^2/Hz)
20.0	0.010
50.0	0.040
250.0	0.040
320.0	0.005

2.4.2 Test Matrix

The test matrix was designed to investigate two commonly used vibration test methods using single axis test equipment to simulate damage accumulation in a multiaxial environment. The first method was the multi-step single-axis-at-a-time application of vibration. The second method was the vector summation of each of the orthogonal components.

The first method to approximate an MDOF environment on SDOF equipment requires a vibration environment specification in three orthogonal translational components. Specifications like this for various environments are common in

standards such as MIL-STD 810G [1] or can be easily measured in the use environment using a single tri-axial accelerometer. The test is conducted in three steps using each of these three profiles one-at-a-time. In between tests, the specimen under test is re-fixtured to change the orientation with respect to the table. In this way the same SDOF table can be used to perform each of the three required orthogonal excitations. This method assumes that the damage caused by each of the orthogonal components of vibration is independent. This assumption of independence may be acceptable for some structures, but not in all cases. Despite this known limitation, this test method remains the mainstay of dynamic testing because of the lack of cost-effective MDOF test equipment. From a durability testing perspective one must be concerned with how close the results of multi-step single-axis-at-a-time testing are to the results of simultaneous MDOF testing. To answer this question, this study will conduct tests to study the average damage accumulation rate under single axis vibration with the rate under simultaneous MDOF vibration, for two selected orthogonal axes. The summation of damage rates under independent single axis vibration will be compared to the damage rate under simultaneous MDOF vibration.

The second method to approximate an MDOF environment on SDOF equipment sums the three orthogonal components of the PSD as if they were vectors producing a resultant PSD. In general this produces a different PSD magnitude and direction for each frequency value. If the three orthogonal component PSDs are scalar multiples of each other, then the resultant direction is the same for all frequencies. In this case,

the resultant magnitude of the PSD becomes the new PSD magnitude to be applied and the resultant direction determines the relative angle between the test specimen and the shaker table. The first limitation of this method is that profile specifications must be modified to meet the requirement that each axis PSD must be a scalar multiple of the others. In order to maintain a conservative approach, additional energy will need to be provided at some frequency intervals to create suitable PSD profiles. The second limitation is that performing the test in this manner is tantamount to forcing absolute coherence between the three orthogonal components of the PSD. The primary question prompted by this method concerns how damage under coherent vibration compares to damage under incoherent vibration. To answer this question two-axis combined durability tests were conducted in this thesis with low coherence and high coherence between the axes and the results will be compared.

The test matrix for this test is in Table 2. It consists of four different tests. Two replicates of each test were originally planned; however, due to test specimen limitations only one combined coherent test was conducted.

Table 2: Test Conditions Matrix

Single-Axis Testing		
Axis		**Duration**
In-Plane		Until Failure
Out-of-Plane		Until Failure
Simultaneous Testing		
Axis	**Minimum Coherence**	**Duration**
Combined	0.1 (Random)	Until Failure
Combined	0.9 (Coherent)	Until Failure

2.5 Test Procedures

The shaker and control/measurement equipment were configured according to the equipment standard operating procedure. When a profile was not specified on an axis, the corresponding shaker amplifiers were turned off. During testing this appeared to produce less cross-axis vibration in those directions compared to when the amplifiers were on with no profile specified.

When the table was started, vibration was increased in increments starting at -12 dB relative to the full durability profile of 3.14 G_{RMS}. Increments were at -12 dB, -10 dB, -6 dB, -3 dB and finally the full level of 3.14 G_{RMS} (0 dB). Increment steps were taken at the operator's discretion. Generally, less than 10 seconds elapsed at each increment while the operator monitored the system for proper operation. Only the time spent at the full vibration level was reported.

Failure was defined as a break in continuity of the electrical connection between the circuit card and component body. During the test this was monitored and logged using an Agilent data logger. In all cases failure was unambiguous.

During the first replicate of tests [17], cards were tested until the first component failed. During the second replicate of tests, cards were tested until all six original components failed. When a component failed, the shaker table was paused; the failed component was de-soldered and removed from the card. To preserve the dynamics of the card, a new component was re-soldered in its place to preserve the dynamic

20

characteristics of the test specimen. With the failed component replaced, the table

was restarted and the test continued until another component failed. This process was

repeated until all six original components had failed. Durability time for each

component was recorded as the total time the table was at full operating level until

loss of electrical continuity of that component. Time during the component

replacement was not included in the durability time.

One concern with the stop and re-start test technique was the effect of vibration

induced heating in the component lead. In order to examine the heating of the lead

during the test, an experiment was performed to measure the temperature rise during

testing. This test is documented in Appendix B. Total temperature rise observed was

less than 3 degrees Celsius over 45 minutes. This is considered small enough to not

have an effect on response or durability.

3. Experimental Characterization of Test Specimen Response

3.1 Background

In order to examine the response of the test specimen under different combinations of vibration, one board was instrumented with strain gages and accelerometers and used for characterization testing. This single test specimen was subjected to the test conditions specified in Table 3. Two test levels were used. One profile consisted of the vibration PSD specified in Figure 16; to examine the presumably non-linear test specimen response during the durability test. A second test used a PSD profile of the same shape, but with the amplitude reduced by -12 dB; to examine the presumably linear response of the system. All characterization tests were conducted on the same equipment as the durability tests. In addition to the accelerometers noted in Section 2.2.2, two strain gages were affixed to the board in the locations noted in Figure 8. At least 30 seconds of data were recorded for each test condition. The test specimen was subjected to less than 10 total minutes of testing. Less than half of this time was spent at the full vibration level. Total characterization times were minimized in order to minimize effects of accumulated damage on the response characteristics.

Table 3: Characterization Test Conditions

Test Number	Vibration Direction	Level
1	In-Plane Only	-12
2	In-Plane Only	0 dB
3	Out-of Plane Only	-12
4	Out-of Plane Only	0 dB
5	Combined (Random)	-12
6	Combined (Random)	0 dB

3.2 Experimental Response

A complete set of power spectral density plots for the response of each accelerometer in each axis is given in Appendix C. Specific data from these plots are presented in this section to highlight certain discoveries. Additionally, Appendix C contains a summary of board strain statistics measured during response characterization.

3.2.1 Vibration Modes and Frequencies

As discussed earlier in Section 2.2.3, the first response mode of the system was deflection of the inductor in the X direction. This response is most clearly displayed in the PSD of the X response of either instrumented component. The plot for Component 1 is shown in Figure 17. The response amplitude is clearly larger for the simultaneous MDOF response than for the single-axis response. Furthermore, the response frequency is observed to be slightly lower for simultaneous MDOF loading than for single axis loading. The author believes this frequency shift is due to a number of non-linear factors including damping due to air drag, plasticity in the leads, and large deformations, which are all functions of response magnitude rather than the loading type (SDOF vs MDOF). This trend is evident when considering the same vibration type at two different levels, as shown in a logarithmic scale in Figure 18. In this plot, it is clear that the peak response frequency shifts down as the amplitude of the response increases.
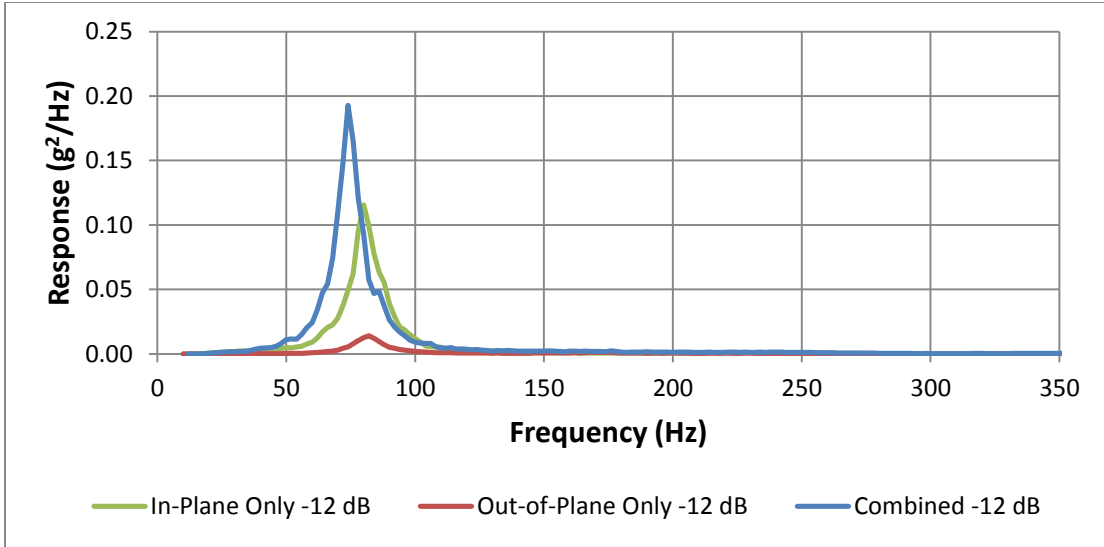
Figure 17: Component 1 X response Under Three Vibration Conditions at -12 dB
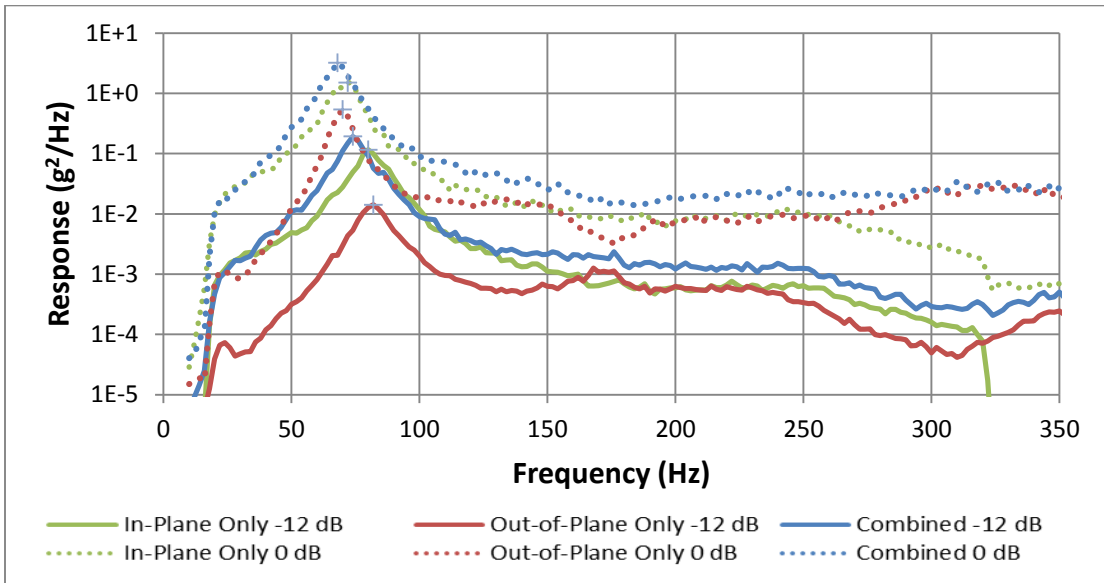
Figure 18: Comparison of X-Response PSDs for Component 1, Showing Drop of Response Frequency with Increase in Level of Excitation

The second natural frequency of the system can most clearly be seen by examining the PSD response of the board's center under out-of-plane vibration shown in Figure 19. A clear peak is seen at 176 Hz for out-of-plane and combined vibration under the -12db load condition.
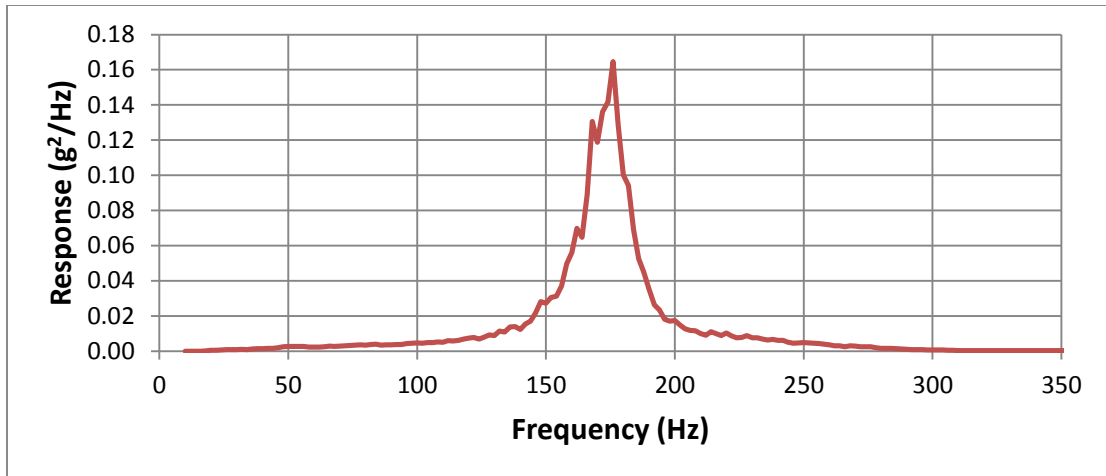
Figure 19: Board Center Z Response Under Out-of-plane Vibration at -12 dB

The third mode of the system is less obvious because most loading conditions that excite the third mode also generally produce a large response of the second mode, thus masking the evidence of Mode III response. Mode III can thus be best observed by looking at the transfer function between the Z response of component 5 and the table under in-plane vibration shown in Figure 20. The eccentricity of the mass excites the third mode without strongly exciting the second mode. The frequency for the third mode was found to be 214 Hz. A strong peak is also seen at 188 Hz. This is not due to board dynamics, but rather a cross-axis coupling resonance in the shaker table which is observed in both the component and table PSD.
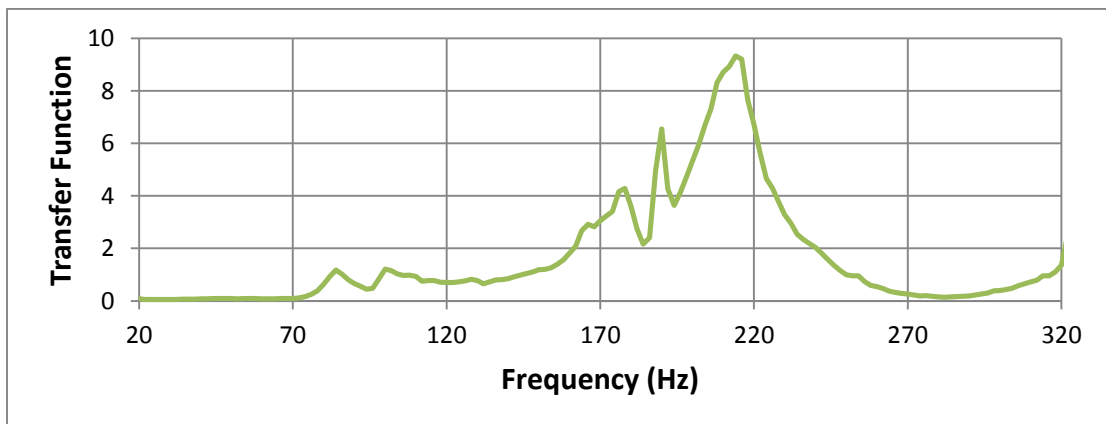
Figure 20: Transfer Function between Component 5 Z Response and Z Motion of Table Under In-plane Vibration at -12 dB

3.2.2 Response Non-linearity

If the system were linear, one would expect the response due to the combination of in-plane vibration and out-of-place vibration to be the sum of the responses observed during the constituent single axis vibration tests. Examination of the experimental results shows this is not the case for either the full durability test level or for the -12 dB vibration level. The response of component 1 in the X direction is shown in Figure 21 and Figure 22. In both cases, the combined vibration produces a non-linear response. At -12 dB, the response under combined loading is 1.5x greater than the summation of the constituent responses while at 0 dB the response is 1.7x greater. While it is not surprising to see non-linearity at the high load levels used for the full scale durability tests, the extent of non-linearity seen under the relatively low -12 dB load level is surprising. Similar results are seen for Component 5 in Figure 23 and Figure 24.
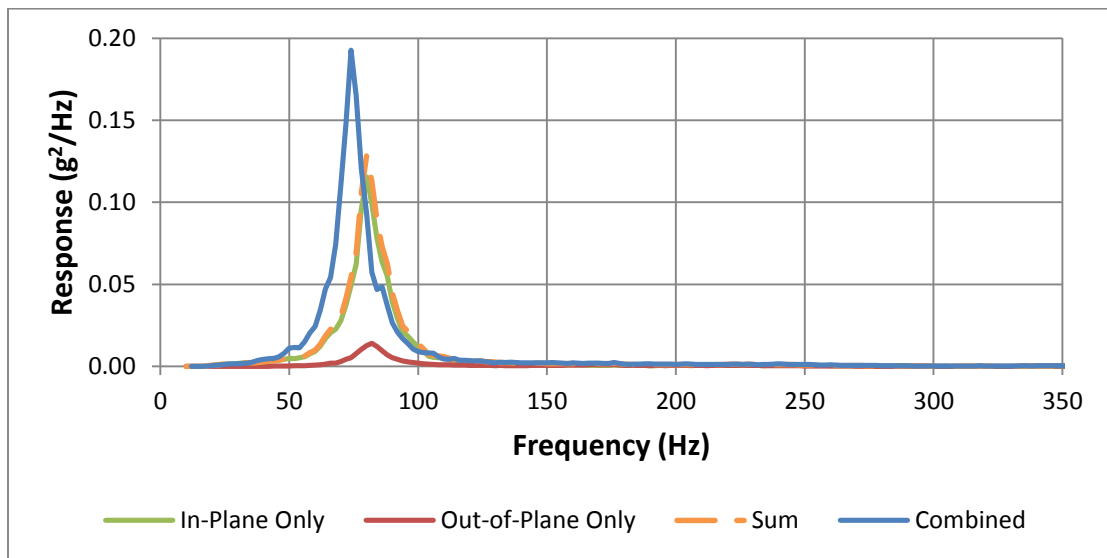
Figure 21: Component 1 X Response Non-Linearity at -12 dB
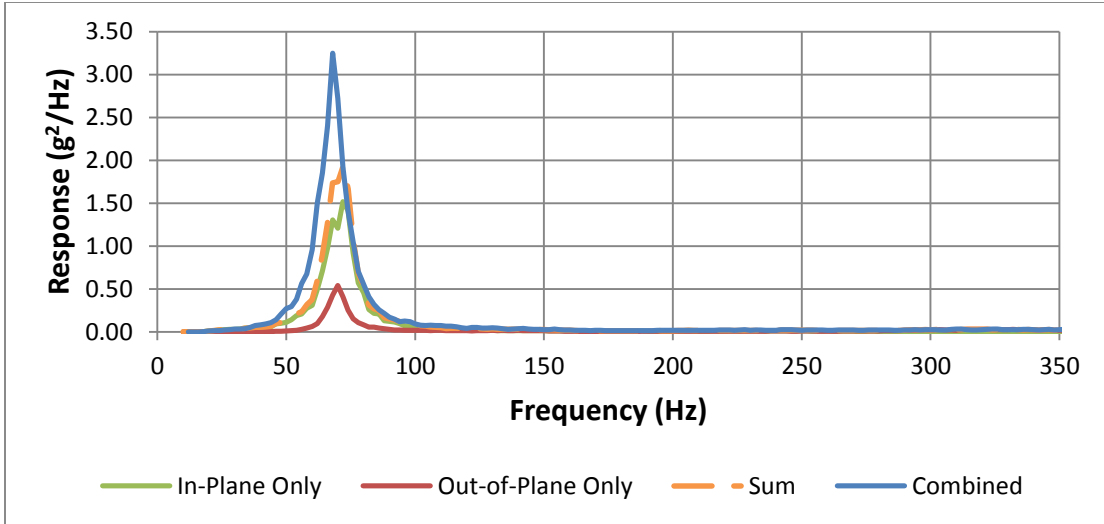
Figure 22: Component 1 X Response Non-Linearity at 0 dB
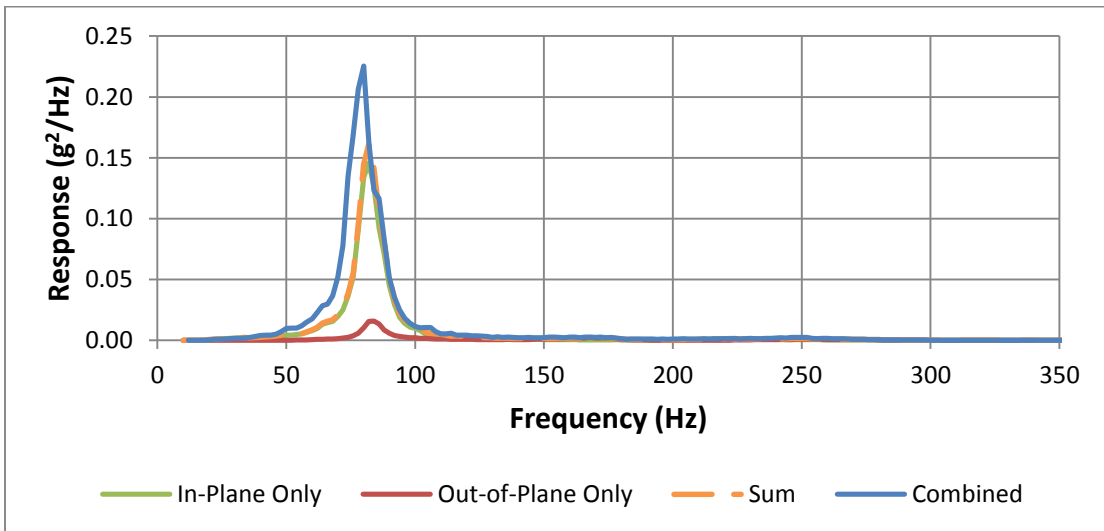
Figure 23: Component 5 X Response Non-Linearity at -12dB
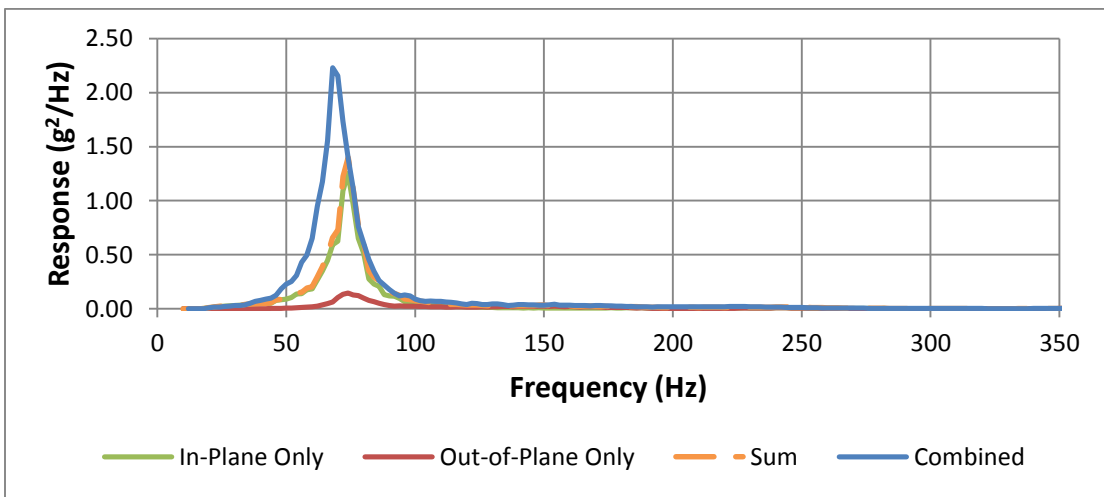
Figure 24: Component 5 X Response Non-Linearity at 0 dB

4. Durability Results

4.1 Background

Durability testing was conducted as described in Section 2. In all cases, the failure site was the copper component lead between the top of the solder fillet and the component body as shown in Figure 25. In 41 of 42 failures recorded, the failure occurred in the component lead corresponding to the outside wrap of the inductor coil, as shown in Figure 26. Thus the asymmetry in the component design discussed in Section 2.2.1 was very significant to the failure mode and hence to the damage accumulation rate.
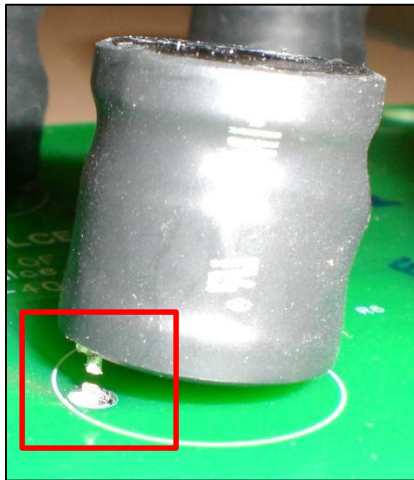
Figure 25: Failure Site on Component on Board
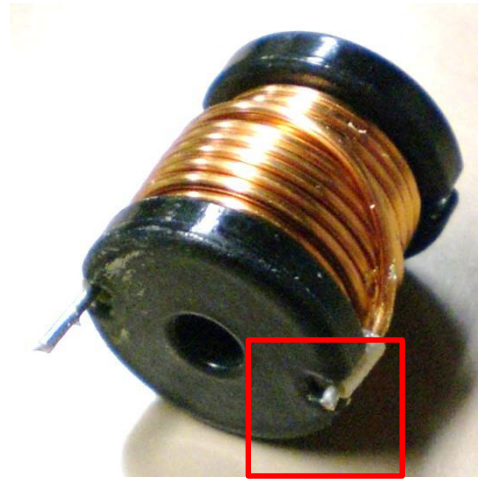
Figure 26: Failure Site on Deconstructed Component

4.2 Data

As discussed earlier in Section 2.5, in the first replicate of tests [17], tests were only conducted until the first component on a board failed. Results are shown in Figure 27 and Table 4.
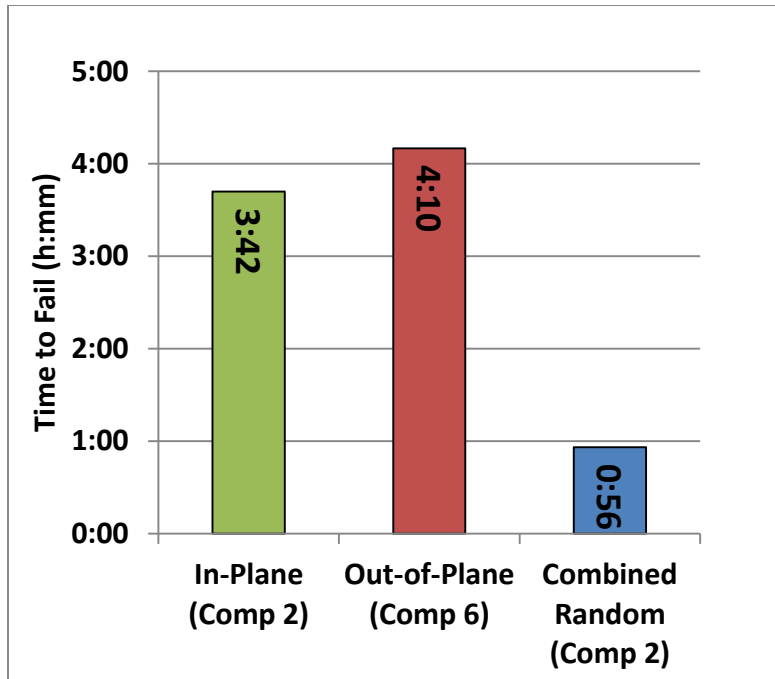
Figure 27: First Replicate [17] Time-to-Failure

Table 4: First Replicate [17] Time-to-Failure

Test Conditions	Time-to-Failure (hh:mm)
In-Plane	3:42
Out-of-Plane	4:10
Combined (Random)	0:56

The second replicate of tests was conducted in this thesis. During this phase of the experiment, testing was conducted until each component on the board failed in accordance with the procedures listed in Section 2.5. Time-to-fail for each component is shown in Figure 28 and Table 5.
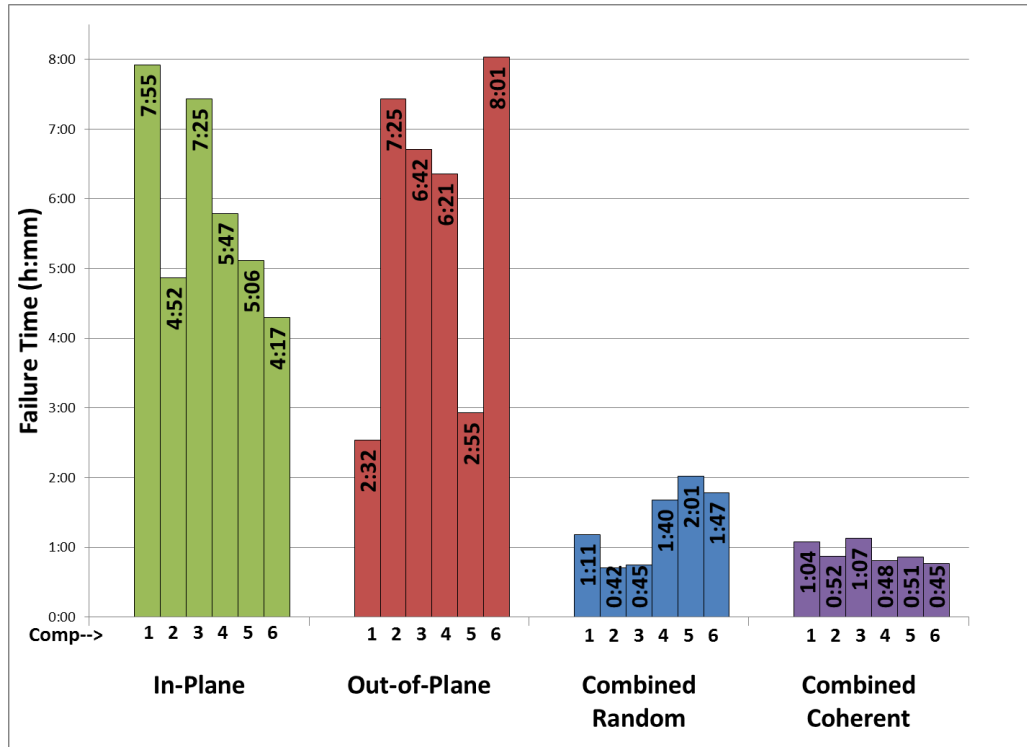
Figure 28: Second Replicate Time-to-Failure

Table 5: Second Replicate Time-to-Failure

Test Conditions	Component Time-to-Failure (hh:mm)						
	1	**2**	**3**	**4**	**5**	**6**	**Average**
In-Plane	7:55	4:52	7:25	5:47	5:06	4:17	5:54
Out-of-Plane	2:32	7:25	6:42	6:21	2:55	8:01	5:39
Combined Random	1:11	0:42	0:45	1:40	2:01	1:41	1:21
Combined Coherent	1:04	0:52	1:07	0:48	0:51	0:45	0:55

4.3 Comparison of Biaxial vs. Sequential Single-axis Test Methods

In order to assess the adequacy of multi-step single-axis-at-a-time test methods, the durability of the test specimen under uniaxial and biaxial vibration conditions will be compared. An average damage accumulation rate (DAR) is defined as the reciprocal of the time-to-failure with units s^{-1}. Average DAR from the time-to-fail data is

presented in Figure 29. Average failure time and standard deviations are calculated for the six components that failed during the second replicate results obtained during this thesis. The first component failure from the first replicate [17] is shown for comparison.
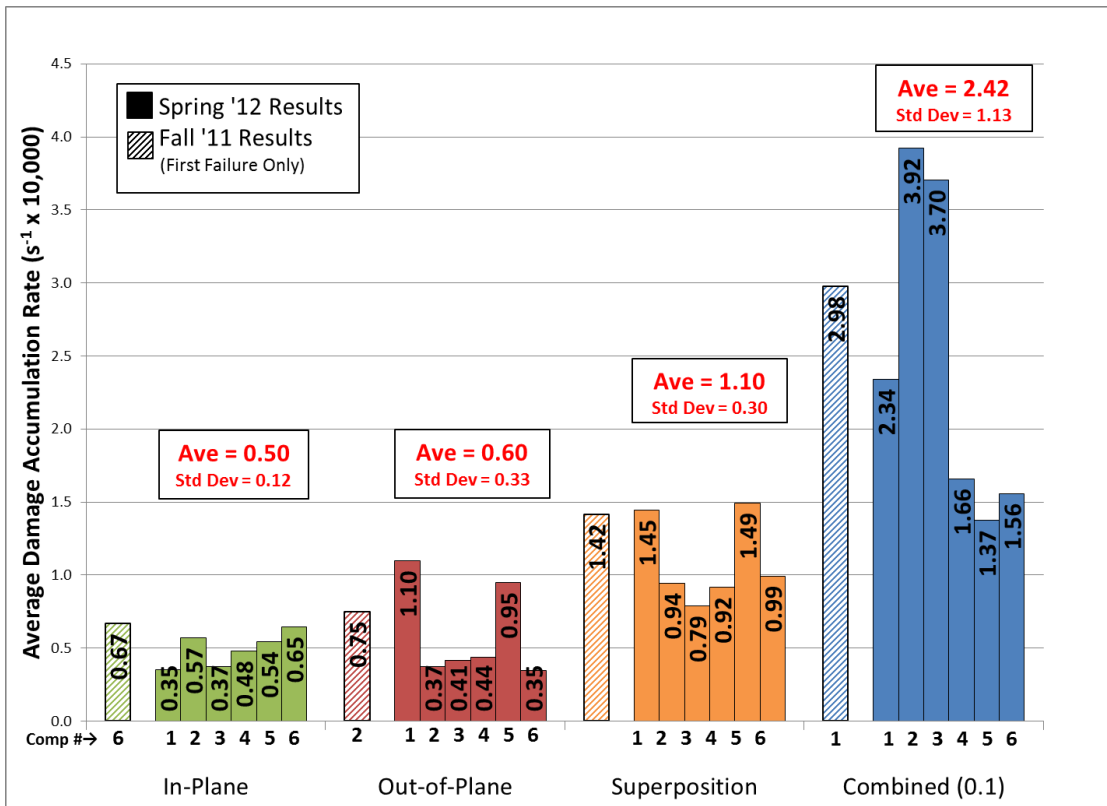
Figure 29: Multi-axis and Single axis Average Damage Accumulation Rates

In addition to the average DAR for each type of vibration test performed (in-plane, out-of-plane and combined), a calculated DAR for the superposition of in-plane and out-of-plane vibration is determined by summing the in-plane and out-of-plane DARs (labeled as "superposition" in Figure 29). This superposition DAR represents the total damage accumulation rate for a complete single-axis-at-a-time test sequence. The superposition DAR can be directly compared to the combined DAR to understand the relationship between multi-step single-axis-at-a-time test methods and true simultaneous multiaxial vibration conditions. These results indicate that single-

axis-at-a-time methods may drastically under represent damage accumulation rates. For this test specimen, a multi-step single-axis-at-time test would over estimate product life by more than a factor of two. This relationship is specific to the test specimen and should not be used as a general correction factor for other structures. The magnitude of error depends on the amount of cross-axis interactions. This specimen represents a fairly severe case of such interactions for two reasons. First, while each direction of loading produces separate modal response, each of these modes creates large stresses at the same location (the lead). Second, the high radius of gyration of the inductor components creates a large geometric non-linearity under cross-axis vibration. This issue is discussed further in Chapter 5. Even though this represents an extreme case, the results can be used to gain some understanding of how misrepresentative multi-step single-axis test methods can be. To develop meaningful correction factors for multi-step single-axis vibration testing, for a broad range of structures, further studies are essential.

4.4 Coherent vs. In-coherent Vibration

The results of combined coherent vs. combined incoherent random vibration tests are useful for comparing true multiaxial vibration test methods to test methods which fixture a device at an angle to replicate the resultant magnitude of a three component PSD using single axis test equipment. Essentially this method treats the PSD magnitude at each frequency as a vector and sums the three components to produce a resultant magnitude and direction at each frequency. If the PSD shapes in each of the three orthogonal axes are scalar multiples of one another, then the vector at each frequency has the same direction. When this condition is true it is meaningful to

33

define a resultant PSD with a new magnitude and direction. The new magnitude is the new PSD specification for the single axis test equipment and the new direction is the fixturing angle. Since the in-plane (X) and out-of-plane (Z) PSD profiles for this durability test were specified with the same profile and since the second in-plane (Y) PSD profile was zero for all frequencies, using the resultant PSD test method would be possible for this test. The resultant PSD to use is graphically shown in Figure 30.
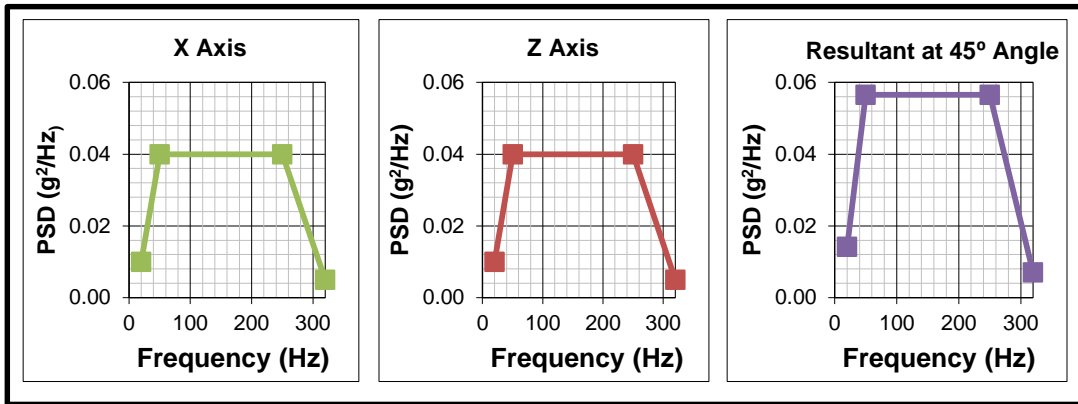
Figure 30: Graphical Depiction of PSD Addition

The difference between the resultant PSD and true multiaxial vibration environments is the phase coherency between the axes. In some environments coherence may be present due to motions in two measured axes originating from the same source; however, in a multiaxial environment, there is, in general, no requirement for coherence between the axes. As the number and complexity of vibration sources increase one would expect the coherency between axes to tend toward complete incoherence. In contrast, when the resultant PSD method is used, absolute coherence between each component is imposed mechanically since only one shaker is used to generate vibration. Using the TEAM six-DOF shaker table and Data Physics controller, this same condition can be created by using the same in-plane and out-of-plane profiles used previously, but specifying cross-axis coherence between

34

the shakers. For the purpose of this test a minimum of 90% cross-axis coherence between the in-plane and out-of-plane axes was specified for the coherent test while a minimum 10% cross-axis coherence was specified for the incoherent test. The test was conducted in the same manner as previous durability tests. Average damage accumulation rates for each component are shown in Figure 31. To see the results in time-to-fail format, refer back to Figure 28.
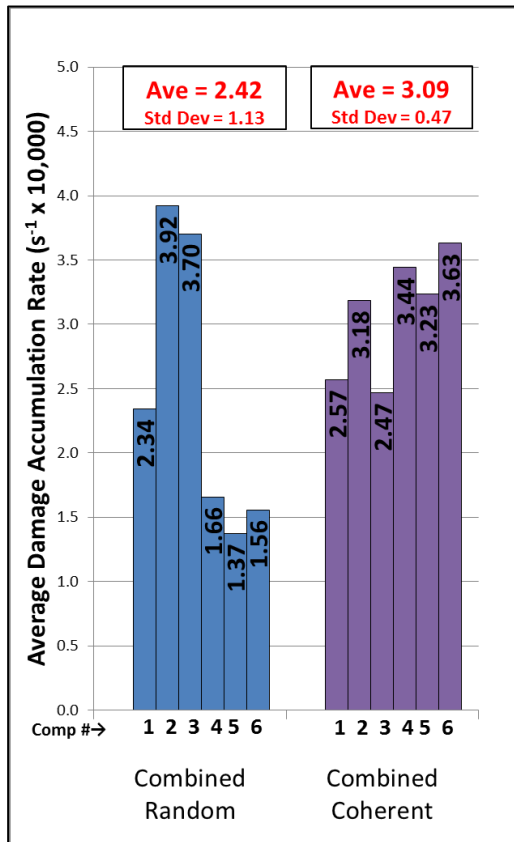
Figure 31: Coherent and Incoherent Average Damage Accumulation Rates

The results indicate that, on average, coherent vibration is more damaging then in-coherent vibration. One also observes a much lower standard deviation in the coherent results compared to the incoherent results. With the limited sample size of this test, it is difficult to know if the short time-to-failure (high average DARs) of components two and three during the in-coherent test were a true manifestation of the

damage under the in-coherent conditions or if they were the result of pre-test damage in the leads. Statistically speaking, the means are different with an 89.9% level of confidence.

From the durability results presented, it seems the resultant PSD test method produces more accurate durability estimates than the multi-step single-axis method. Further studies are recommended to develop correction factors for the resultant PSD method for different types of test structures.

5. Non-linear Geometric Effects on a Beam Subject to Biaxial Vibration

5.1 Background

Frequency domain methods are often employed to efficiently perform a fatigue analysis of structures subjected to random vibration. The primary advantage of frequency domain methods is the reduction in computational expense and complicated transient effects present in time domain analysis. Unfortunately, frequency domain methods assume system linearity. As discussed in Section 3.2.2, significant non-linearity was observed in the component response, necessitating the use of time-domain methods. While several factors undoubtedly contribute to the non-linearity observed under biaxial vibration, the effect of geometric deformation was chosen for an in-depth examination in this thesis.

5.2 Model Description

The test vehicle used in Section 4 is too complex for theoretical exploration of nonlinear effects and cross-axis synergy. Hence, a simple model was developed to explore the basic principles governing cross-axis synergy during biaxial vibration, due to nonlinear response. The structure modeled was a 45 mm long cantilevered rod of 1 mm diameter with a point mass at the free end. The rod was modeled as Aluminum 6061-T6 with a density of 2.7 g/cm^3 and elastic modulus of 68.9 GPa. During each analysis, stress remained below the typical yield point of 275 MPa therefore plasticity was not included in the model. Rayleigh mass-proportional damping was used for the rod and point mass, with an alpha coefficient of 100. The geometry and properties specified above resulted in a rod mass of 0.0954 g. The end

mass was specified as 0.29 g which resulted in a 95 Hz first mode natural frequency. The second mode frequency was 1558 Hz.
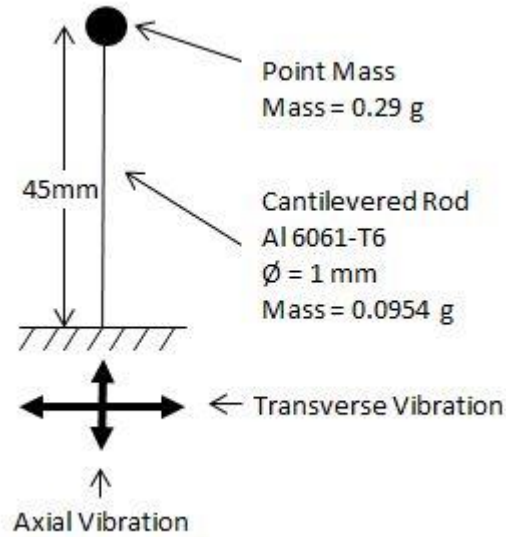
Figure 32: Beam Model Diagram

Vibratory excitation was applied to this model in the form of accelerations applied to the base of the rod in the transverse and axial directions. Transverse accelerations were always a 90 Hz sinusoid with a peak acceleration of 30.58 g (300,000 mm/s^2). This value was selected to create large deflections of the beam without exceeding the yield stress of the material. Several different types of vibrations were applied in the axial direction. The first broad class of vibration was harmonic excitations using a sine wave pattern with peak acceleration of 61.16 g (600,000 mm/s^2) and frequencies from 90 Hz to 270 Hz. The second broad class was narrow-band random vibration with a bandwidth of 20 Hz and center frequencies of 90 Hz and 180 Hz. The amplitude of the random signal was set such that the root mean square of the time domain signal was the same as that of the harmonic signal. This random vibration signal was synthesized using the methods outlined in Appendix D.

38

The model was constructed using the ABAQUS/CAE finite element analysis software

package. The beam was modeled using 30 B21 linear shear deformable beam

elements in a two dimensional plane. The dynamic-implicit

(ABAQUS/STANDARD) procedure was used to execute the analysis.

5.3 Beam Motion under Single-axis Harmonic Excitation

For a complete discussion on the theory concerning the response of a beam subjected

to a single transverse base motion, Meirovitch's textbook, *Fundamentals of*

Vibrations [18], provides an excellent general reference. Additionally, a complete

derivation of an analytic solution for the steady state response of a cantilevered rod

with an applied base excitation can be found in [19] and is presented in Equation 1.

$$u(x,t) = 2A \sum_{j=1,2,3\ldots}^{\infty} \frac{\frac{\cos \lambda_j l + \cosh \lambda_j l}{\sin \lambda_j l + \sinh \lambda_j l}}{\lambda_j l} \frac{\left(\frac{\omega}{\omega_j}\right)^2 \Phi(x)}{\left\{\left(1 - \left(\frac{\omega}{\omega_j}\right)^2\right)^2 + \left(2\zeta_j \frac{\omega}{\omega_j}\right)^2\right\}^{1/2}} \sin \omega t$$

Equation 1: Cantilevered Rod Analytic Solution

Where:
  A is the amplitude of base oscillation
  u is the displacement of beam
  t is the time
  ω is the frequency of forcing function or base oscillation
  ω_j is the modal natural frequency (j=1,2,3,4…)
  ζ_j is the modal damping value (j=1,2,3,4…)
  x is the longitudinal position or node location
  $\Phi(x)$ represents the shape of the jth mode of the beam and is given by Equation 2.
  $\lambda_j l$ is found by solving the transcendental equation of the cantilevered beam. The
    first four values are given in Table 6 for reference.

$$\Phi(x) = \cos \lambda_j x - \cosh \lambda_j x - A(\sin \lambda_j x - \sinh \lambda_j x)$$

Equation 2: Shape of the jth Mode of the Rod

Table 6: Solution of the Transcendental Equation for a Cantilevered Rod

j	$\lambda_j l$
1	1.875
2	4.694
3	7.855
4	10.996

It is also useful to note that the modal damping values of Equation 4 can be related to the Rayleigh damping values (α and β) through Equation 3.

$$\alpha + \beta \omega_j^2 = 2 \zeta_j \omega_j$$

Equation 3: Modal Damping in Terms of Rayleigh Damping Coefficients

As shown by Equation 1, the steady state motion of a cantilevered rod will be periodic with a frequency equal to the frequency of the base motion. For a given rod geometry, the response amplitude will be affected by the amplitude of base motion, damping in the beam and frequency relationship between the base motion and natural frequency of the rod.

In addition to affecting response amplitude, the damping used in the beam model causes three other important effects. First, it causes the solution to be bounded for all frequencies. Second, it damps the transient solution and forces the finite element solution to converge to the steady state solution which is the subject of this analysis. It was found that the damping present in the model (alpha = 100) was sufficient to bring the solution to steady state within a reasonable time period. As such, the techniques outlined in Appendix F to remove the transient period were not necessary.

Finally, damping governs the phase relationship between the base motion and the beam motion.
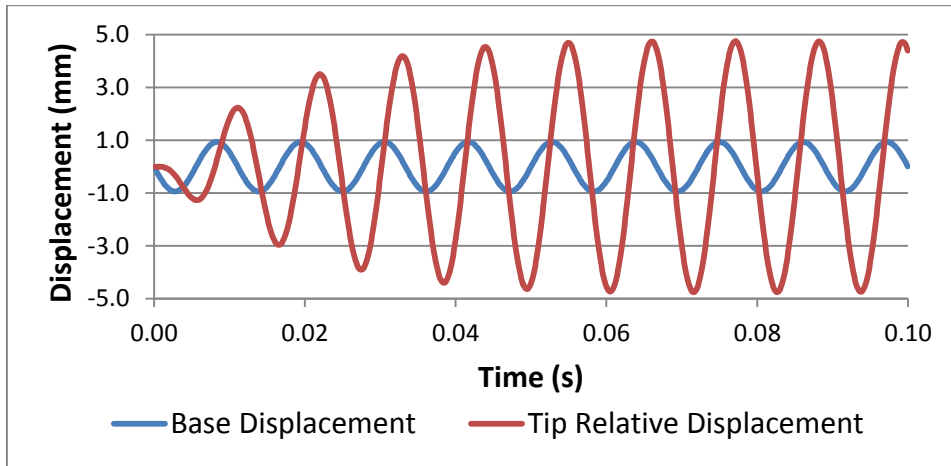
Figure 33: Tip and Base Displacement under Transverse Vibration Only

Figure 33 shows the FEA-derived displacement of the tip of the beam relative to the base displacement during transverse vibration only. In this figure, one can observe the convergence to the steady state solution no later than 0.1 seconds after the start of the simulation and the tip motion lagging the base motion by 0.00208 seconds (67.24° phase). For reference with the following discussions, the maximum steady state stress in the element closest to the base has an amplitude of 239.5 MPa.

5.4 Effect of Vibration in Axial Direction

When only harmonic axial vibration is present, stress in the rod is uniform across the cross section and alternates between tensile and compressive stress as the acceleration of the rod alternates between positive and negative. Through an FEA simulation the amplitude of this stress at steady state was found to be 0.295 MPa. If the effects of the geometric deformation are ignored, then an additional 0.295 MPa stress in the lead would be the maximum expected stress increase due to the axial vibration. However, when geometric deformation is considered, a significantly larger stress is

41

calculated, because the inertial forces produce a bending moment on the rod. If the transverse displacement of the rod is large enough, the additional bending moment produced by the axial vibration will contribute significantly to the stress at the base of the beam.

5.5 Effect of Phase under Biaxial Harmonic Excitation

A series of finite element simulations were performed using the 90 Hz transverse vibration and 180 Hz axial vibration as described in Section 5.2. The phase relationship between the transverse and axial vibrations was varied and the steady state stress amplitude measured. The results of this analysis are shown in Figure 34.
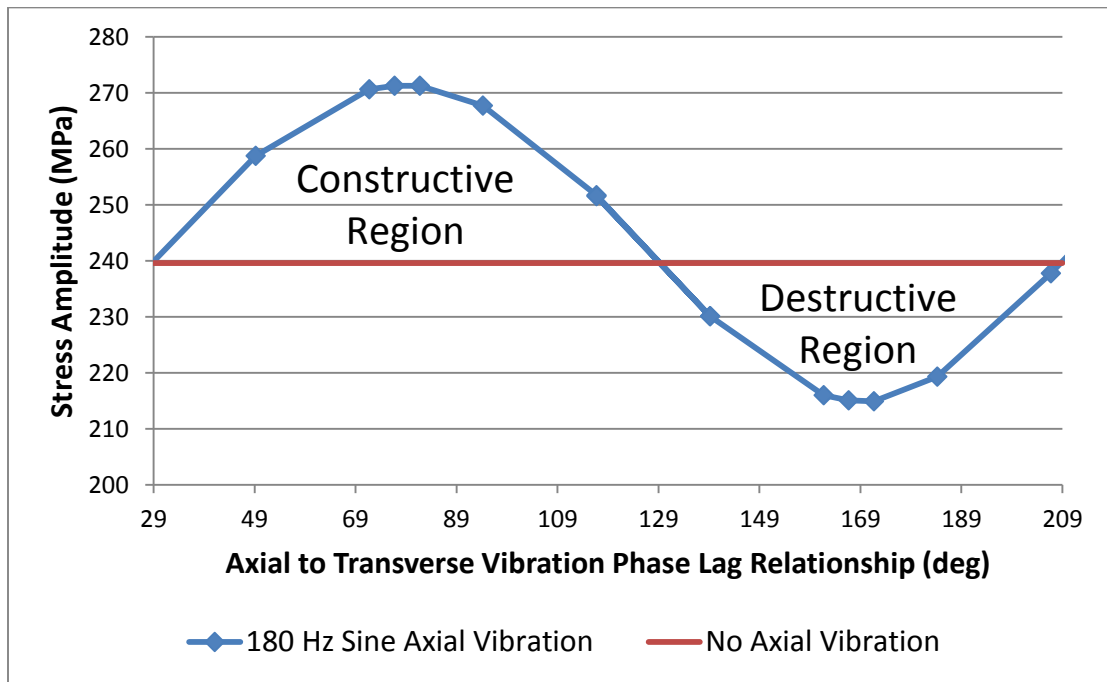
Figure 34: Biaxial Phase Relationship Effect on Stress Amplitude

For the range of phases between 29° and 129° the presence of 180 Hz axial vibration increased the stress amplitude in the rod as compared to the no-axial-vibration condition. For the range of phases between 129° and 209° the 180 Hz axial vibration decreased stress amplitude in the rod. It should also be observed that the maximum

constructive (synergistic increase in stress) effect is larger than the maximum

destructive (synergistic decrease in stress) effect. To understand this effect one must

understand how the axial acceleration acts on the deformed rod. Steady state stress

amplitude is increased when axial acceleration is applied in a direction which

increases the magnitude of the beam velocity. Conversely, stress amplitude is

decreased when axial acceleration decreases velocity. Simply stated, this requires a

positive acceleration when the rod is moving away from center and a negative

acceleration when the rod is moving toward center. Illustrations for the base

accelerations producing increases and decreases in stress are shown in Figure 35 and

Figure 36.
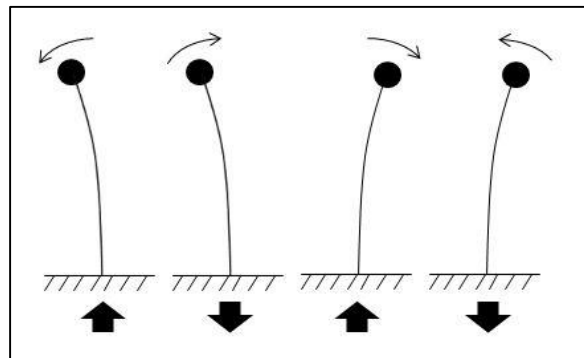
Figure 35: Base Motions to Increase Stress Amplitude
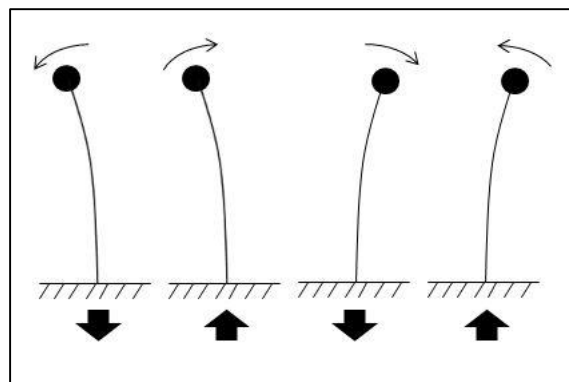
Figure 36: Base Motions to Decrease Stress Amplitude

43

Thus, the optimum base acceleration waveform for increasing stress is a square wave with a frequency twice the transverse frequency. The phase must be aligned such that the acceleration acts as depicted in Figure 35. The optimum constructive relationship between the transverse displacement of the rod tip and the axial acceleration of the base is show in Figure 37. One cycle of rod motion is depicted. Finite element results show that the relationship depicted in Figure 37 does in fact produce maximum stress amplitude.
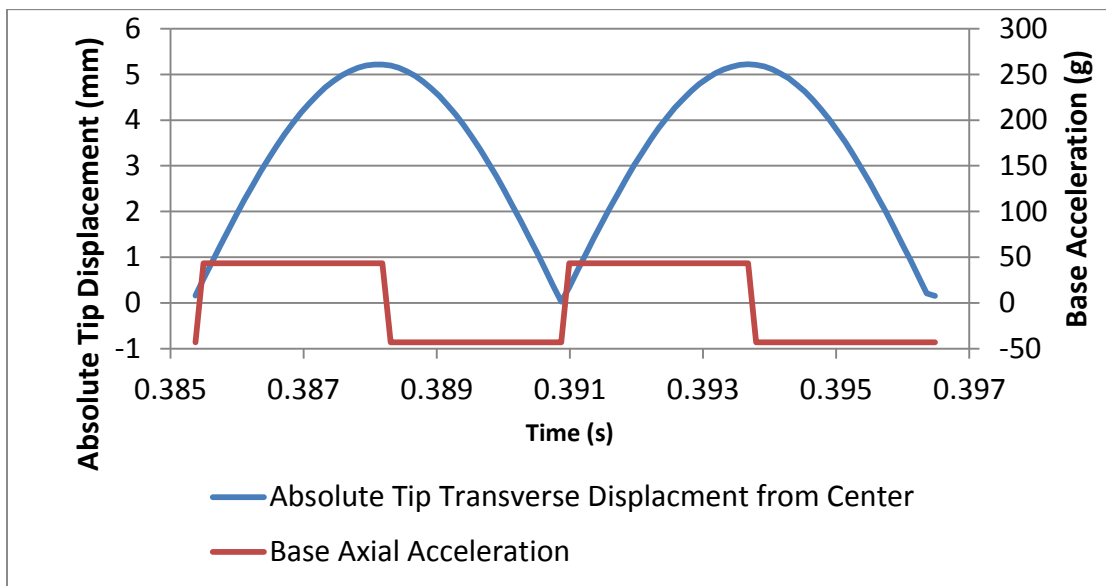
Figure 37: Optimum Constructive Relationship for Square Wave Acceleration
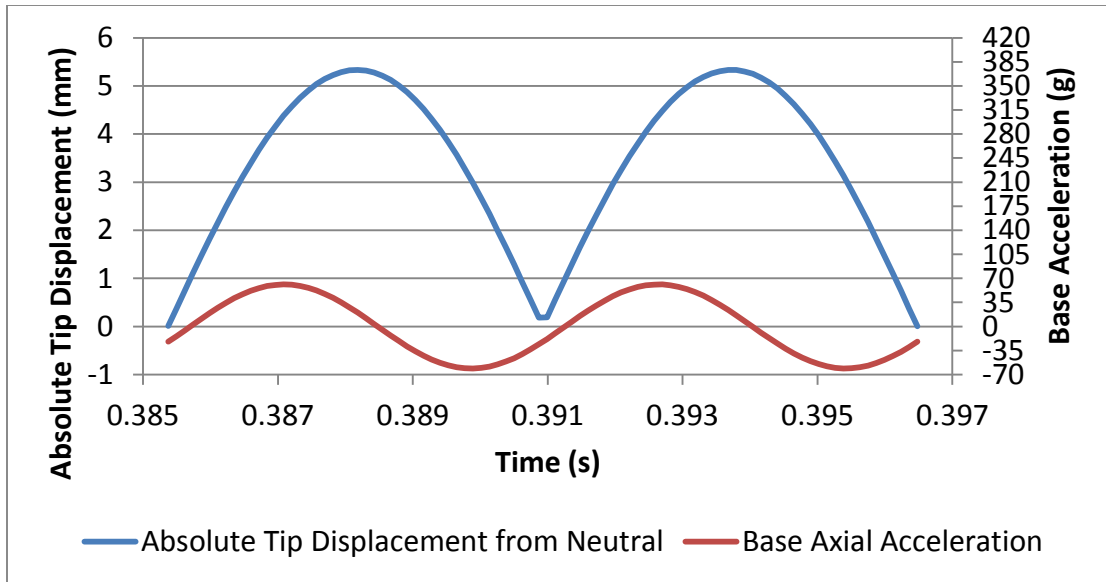
Figure 38: Optimum Constructive Relationship for Sine Wave Acceleration

When the axial acceleration at the base is applied with a sine waveform rather than a square wave, the general relationship is the same however FEA results indicate the acceleration is required to lead the displacement by approximately 11 degrees phase to achieve the maximum stress. This relationship is shown in Figure 38. This is due to the two competing mechanisms (positive acceleration during increasing deflection / negative acceleration during decreasing deflection) having unequal effects on stress. Because of this difference between the mechanisms, the relationship skews such that the mechanism with a stronger effect (positive acceleration during increasing deflection) acts when deflections are larger and produces larger stress amplitude.

The second effect observed in Figure 34 is the larger impact of the constructive effects compared to the destructive effects. At the maximum constructive phase, stress amplitude is increased 31.67 MPa while at the maximum destructive phase stress is only decreased by 24.68 MPa. The effect is explained by fact that when the relationship is constructive, transverse deformation is increased giving greater effect

45

to the axial vibration while destructive relationships reduce the transverse

deformation reducing the effect of the axial vibrations.

5.6 Effect of Frequency Ratio under Biaxial Harmonic Excitation

The preceding analysis of the effect of phase relationship considered an axial

vibration at a frequency exactly twice the transverse frequency. When the frequency

in one axis is a whole number multiple of the frequency in the orthogonal axis a

special case is established such that the phase relationship is constant with time. For

cases where the axial vibration is at a frequency other than a whole number multiple

of the transverse frequency, the phase relationship changes over time at a rate equal to

the difference between the two frequencies. For example, if a 90 Hz transverse

vibration and 135 Hz axial vibration were used, the phase relationship would change

from maximum constructive to maximum destructive at 45 Hz. For axial frequencies

above 135 Hz, the amplitude modulation is observed as the difference between the

axial frequency and the first harmonic of the transverse frequency. This amplitude

modulation can be seen by comparing the two traces in Figure 39.
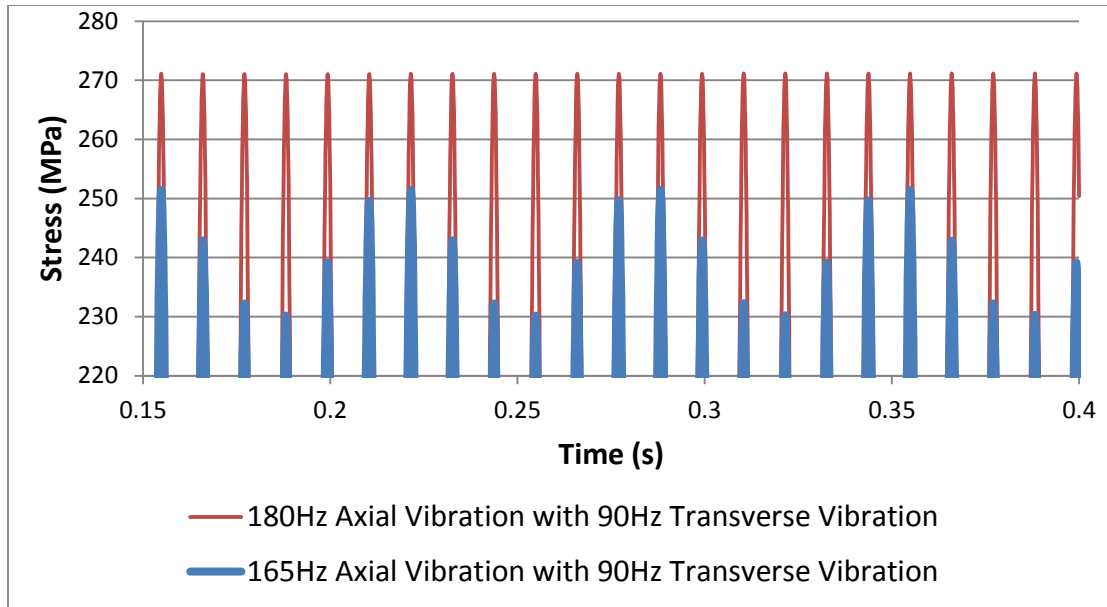
Figure 39: Depiction of Amplitude Modulation

In one case of Figure 39, an axial frequency of 180 Hz is used resulting in a constant phase relationship and no modulation of the stress amplitude. In the second case of Figure 39, an axial frequency of 165 Hz is used resulting in a stress amplitude plot with a 15 Hz modulation. The peak of this modulation occurs when axial and transverse vibrations are at their most constructive phase relationship. The valley occurs when the axial and transverse vibrations are at their most destructive. Thus, when an axial vibration is applied at other than a whole number multiple of the transverse frequency, the stress amplitude can be extracted for the most constructive and destructive phases. By performing FEA simulations of the rod with a range of axial frequencies, and employing the above technique to determine the maximum constructive and maximum destructive stress amplitude, Figure 40 was generated.
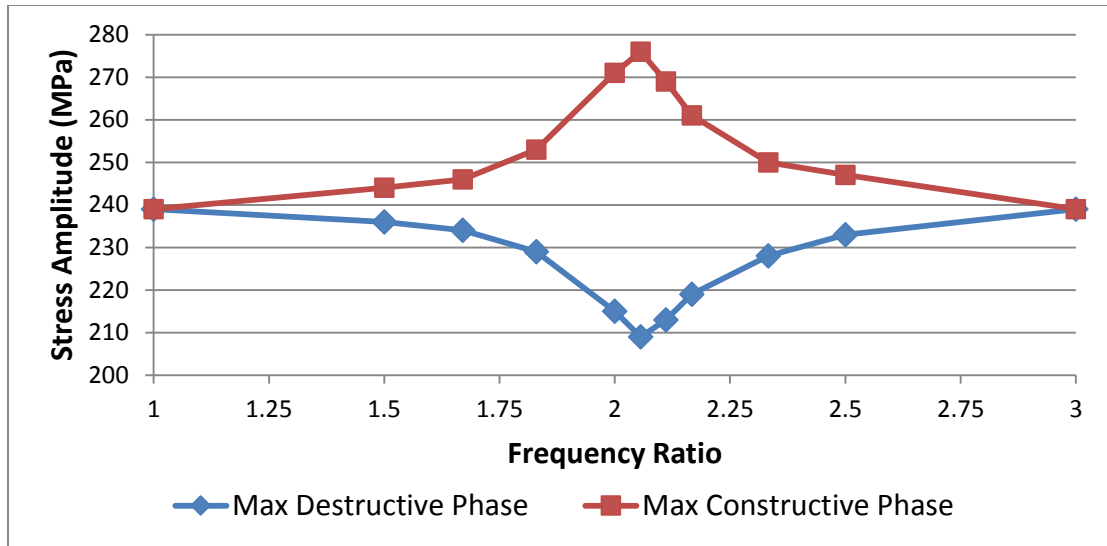
Figure 40: Effect of Frequency Ratio on Stress Amplitude

The most striking deduction from Figure 40 is that as the axial vibration frequency changes from an even multiple of the transverse frequency to an odd-multiple, the effect of the axial vibration is reduced from a maximum to approximately zero. To understand this phenomenon, it is instructive to refer back to Section 5.5. If a square wave acceleration is applied in the axial direction at the same frequency as the transverse motion, one observes that no matter what phase relationship is established between the two axes, equal constructive and destructive effects will exist during each transverse cycle. Thus, the effects are frequency filtered such that axial acceleration frequencies near the transverse frequency and odd multiples of the beam are blocked while those near even multiples are passed with smoothly varying levels of transmission in between.

A second observation from Figure 40 which at first appears to conflict with the above conclusion is that the maximum was not at a frequency ratio of 2. In fact, it was found to be near 185 Hz which corresponded to frequency ratio of 2.056.

Additionally the data is observed to be generally skewed toward higher frequency ratios. This is explained by the fact that the rod's natural frequency was 95 Hz with a first harmonic at 190 Hz. The beam displays a larger response to driving frequencies near its natural frequency and harmonics. Thus the combination of maximum theoretical response at 190 Hz with a filtering profile that is maximum at 180 Hz results in an observed peak at approximately 185 Hz. The presence of this mechanism was confirmed by repeating the frequency ratio FEA simulations using a beam with a natural frequency of 85 Hz. In this case, the maximum effect due to axial acceleration was observed at approximately 175 Hz.

5.7 Effects under Narrow-band Random Vibration

Significant differences exist between harmonic vibration and random vibration. These differences raise questions about how a beam subjected to biaxial vibration will be affected when one or more of the vibrations are random rather than harmonic. Transverse random vibration will establish a transverse beam response which is highly periodic at the natural frequency of the beam. In order to keep the transverse response frequency consistent with the previous work on harmonic excitation and allow easier comparison between the harmonic and random results, this study will continue to use a 90 Hz sine input in the transverse direction and focus on random vibration in the axial direction only.

Unlike harmonic vibration, when random vibration is applied in the axial direction, no steady or predictable relationship exists between the transverse deflection of the beam and the axial base motion. Furthermore, by definition, random signals cannot

exist at a single frequency. Instead, a random signal's energy is distributed over a frequency range known as its bandwidth. Because of this characteristic, the notion of a frequency ratio between the transverse and axial directions is no longer exact. Customarily, stationary random vibrations are characterized as an acceleration magnitude within a particular bandwidth. These are generally referred to as power spectral density (PSD) or acceleration spectral density (ASD) profiles. If the random vibration has a constant spectral density across a continuous bandwidth, then one can reference the ratio between the transverse frequency and the center of the random vibration bandwidth. Such a signal will be used for the examination presented in this section.

In order to examine the effect of random vibration in the axial direction, several finite element simulations were conducted. These models used a 90 Hz transverse vibration combined with a random vibration with 20 Hz of bandwidth. A 20 Hz wide signal was chosen to allow for examination of several different non-overlapping frequency ratios between the natural frequency of the beam and twice the natural frequency of the beam. The amplitude of the axial vibration was set such that the resulting signal had the same time domain root mean square as the 180Hz sine vibration used in the previous sections. The signal was synthetized using Method II described in Appendix D.

The nature of random vibration results in a stress amplitude response which becomes statistically stationary at steady state, but does not achieve a state where stress

50

amplitude is constant with each cycle. This necessitates statistical analysis and

reporting of the FEA results for random vibration. Figure 41 depicts the stress at the

base of the beam during 90 Hz harmonic transverse and 170-190 Hz random axial

vibration. Similarly, Figure 42 depicts the stress at the base of the beam during 90 Hz

harmonic transverse and 80-100 Hz random axial vibration.
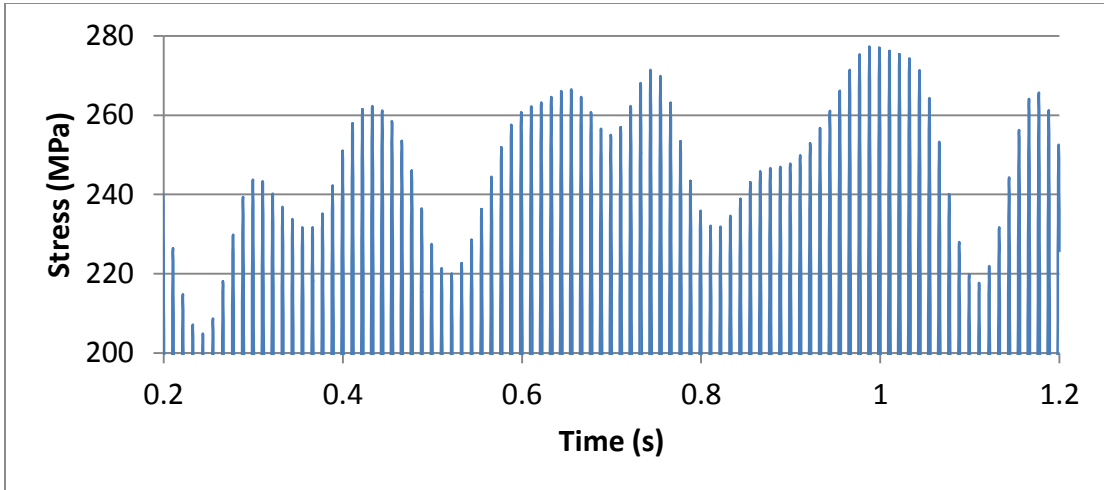
Figure 41: Stress Amplitude with 170-190 Hz Random Axial Vibration
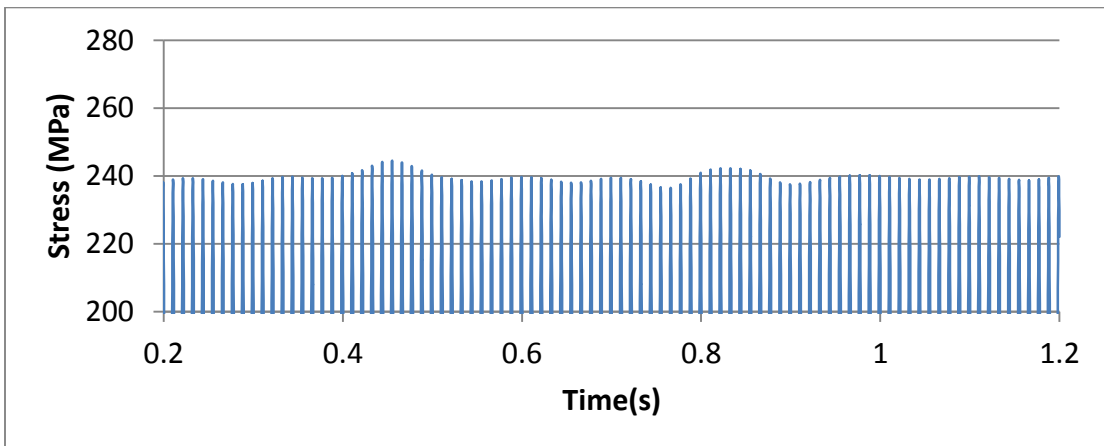
Figure 42: Stress Amplitude with 80-100 Hz Random Axial Vibration

As one can see, the stress amplitude varies unpredictably over the time period of the

simulation when certain frequency bands are used. In order to analyze this data

several statistical measurements were made. The mean, standard deviation, skewness

and kurtosis were calculated for the entire time domain signal beyond 0.2 seconds.

The first 0.2 seconds were omitted to remove the initial transient effects.

Additionally, each positive and negative peak was measured. Most of this stress is

due to the transverse vibration, but the modulation is due to the axial vibration. The

mean and standard deviation of the peak values were also calculated. The results for

several different frequency ranges of axial vibration are shown in Table 7 and Table

8.

Table 7: Peak Stress Statistics

			Peak Stress (MPa)			
Freq. Ratio	Center Freq. (Hz)	Range (Hz)	Mean Pos. Peak	Mean Neg. Peak	Std Dev Pos. Peak	Std Dev Neg. Peak
1.00	90	80-100	239.52	-240.44	1.51	1.46
1.56	140	130-150	240.15	-240.30	3.48	3.48
1.78	160	150-170	240.75	-240.93	7.03	7.35
2.00	180	170-190	247.76	-247.98	17.93	18.08
2.22	200	190-210	240.62	-240.65	13.26	13.00

Table 8: Time History Stress Statistics

			Time History Stress (MPa)			
Freq. Ratio	Center Freq. (Hz)	Range (Hz)	Mean	Std Dev	Skewness	Kurtosis
1.00	90	80-100	-0.95	169.87	4.50E-03	1.50
1.56	140	130-150	0.06	170.08	-1.10E-03	1.50
1.78	160	150-170	0.03	170.64	-1.30E-03	1.50
2.00	180	170-190	0.09	175.99	-1.40E-03	1.53
2.22	200	190-210	0.07	170.31	-7.98E-04	1.52

As one can see in Table 7, the effect of random axial vibration is similar to the effect

of harmonic axial vibration. When the band of random vibration is centered near the

frequency of transverse motion, the axial vibration produces no significant effect. As

the band center is swept to twice the frequency of transverse motion, the mean stress

amplitude increases as compared to the stress amplitude without axial vibration. In

the presence of random axial vibration, both constructive and destructive phase relationships exist in the time history, however, the imbalance between constructive and destructive effects as shown in the discussion on harmonic vibration results in a net increase in the mean stress over time. Perhaps more significant for the consideration of fatigue and failure is the large increase in standard deviation of the stress amplitude due to axial vibration at twice the transverse frequency. This large increase in standard deviation is indicative of much higher stress amplitudes occurring in a time history than would be calculated if the non-linear geometric effects of axial vibration were not considered.

5.8 Conclusions

The examination of a beam subjected to transverse and axial vibrations has revealed several useful insights. Foremost is the finding that substantial stress amplitude increases are possible when significant transverse deformations occur in the presence of either harmonic or random axial vibrations. The significance of the impact on stress is greatly dependent on the frequency relationship between the transverse motion and the axial vibration. The maximum effect occurs when the axial vibration occurs at or the near an even multiple of transverse frequency. Little or no effect is observed when the axial frequency is near the transverse frequency or an odd multiple. This finding has implications for analysts and designers. Analysts may be able to safely neglect the non-linear effects of geometric deformation if the frequency ratio between vibrations is known to avoid ranges where stress increases are possible. Similarly, designers can avoid situations where biaxial vibrations increase stress in certain locations by controlling the natural frequencies of critical components.
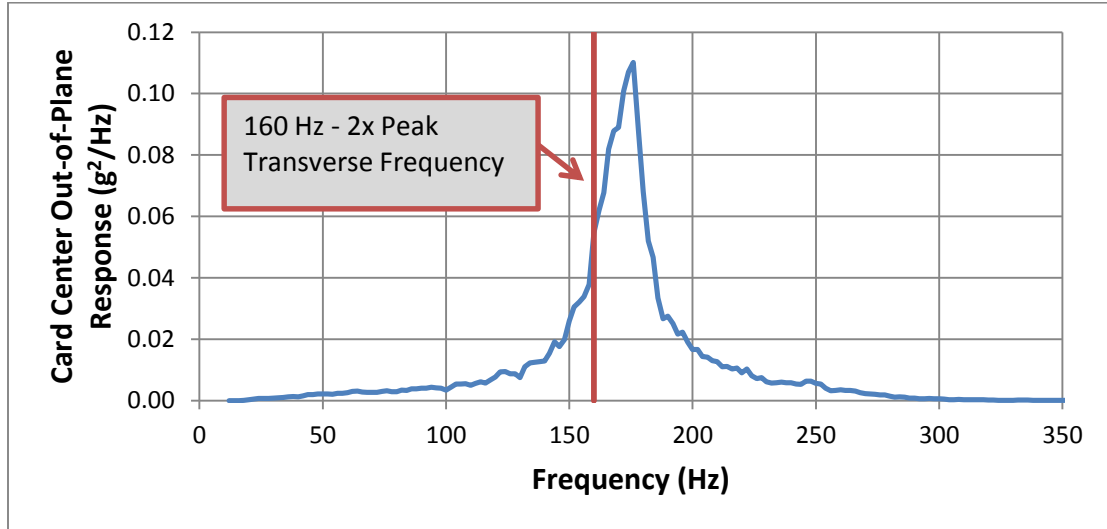
Figure 43: Card Center Out-of-Plane Response

Through happenstance, the specimen tested in Section 4, was designed in a way that may have made the components mounted on the card prone to the type of stress amplitude increase described above. The components responded to the broadband excitation with a transverse motion at their first mode frequency of approximately 80 Hz. The axial motion applied to the components was the out-of-plane motion of the card. The card's out-of-plane response was centered on its first mode natural frequency of approximately 176 Hz with the energy in a narrow band from approximately 148 – 198 Hz. Thus, most of the out-of-plane vibration applied to the component was near twice the transverse frequency of motion setting up the conditions for the out-of-plane vibrations to increase the deformation and stress in the component leads. It may be possible in this type of situation to improve performance by adjusting the stiffness of the board to achieve a first mode board frequency closer to 3 times the component frequency or 240 Hz.

6. Summary, Conclusions and Contributions

This section provides a summary of the work completed under this thesis, an overview of the major findings and discussion of the ways this work has expanded the scientific community's knowledge of multiaxial vibration and its effects.

6.1 Summary and Conclusions

The intent of this study was to examine how the simultaneous application of vibratory loading in multiple directions affects structural response and durability of electronic circuit card assemblies, as compared to the linear superposition of multiple uniaxial loadings. Experiments were performed on a TEAM TENSOR TE6-900 MDOF shaker table using an instrumented electronics assembly. The first mode natural frequency acceleration response of inductors on the circuit card was examined under several conditions. Two different uniaxial conditions were measured separately followed by the biaxial vibration condition composed of the two previously tested uniaxial conditions. Under the vibration profile used (based on guidelines in NAVMAT P-9492 [6]), the component on the test specimen experienced 1.7x more transverse acceleration under biaxial conditions than was calculated by summing the constituent uniaxial transverse accelerations. Even at vibration levels 12dB below the level specified in NAVMAT P-9492 [6], biaxial response was still 1.5x larger than that calculated by summing the constituent uniaxial accelerations. These two results show that the response (and consequently the inertial forces) experienced under biaxial vibration differ significantly from the response which would be calculated by the superposition of the component vibrations applied in a uniaxial manner.

A difference between simultaneous multiaxial vibration and the linear superposition of uniaxial vibrations is important because much of the vibration testing used to assess product durability is performed as a series of uniaxial steps rather than a single multiaxial test. An empirical study was performed to further explore the effect of the increased loads experienced under simultaneous biaxial vibration. Several test specimens were tested to failure to determine the average damage accumulation rate (DAR) under simultaneous biaxial vibration and under each of the uniaxial components of the biaxial vibration applied independently. The average DAR was found to be $0.5e^{-4}$ s^{-1} and $0.6e^{-4}$ s^{-1} respectively for the two components of vibration applied independently. The simultaneous application of the two components produced and average DAR of $2.425e^{-4}$ s^{-1}. Thus damage was found to accumulate 2.2 times faster under biaxial vibration than would be indicated by the summation of the constituent parts. These findings are in line with previous reported durability results such as [10] and [12]. Consequently, durability results obtained through the multi-step uniaxial method should not be trusted if vibrations in multiple axes apply stress to the same region.

In addition, DARs were measured for two cases of biaxial vibration. In the first case, the motion in the two axes is completely random (uncorrelated) while in the second case, the motion in both axes is coherent (correlated). Results showed DARs of $2.425e^{-4}$ s^{-1} for the random case and $3.21e^{-4}$ s^{-1} for the coherent case. Thus, in this test, damage was found to accumulate 33% faster when coherency was enforced.

While the limited sample size does not allow for strong conclusions, the data does yield two preliminary findings worthy of future investigation. First, the level of coherency between each axis in a multiaxial environment may affect the damage accumulation rate and should be assessed if one is trying to replicate a particular environment. Second, if a test method is used which forces coherency between components (such as the resultant PSD method) then conservative results are likely to be produced. While in many cases, a safety margin of 33% is not on its own excessive, the resultant PSD method often requires the vibration levels in certain frequency bands to be increased in a conservative manner. These multiple layers of conservative choices may result in a test specification which far exceeds the actual environment. This may be unsatisfactory in a situation where the required overbuilding results in significant negative cost or performance change.

Significant finite element modeling was performed in an attempt to understand the physics behind the empirical results. A large scale model of the structure used for the experimental work was developed. Ultimately this model could not be developed to the point of bringing better understanding to the question at hand, however, several modeling techniques were developed which may be useful to future work in this area. These modeling techniques are addressed in Appendices D, E, F, and G. Most significantly this work included:

- Two methods to create a random vibration boundary condition for time-domain analysis

- A method to reduce the time-domain transient response by proper application of initial conditions

- Discovery of an appropriate damping constant required to model a clamped-clamped FR-4 circuit card

- A modeling technique to allow for limited fixture flexibility at the boundary

In order to understand the mechanisms responsible for the increase in response and decrease in durability found during experimental testing, a simple finite element model of a rod undergoing biaxial base vibration was examined. Through this model, it was demonstrated that vibration in an axial direction can affect stress levels due to the geometric deformation produced by vibration in the transverse direction. The phase relationship and frequency ratio between the transverse and axial motion plays a critical role in determining how stress amplitude levels are affected. Depending on the phase relationship, the effect on stress amplitude can be either constructive (stress increasing) or destructive (stress decreasing); however, these two effects were found to be unequal. The stress amplitude increase for constructive phase relationships was found to be larger than the stress amplitude decrease for destructive relationships. Frequency ratio also played an important role by modulating the amount of time in which the axial vibration was of a particular phase relationship (constructive or destructive) during a single transverse cycle. Stable relationships were found to occur at whole number multiples of the transverse frequency. At odd multiples equal time is spent in constructive and destructive phase. As a result very little net effect is observed. In contrast, at two times the transverse motion frequency, the axial motion

is continuously at the same phase relationship allowing for maximum stress increase or decrease.

The studies of the beam under harmonic vibration were used to gain a better understanding of the physics affecting the beam under biaxial random vibration. Simulations were conducted with a harmonic transverse vibration and a narrowband random axial vibration. Axial vibration frequency band was varied to study the effects. Similar to the harmonic beam, the magnitude of the axial vibration effect was affected by the frequency content of the axial vibration. Vibration near the transverse frequency or three-times the transverse frequency had little or no effect. Vibration near twice the transverse frequency had maximum effect. The effect was found to vary in an unpredictable manner over time as would be expected from a random axial vibration whose phase relationship is neither stable nor predictable. It was concluded that axial vibrations which on their own would produce negligible stresses in a structure could produce significant stress increases if they were applied simultaneously with transverse vibrations producing significant geometric deformation.

6.2 Contributions

The primary contributions of this thesis to the body of knowledge of multiaxial vibration fall into two categories. The first concerns durability under uniaxial and biaxial vibration. The second is the improved understanding of the beam motion under biaxial vibration. Findings which are particularly noteworthy include:

- The direct comparison of average damage accumulation rate under biaxial vibration to the damage accumulation rates under the constituent uniaxial vibrations.

- The comparison of damage accumulation rate under coherent and incoherent biaxial vibration.

- The demonstration through FEA that vibrations which produce insignificant stresses on their own may produce large stress increases when combined with vibrations on other axes due to geometric deformation.

- The conclusion that the stress amplification effect of motion in a second axis is dependent on the frequency ratio between the two axes.

7. Limitations and Future Work

This section discusses five limitations of this study and the corresponding ways future study can address the limitation and improve the understanding of structures under multiaxial vibration.

7.1 Experimental Results are only valid for the Tested Structure

The extent of increase in the damage rate reported here for biaxial vibration, as compared to the linear summation of the damage rates of the individual components of vibration, is valid for the structure tested in this study. The factor of 2.2 difference reported here should merely be interpreted as a single data point to help understand the possible level of risk being accepted by performing multiple-step SDOF testing in lieu of MDOF testing. It should not be interpreted as a general correction factor to translate multiple-step SDOF test results to MDOF test results. Many factors including the vibration profile on each axis and the structure under test will impact how the multi-step SDOF test results relate to MDOF results.

This work intentionally focused on a structure with very high radius of gyration, which is fully expected to demonstrate a significant nonlinear cross-axis interaction, thus leading to a significant durability discrepancy between MDOF test results and multiple-step SDOF results. Future work should perform empirical studies on a broader range of structures to include structures that are likely to produce agreement between MDOF and multi-step SDOF testing. In this way, potential "safe areas" for multiple-step SDOF testing could be established.

Significant component to component variability was observed, particularly in the transverse stiffness of the leads where they entered the component body. This had an effect on the natural frequency of the component and likely affected how damage accumulated in each lead relative to the other lead. This and other effects are clearly evident when observing the large range of failure times within each set of durability tests. The large variability negatively affected the statistical significance of the results. The large difference between DARs for combined and superposition of individual components meant that despite the variability the difference in damage accumulation rate was still very significant. In the case of the coherent and incoherent vibration, the large variability resulted in a statistically weak conclusion that damage was higher under coherent vibration. Tests were conducted to examine if an effect of test sequence affected results in a multiple-step test; however, in this case the large variability obscured any conclusion on the matter.

Another related sample size consideration concerns the composition of the population. While the discussion generally compares the average time-to-failure of the six components, one must realize the six components are neither exact replicates nor tested independently. Center components (components 2 and 5) withstood different forces than edge components (components 1, 3, 4, and 6). Accelerometers created additional asymmetries between components. The author considers the aggregation of all components valid since each of the groups contained equal

numbers of each type of component. For this reason, the first component failure from the Fall testing [17] was not included.

If future empirical studies are conducted simpler structures should be studied or larger sample sizes should be planned.

7.3 Study of Cross-axis Coherence when Damage Modes are off Axis

This study compared biaxial damage accumulation under coherent and incoherent conditions between axes.   For this test specimen's orientation, each component of vibration primarily excited only one mode of the specimen. In this situation when coherent vibration was used, both modes were excited just as in incoherent MDOF testing. If the specimen has been fixtured at a different orientation (+/- 45 for the PSDs specified for the durability tests) the coherent vibration would only excite one damage mode (component only or board only, depending on the direction of fixture rotation). This would differ significantly from incoherent MDOF testing. Future work should examine the effect of test specimen orientation on the comparative damage rates under coherent and incoherent vibration.

7.4 Modeling Experimental Results using Time Domain FEA

The work in this thesis set out to perform time-domain FEA on the experimental structure. Unfortunately, modeling such a structure proved exceedingly complex. Future work should focus on developing a structure that displays a similar decrease in durability under multiaxial vibrations, but is simple enough to model in detail. The

FEA model can then be used to estimate the stress history at the failure site and perform a fatigue analysis.

7.5 Comparison between Experimental Structure and Rod-Mass Model

While Section 5.8 highlighted similarities between the experimental structure and the beam model, one must be careful not to extend the comparison too far. The effect of biaxial vibration demonstrated by the rod-mass model likely contributes to the increase in response; however, it is certainly only one of several factors which work to decrease durability under biaxial vibration. Additional work is needed to understand other effects which may contribute to the decreased durability under multiaxial vibration.

TE6-900 Vibration Test System Specifications [16]

Table Size:	200 x 200 mm (8 x 8 in.)
Frequency Range:	10 – 5,000 Hz
Table Material:	Magnesium
Rated Force	
Sine:	900 N (200 lbf)
Random:	900 Nrms (200 lbf)
Max. Acceleration	
Bare table:	295 m/sec2 (30-g)
Max. Velocity:	1500 mm/sec (60 in/sec)
Max. Displacement:	12.5 mm (0.5 in p-p)
Moving Element Mass:	4 kg (9 lb)
Cooling System:	Oil cooled
Power Supply:	230 VAC 60 Hz, 3 phase, 60 amps
Required Floor Space:	1.8-m x 1.4-m (72 in. x 54 inc.)
System Weight	1200 kgs (2650 lbs)

Appendix B

Lead Temperature Rise during Testing

One concern with the stop and re-start test technique was the effect of vibration induced heating in the component lead. In order to examine the heating of the lead during the test, an experiment was performed to measure the temperature rise during testing. This Appendix documents the method and results of that test.

A test specimen that had previously been used for a durability test was used for this experiment. At the start of the test, component six had one broken lead. No accelerometers were attached to the board or components during this test. After calibration, a J type thermocouple was attached with a small amount of solder to the left lead of component 2 on the underside of the board.   The combined random coherence profile specified in Section 2.4 was used for this test.

Lead temperature was monitored for approximately 80 minutes including test set-up, vibration, and equipment shut down. The results are shown in Figure 44. During the test, the second lead on component 6 failed completely severing the component from the test specimen. Later in the test, component 5 also failed; eventually completely separating from the test specimen. The test was terminated after 53 minutes of testing because it appeared a steady state temperature had been achieved.

A temperature rise of less than three degrees Celsius was observed in the lead during the 53 minutes of vibration. This temperature rise is considered small enough that it should not be a factor in the durability of the component lead.
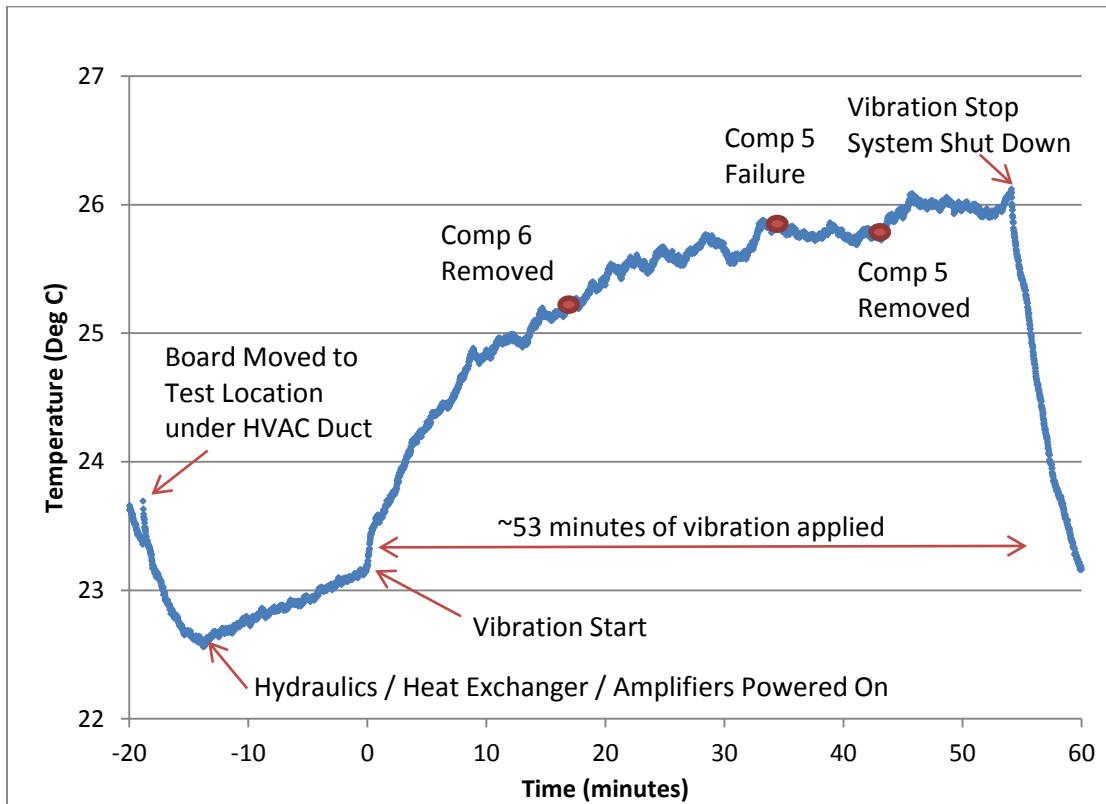
Figure 44: Durability Test Lead Temperature Rise

Appendix C

Response Data

Includes Accelerometer and Strain Gauge Data
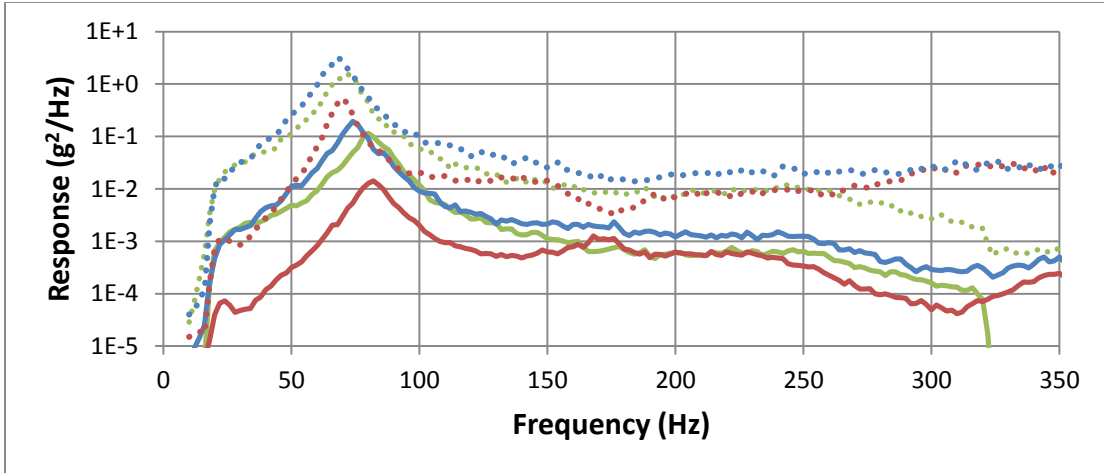
Figure 45: Component 1 X Response
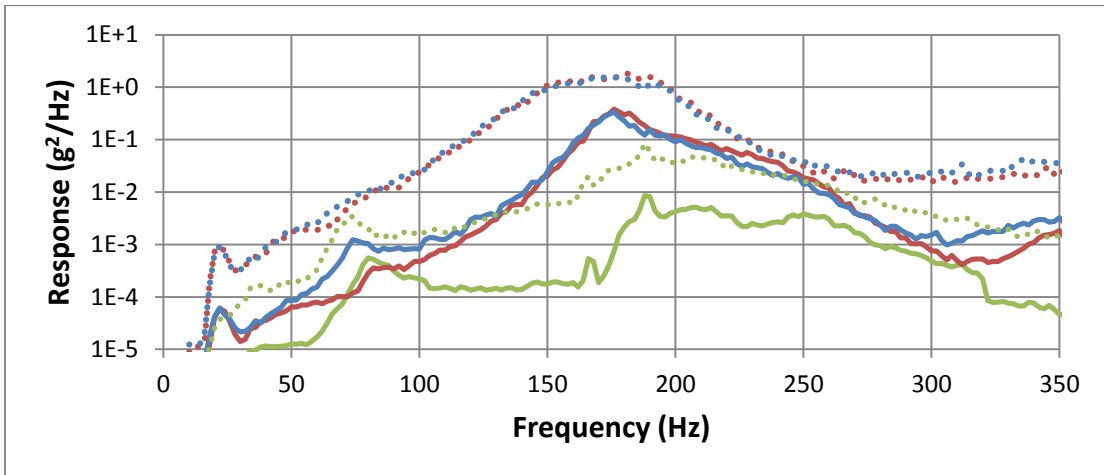
Figure 46: Component 1 Y Response

Figure 47: Component 1 Z Response

In-Plane Only -12 dB   Out-of-Plane Only -12 dB   Combined -12 dB
In-Plane Only 0 dB   Out-of-Plane Only 0 dB   Combined 0 dB

Appendix C-2
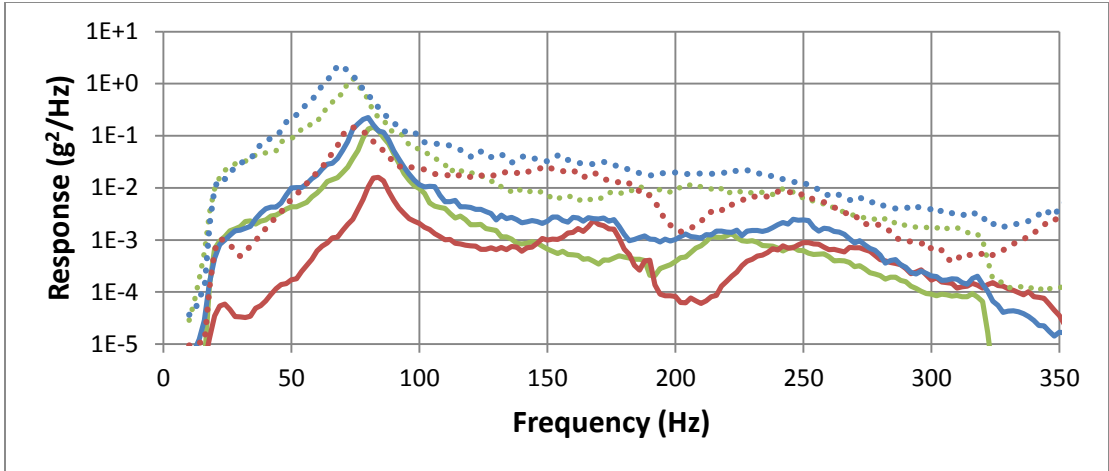
Figure 48: Component 5 X Response
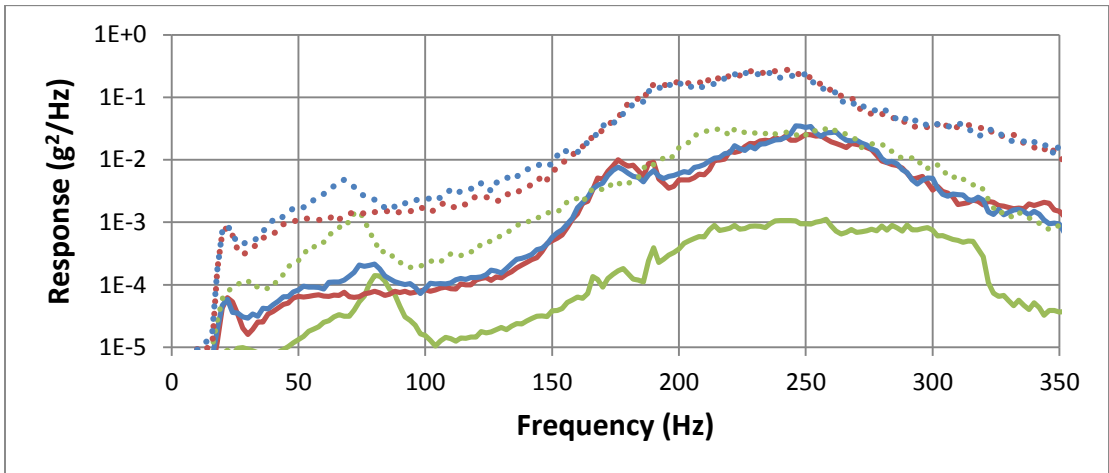
Figure 49: Component 5 Y Response
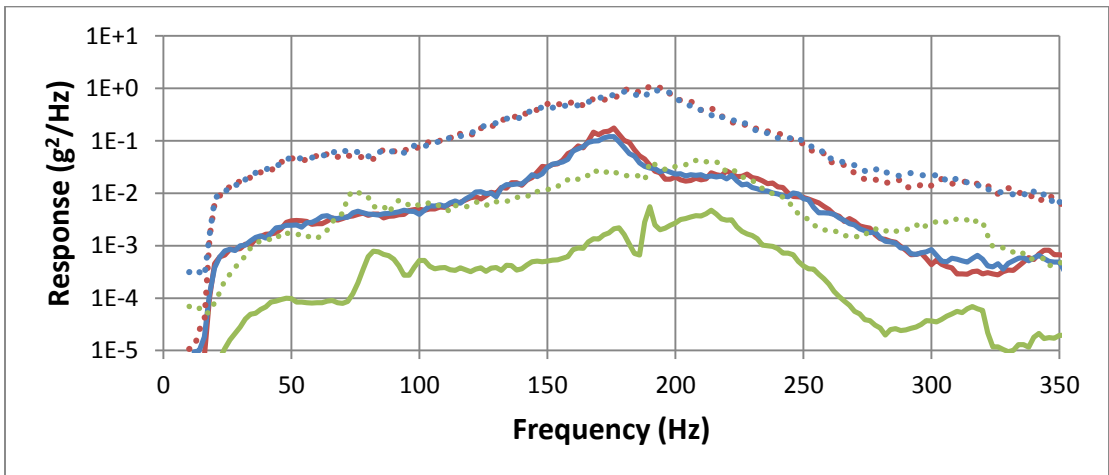
Figure 50: Component 5 Z Response

In-Plane Only -12 dB   Out-of-Plane Only -12 dB   Combined -12 dB
In-Plane Only 0 dB   Out-of-Plane Only 0 dB   Combined 0 dB

Appendix C-3
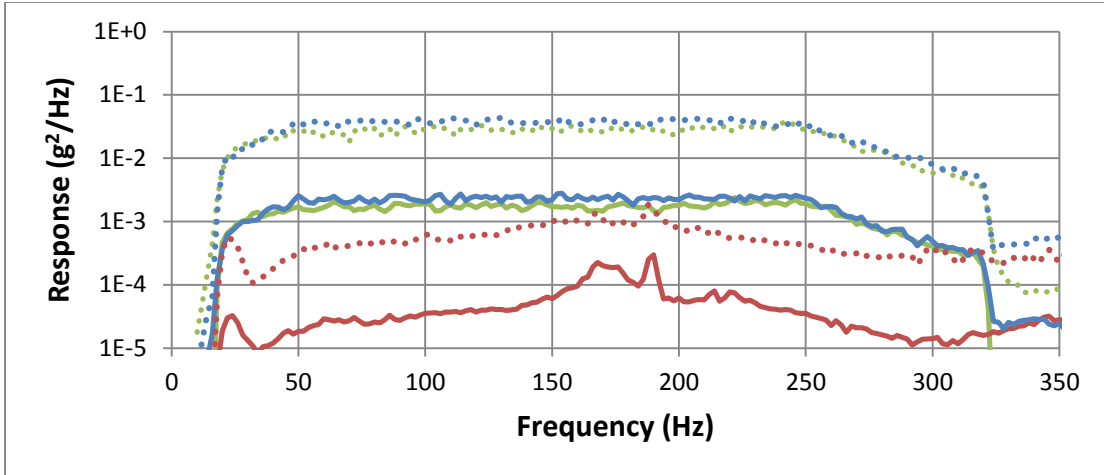
Figure 51: Board Edge X Response
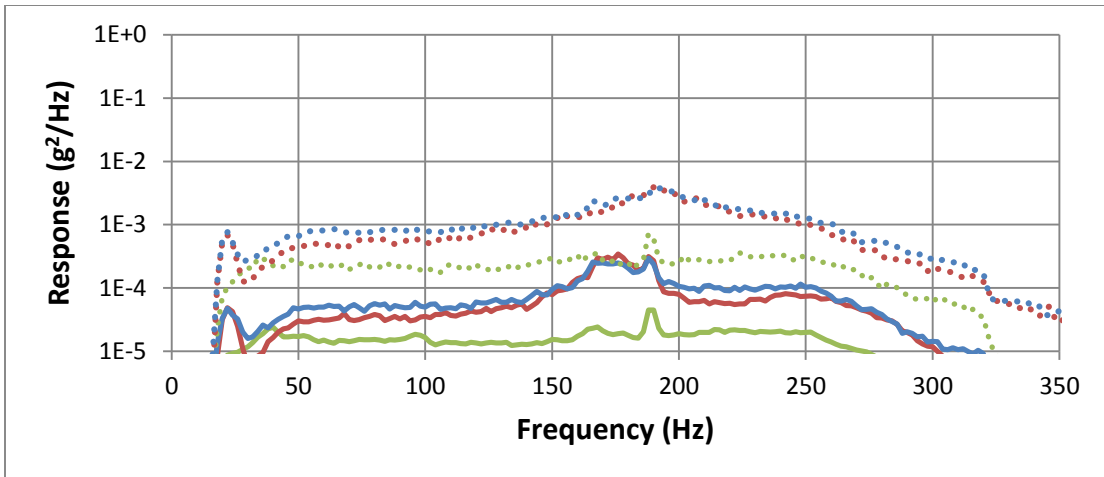
Figure 52: Board Edge Y Response
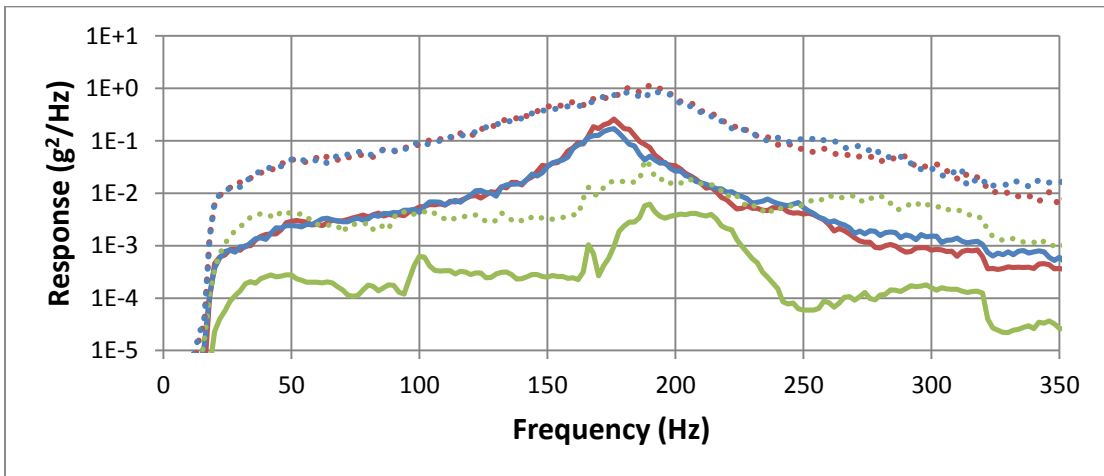
Figure 53: Board Edge Z Response

In-Plane Only -12 dB   Out-of-Plane Only -12 dB   Combined -12 dB
In-Plane Only 0 dB   Out-of-Plane Only 0 dB   Combined 0 dB
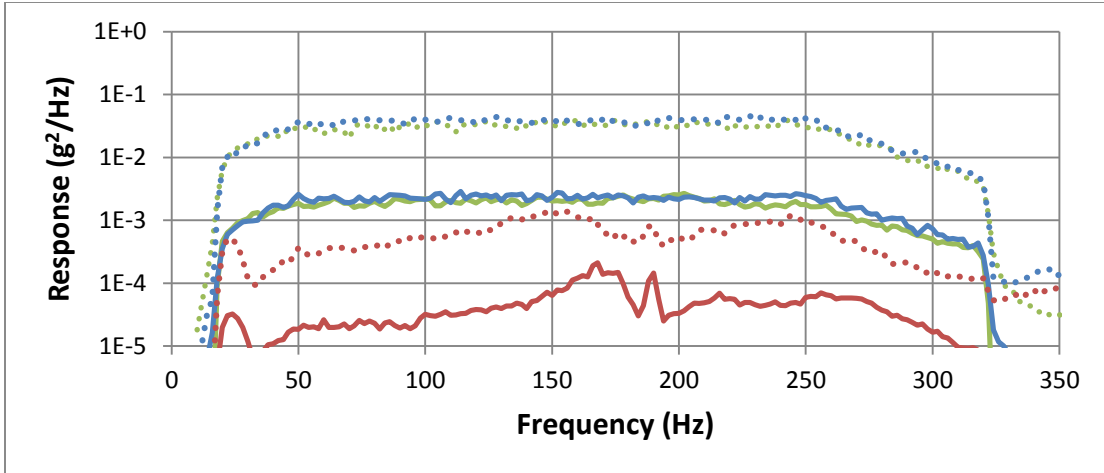
Figure 54: Board Center X Response
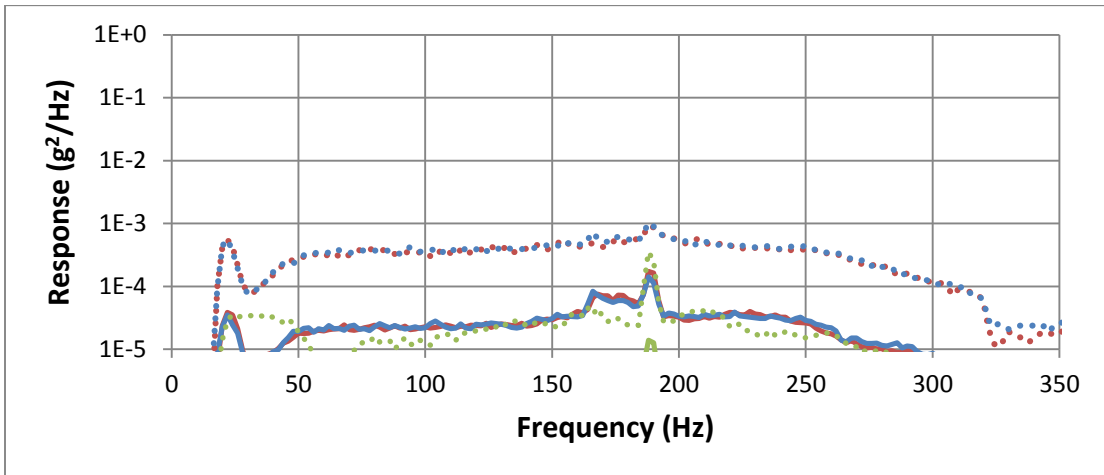
Figure 55: Board Center Y Response
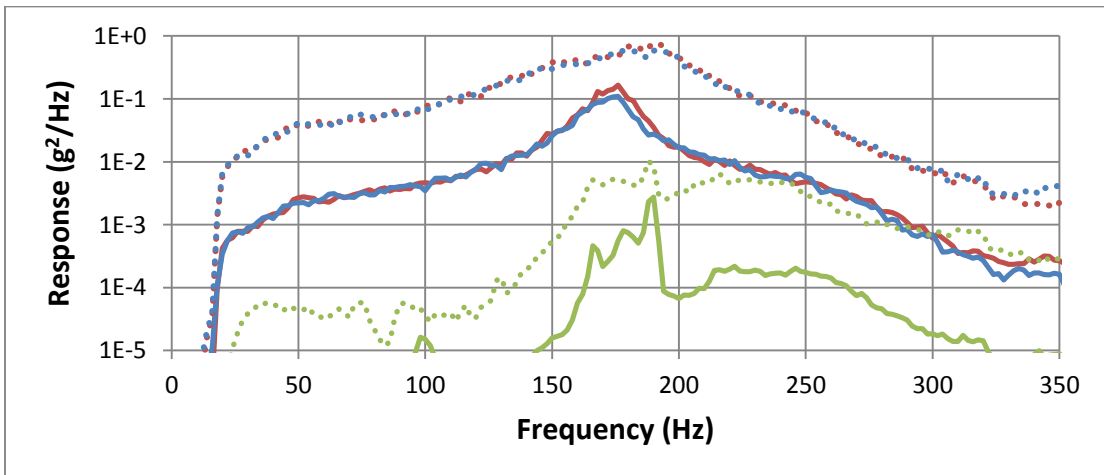
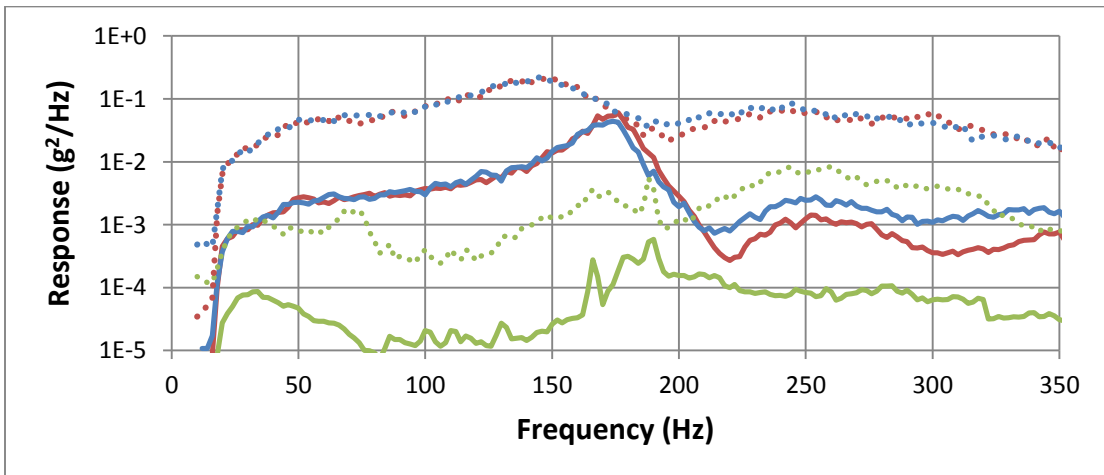**Figure 56: Board Center Z Response**

In-Plane Only -12 dB　　Out-of-Plane Only -12 dB　　Combined -12 dB
In-Plane Only 0 dB　　Out-of-Plane Only 0 dB　　Combined 0 dB

Appendix C-5

Table 9: Strain Gauge Statistics during Characterization

Vibration Direction	Level	Location	Mean	Standard Deviation	Positive 95th Percentile	Negative 95th Percentile	Max Positive	Max Negative
In-Plane Only	-12 dB	Board Fixture	2.05E-06	8.14E-06	1.53E-06	-1.15E-05	3.40E-05	-3.15E-05
		Board Edge	5.97E-07	1.00E-05	1.71E-05	-1.58E-05	3.63E-05	-3.42E-05
	0 dB	Board Fixture	1.12E-05	2.17E-05	4.60E-05	-2.48E-05	1.04E-04	-8.73E-05
		Board Edge	8.02E-06	1.60E-05	3.45E-05	-1.80E-05	7.23E-05	-6.65E-05
Out-of-Plane Only	-12 dB	Board Fixture	1.62E-05	2.21E-05	5.22E-05	-2.07E-05	1.02E-04	-7.46E-06
		Board Edge	1.25E-05	1.76E-05	4.18E-05	-1.62E-05	7.96E-05	-5.55E-05
	0 dB	Board Fixture	1.94E-05	6.96E-05	1.36E-04	-9.32E-05	3.19E-04	-2.52E-04
		Board Edge	1.61E-05	4.93E-05	9.61E-05	-6.55E-05	2.15E-04	-1.82E-04
Combined (Random)	-12 dB	Board Fixture	1.91E-05	2.13E-05	5.42E-05	-1.62E-05	1.07E-04	-6.72E-05
		Board Edge	1.53E-05	1.71E-05	4.36E-05	-1.28E-05	8.37E-05	-5.66E-05
	0 dB	Board Fixture	2.30E-05	7.08E-05	1.41E-04	-9.12E-05	3.74E-04	-2.95E-04
		Board Edge	2.03E-05	4.98E-05	1.01E-04	-6.28E-05	2.62E-04	-2.12E-04

Appendix D

Modeling a Random Vibration Boundary Condition

Method 1

The first strategy for modeling a random vibration boundary condition (BC) utilized

data captured during the experimental work performed on the TEAM six-DOF shaker

table. Accelerometer time history from the tri-axial accelerometers on the table

surface was recorded at 4096 Hz. This time history could be directly imported into

Abaqus as a tabular amplitude. Separate amplitudes would be specified for each of

the three orthogonal directions. These amplitudes would then be applied as

acceleration BCs within the load module.   Care must be taken to ensure the proper

unit conversion is used. In this case accelerometer output was in g's and the Abaqus

model used mm/s^2 so all values were multiplied by 9800. An example Abaqus

acceleration time history at the BC is shown in Figure 57. Displacement time history

is shown in Figure 58. While the acceleration looks reasonable, the displacement

history shows motion ranging from -23mm to +30mm over a two second time span.

This motion is inconsistent with the actual motion of the table observed during the

experiment.
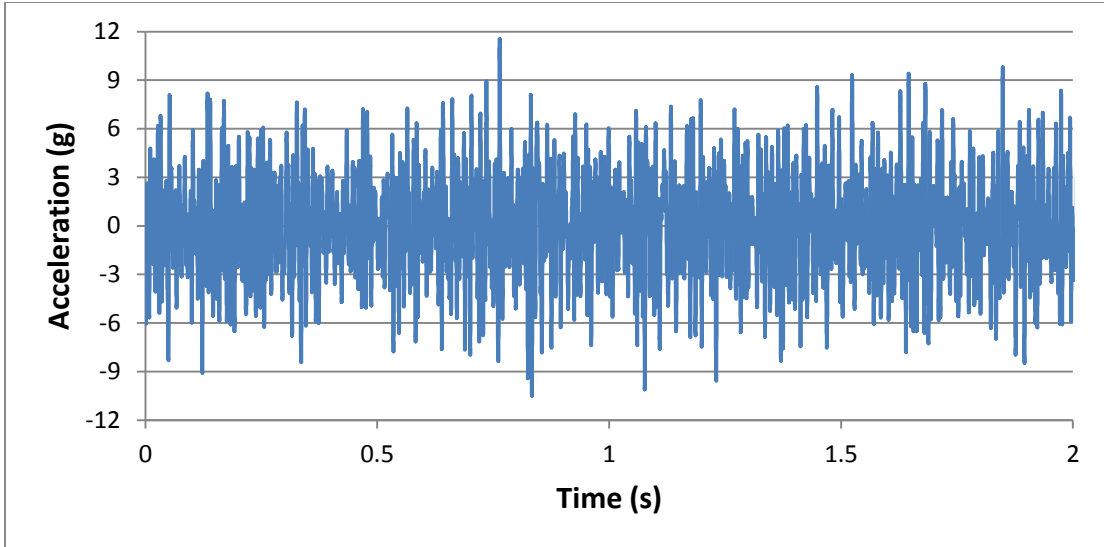
Figure 57: Boundary Acceleration
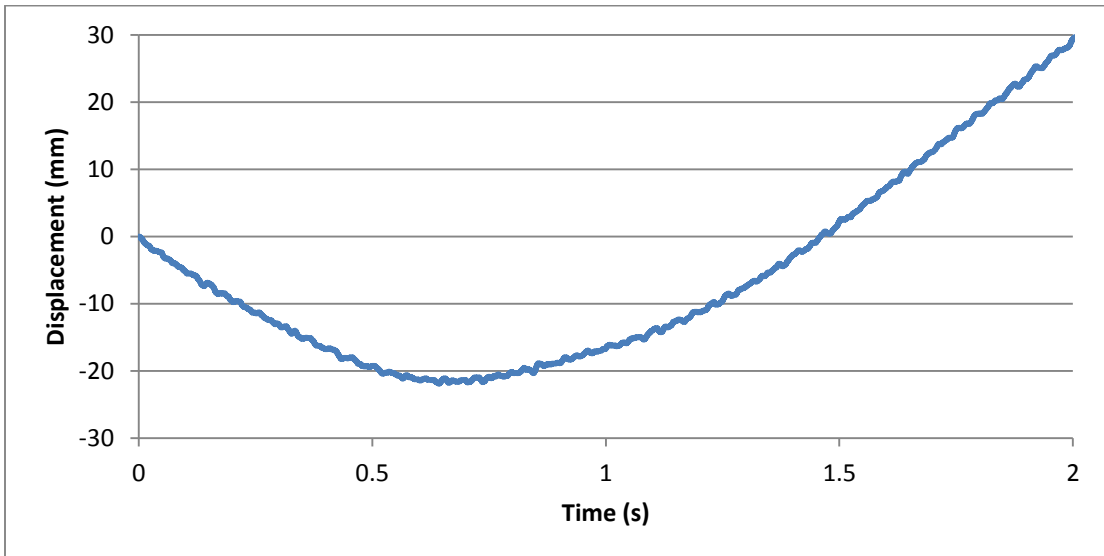
Figure 58: Boundary Displacement

The large displacements are presumed to be from two sources. The first source is likely accelerometer error caused by electrical noise. These errors are integrated twice by the finite element program along with the true accelerations to arrive at the boundary displacement. These integration errors are cumulative over time and are responsible for much of the motion shown in Figure 58. According to [20], thermal-electrical noise is greatest at low frequencies. Since the input spectrum was specified only above 20 Hz, the strategy chosen for minimizing thermal-electrical noise error

Appendix D-2

was to filter out frequency content below 10 Hz from the acceleration time history. A fourth order high pass Butterworth filter was used with a frequency cutoff at 10 Hz. When this filtered acceleration history is used as the BC within Abaqus, the resultant acceleration looks similar to the original acceleration, but much of the unrealistic displacement is removed. The acceleration and displacement histories are shown in Figure 59 and Figure 60. The figures are shown on the same scales used above. Total rigid body displacement over two seconds is less than 2 mm. A reduced vertical scale plot of displacement is shown in Figure 61.
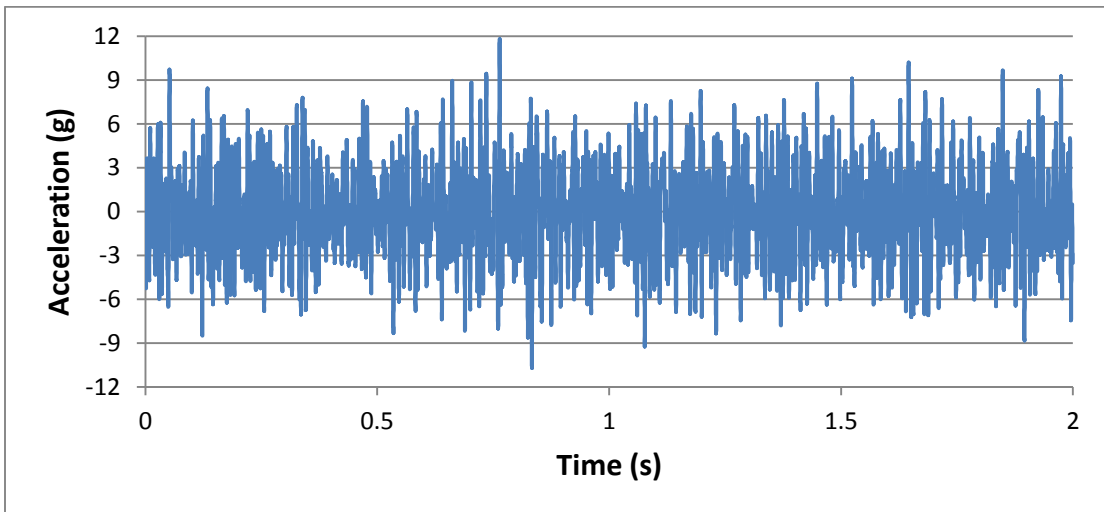
Figure 59: High Pass Filtered Boundary Acceleration
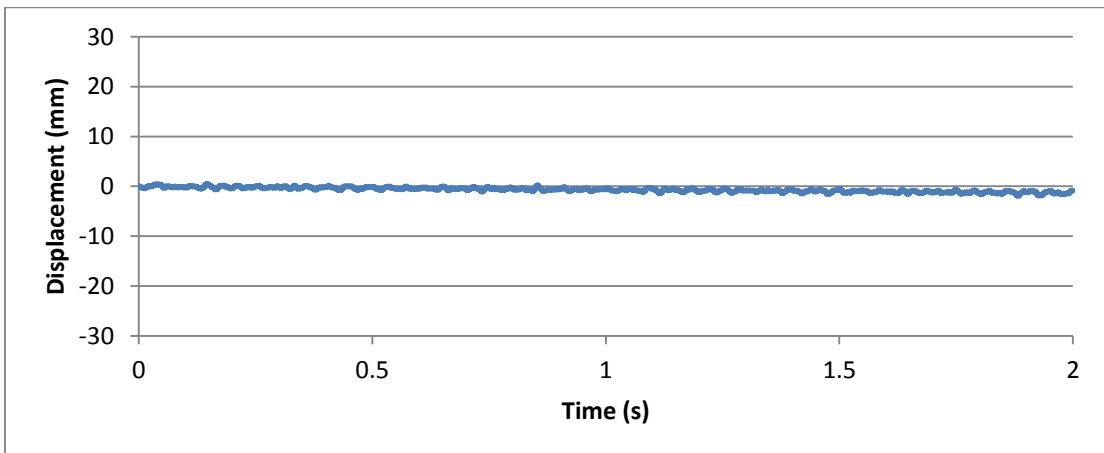
Figure 60: Boundary Displacement from Filtered Acceleration

Appendix D-3
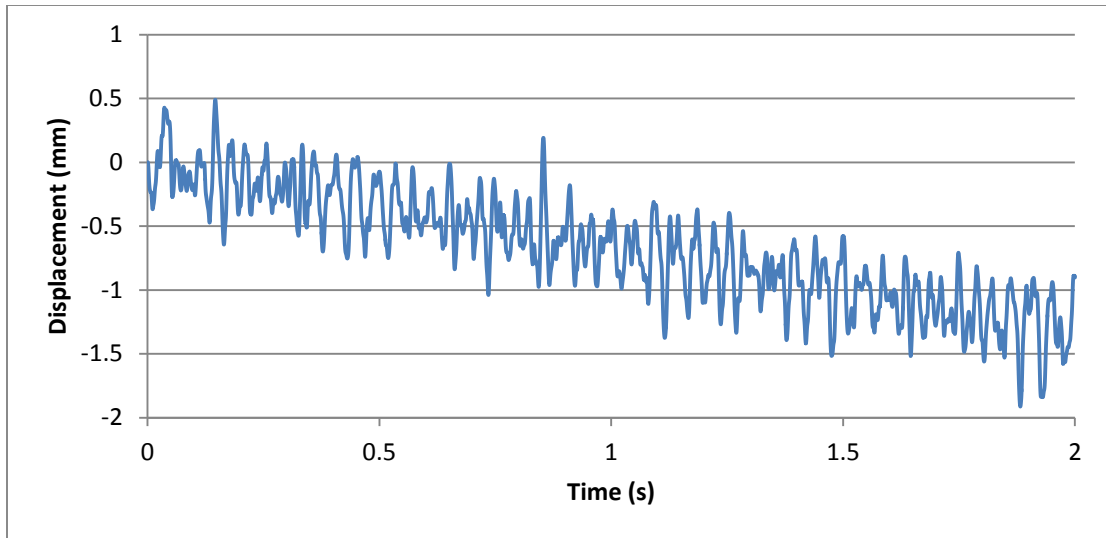
Figure 61: Zoomed Boundary Displacement from Filtered Acceleration

The second source of rigid body motion at the boundary is presumed to be incorrect initial velocity. The acceleration time history was recorded starting while the table was undergoing statistically stationary vibration. As such, the assumption is the table was not at zero velocity at the start of the acceleration history. In Figure 61, one can visualize the motion of the center of vibration with time. It appears approximately linear over the time span with a total motion of ~1.3 mm. This displacement over the two second time span equates to an average velocity of -0.65 mm/s. When an initial velocity of +0.65 mm/s is applied to the boundary the rigid body motion is removed as shown in Figure 62. Displacement is on the order of ±0.5mm.
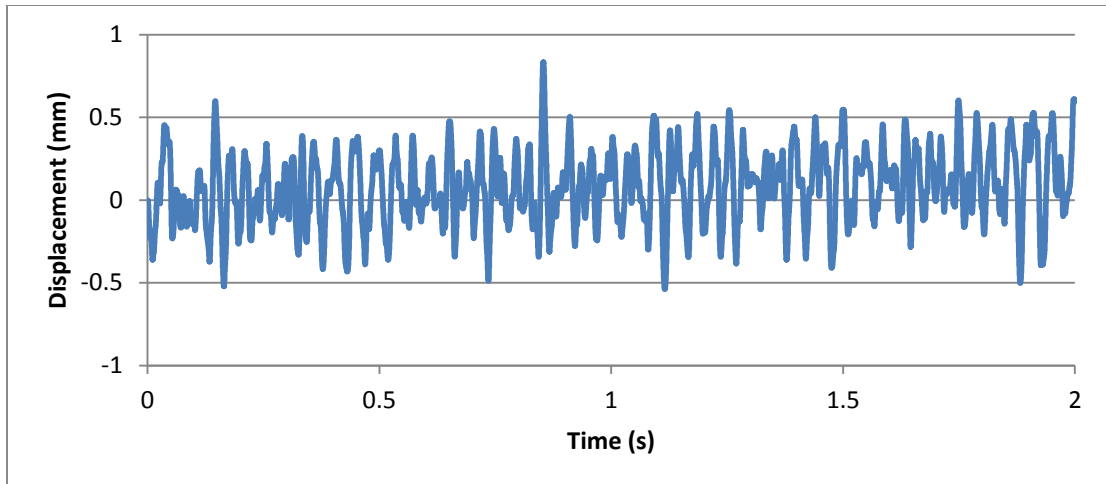
Figure 62: Boundary Displacement from Filtered Accel. with Initial Velocity

Method 2

The second strategy for modeling a random vibration boundary condition for time-domain analysis was not based on experimental data, but rather was constructed from the desired PSD definition. A PSD contains the amplitude of each frequency component in a time-domain signal, but lacks any phase information. If the time history is an ergodic stationary Gaussian random process then the phase is purely random [21]. Practically speaking this assumption allows the construction of a random vibration time-domain signal with the desired PSD. First, one needs to take the desired PSD vector and scale it according to the desired sampling frequency and length of signal. Then, each value of the PSD vector needs to be converted to a complex value by assuming an independent random phase value between $-\pi$ and $+\pi$. This complex vector is mirrored to create positive and negative parts. Finally, an inverse Fourier transform is performed to generate the time-domain signal. The mathematical process is described in a MATLAB script included in Appendix D. It should be noted, that the time-domain signal generated is not unique. Figure 63 and

Appendix D-5

Figure 64 depict an example time-domain signal and PSD for a specified PSD of 0.04 g^2/Hz over the range of 50 Hz to 300Hz. This signal can be applied to a finite element model through use of a tabular amplitude definition.
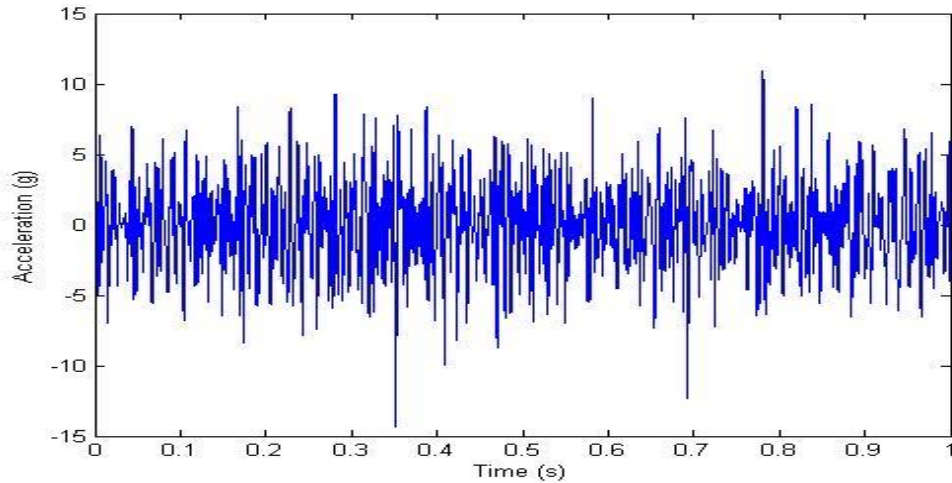
Figure 63: Time Domain Acceleration Signal for PSD shown in Figure 64
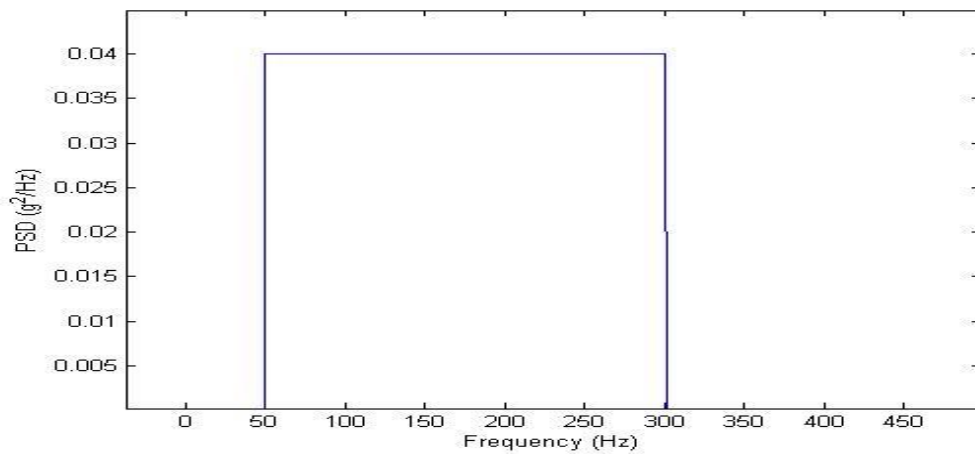
Figure 64: PSD of Signal in Figure 63

Appendix E

MATLAB script for generating a time domain vibration signal from a PSD definition and random phase assumption.

```matlab
clear;clc;

rate=4096; %Sampling rate in Hz
time=1; %Length of signal in seconds

L=time*rate;
dt=1/rate;

%%%% This section builds a suitable PSD definition %%%%%%%%%%%%%%%%

%psd must be entered as a vector of values. A value for each
%1/time Hz must be entered.  For example when time=2 a value for each
%1/2 Hz must be entered. psd(1) is the DC component.  psd(1)=dc,
%psd(2)=1/2Hz, psd(3)=1Hz etc.  Below is a loop is used to generate a
%signal with energy between a high and low frequency.

psd=zeros(1,L/2);
low=50;
high=100;
for i=low*time:high*time
   psd(i+1)=.04;   %Note, the +1 adjusts for DC;
                   %Value is the value of PSD in units^2/Hz
end

%%%% Scales the PSD based on length and rate of signal
PSD=sqrt(psd)*sqrt(rate*L/2);

%%%% Converts the PSD to a complex number with random phase
phase=(rand(1,L)-.5)*2*pi; %vector of random phase values
for n=1:L/2
    a=PSD(n)*sin(phase(n));
    b=PSD(n)*cos(phase(n));
    comp(n)=complex(a,b);
end

%%%% Mirrors the signal to create the negative frequency half.
comp2(1:L/2)=comp;
comp2(L/2+1:L)=fliplr(comp);

%%%% Performs IFFT
sig=ifft(comp2,'symmetric');

%Plots
figure(1)
plot(sig)
```

Appendix F

Computational Strategies to Minimize Transient Response during Time-Domain
Analysis of Structures under Vibratory Loading [22]

DRAFT
**Proceedings of the ASME 2013 International Technical Conference and Exhibition on Packaging and Integration
of Electronic and Photonic Microsystems
InterPACK2013
July 16-18, 2013, Berlingame, CA USA**

InterPACK2013-73200

COMPUTATIONAL STRATEGIES TO MINIMIZE TRANSIENT RESPONSE DURING TIME-DOMAIN ANALYSIS OF STRUCTURES UNDER VIBRATORY LOADING

Matthew Ernst	**Cholmin Choi**	**Abhijit Dasgupta**
University of Maryland	University of Maryland	University of Maryland
College Park, MD, 21042	College Park, MD, 21042	College Park, MD, 21042

ABSTRACT

Time-domain dynamic analysis of vibratory systems becomes useful in finite element analysis (FEA) when the structure's response can no longer be assumed linear, as frequency-domain (spectral superposition) methods require. Time-domain analysis also permits the use of cycle-counting methods when assessing the vibration durability of electronic assemblies. The analyst is often limited to simulating only the first few cycles of the vibration response in very complex models, to minimize the computational burden. However, the accuracy of time domain analysis can be questionable during these first few cycles, due to unwanted transients, unless the initial conditions are properly modeled to correctly produce the steady state response. This paper explores this sensitivity to initial conditions for undamped and damped structures. Strategies for calculating and implementing proper initial conditions within FEA are discussed. Two illustrative examples are presented for simplicity. The first consists of a simple cantilever beam so that the numerical results can be compared to known analytic solutions and the basic theory can be demonstrated. The second example is a 2D representation of a circuit card assembly containing multiple leadless chip resistor components, so that implementation details can be demonstrated for more complex structures. This paper is intended to have tutorial value to FEA users who have to conduct time-domain dynamic analysis.

1. INTRODUCTION

Frequency-domain analysis has been widely used for life prediction of solder interconnects under vibratory loading. For instance, Jih, et al [1], studied vibration fatigue of surface mount solder joints based on the response function of the displacement PSD. Yu, et al, [2] performed finite element (FE) spectral analysis of solder joints of BGA assemblies, and vibration fatigue life was estimated based on the response PSD

of the von Mises stress in the critical solder joint. However, time-domain dynamic analysis of vibratory systems becomes necessary when the structure's response can no longer be assumed linear as frequency-domain methods require. For example, Upadhyayula and Dasgupta [3] used time-domain analysis and cycle counting methods to assess the vibration durability of J-leaded PLCC interconnects. Chen, et al [4] investigated the vibration damage accumulation rate in PBGA solder interconnects using static FE analysis in the time-domain. Moreover, Zhou, et al [5] studied the vibration durability of PBGA solder joints via dynamic FE analysis of solder strain response in the time-domain.

In view of current literature on time-domain FE analysis; however, a more accurate and effective time-domain dynamic FE modeling strategy is needed, since the computational expense of complex finite element models places a practical limit on the length of the response time-window over which an analysis can be conducted. For complex models, this limit may be as short as a few cycles of a vibratory system. To cope with this problem, some authors [3], [5] and [6] have resorted to the use of nonlinear transfer functions that approximate the strain history in the solder from measured strain histories on the PWB. In this approach, only a few steady-state response cycles are modeled using time-domain nonlinear dynamic FEA analysis. However, if the initial conditions applied to the model do not match the steady-state conditions the early cycles of the response are dominated by erroneous transients as the system moves from its initial conditions to its steady-state conditions. For lightly damped structures, this erroneous transient response period may exceed the practical time limit of the simulation. However, correct estimation and application of the initial condition to all parts of the structure (all degrees of freedom at all nodes in the context of FEA) can be a non-trivial task. Therefore, this paper focuses on effective strategies to implement the proper initial conditions to allow the simulation

to approach the steady-state response within as few cycles as possible, to minimize the computational burden.

NOMENCLATURE

l is the beam length
b is the beam width
h is the beam height
A is the amplitude of base oscillation
u is the displacement of the beam
t is the time
ω is the frequency of forcing function or base oscillation
ω_n is the natural frequency
ω_j is the modal natural frequency (j=1,2,3,4…)
ζ_j is the modal damping value (j=1,2,3,4…)
u_0 is the initial displacement
v_0 is the initial velocity
x is the longitudinal position or node location
E is the indeterminate Eigenvector multiplier
eig(x) is the Eigenvector value for node x
ψ is the phase difference

The presence of an overbar indicates a vector

2. THEORY

For the purpose of discussing the underlying theory it is informative to first consider a simple undamped single-degree-of-freedom spring-mass oscillator subjected to harmonic sinusoidal motion at the base of the spring. The solution to the differential equations of dynamic motion are known to consist of a transient solution at the natural frequency, whose amplitude and phase are governed by the initial conditions (first term on the right hand side of Equation 1) and a steady state solution at the forcing frequency, whose amplitude is governed by the amplitude and frequency of the base oscillation (last term on the right hand side of Equation 1). If one wishes to start a simulation at the steady state condition, proper initial conditions must be specified such that the amplitude of the first term is zero. A more detailed derivation of the equations of motion for a SDOF oscillator can be found in the literature [7].

$$u(t) = C\cos(\omega_n t + \phi) + \frac{A\omega_n^2}{(\omega_n^2 - \omega^2)}\sin\omega t$$

Equation 1

Where:

$$C = \sqrt{u_0^2 + \left(\frac{v_0}{\omega_n} - A\omega\left(\frac{\omega_n}{\omega_n^2 - \omega^2}\right)\right)^2}$$

Equation 2

$$\phi = \tan^{-1}\left(\frac{u_0\omega_n}{v_0 - A\omega\frac{\omega_n^2}{\omega_n^2 - \omega^2}}\right)$$

Equation 3

A similar relationship is required in order to remove the transient response in any continuous structure, where the initial condition becomes a spatial function, related to the eigen vectors of the problem. This relationship requires the initial excitation, deformation, and velocity fields to be consistent with the steady state motion. Failure to apply these initial conditions results in a secondary amplitude modulation. As an example we will first consider a simple FEA model of a cantilever beam below, since the analytic solution for this simple structure is well known in the literature. In the final section of this paper we will consider the challenges of applying such initial fields to FEA models of more complex structures, such as a circuit card assembly.

3. EXAMPLE STRUCTURE AND MODEL

Consider a simple cantilevered beam, as shown in Figure 1, to demonstrate the fundamental concepts discussed above in Section 2. We will explore a series of model refinements to demonstrate how neglecting certain aspects of the initial conditions can affect the modeled response.

Material properties were selected to approximate aluminum. A linear elastic constitutive property was specified with a Young's modulus of 79 GPa and Poisson's ration of 0.3. Density was 2600 kg/m^3. Examples are considered with no damping as well as with Rayleigh damping of α=96.49 and β=4.91e-5. The finite element model uses 10 linear Euler-Bernoulli beam elements (B23 elements). The beam has one free end and one clamped end. The clamped end allows no rotation and no translation in the axial direction. A base motion is applied to the transverse direction of the clamped end. Displacement amplitude of 1 mm at a frequency of 78 Hz is specified. The analysis is restricted to two-dimensional space to allow easy verification against the analytic solution in Equation 4. The natural frequencies of the first two resulting modes are 88 Hz and 523 Hz.
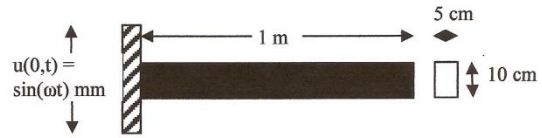
Figure 1: Beam Geometry and Base Excitation

A complete derivation of an analytic solution for the cantilevered beam can be found in [8]. The steady state solution for the motion of the beam is presented in Equation 4.

$$u(x,t) = 2A\sum_{j=1,2,3…}^{\infty}\frac{\gamma_j}{\lambda_j l}\frac{\left(\frac{\omega}{\omega_j}\right)^2\Phi(x)}{\left\{\left(1 - \left(\frac{\omega}{\omega_j}\right)^2\right)^2 + \left(2\zeta_j\frac{\omega}{\omega_j}\right)^2\right\}^{1/2}}\sin\omega t$$

Equation 4

Where:

$$\gamma_j = \frac{\cos \lambda_j l + \cosh \lambda_j l}{\sin \lambda_j l + \sinh \lambda_j l}$$
Equation 5

$$\Phi(x) = \cos \lambda_j x - \cosh \lambda_j x - A(\sin \lambda_j x - \sinh \lambda_j x)$$
Equation 6

$\lambda_j l$ is found by solving the transcendental equation of the cantilevered beam. The first four values are given in Table 1 for reference.

j	$\lambda_j l$
1	1.875
2	4.694
3	7.855
4	10.996

Table 1

It is also useful to note that the modal damping values of Equation 4 can be related to the Rayleigh damping values (α and β) through Equation 7.

$$\alpha + \beta \omega_j^2 = 2\zeta_j \omega_j$$
Equation 7

4. MODELING STRUCTURES WITHOUT DAMPING

A time-domain FEA solution to constant-amplitude harmonic (sinusoidal) excitation is presented here for the beam shown in Figure 1. The steady state solution at any point of the beam should therefore be a constant-amplitude harmonic motion at the excitation frequency. Figure 2 shows the correct steady state response of the tip of the beam and the base motion, based on the analytic solution in Equation 4. Clearly the velocity field will be non-zero each time the beam passes through its undeformed configuration. This velocity field represents the correct initial condition if we wish to conduct an FEA simulation for the steady-state response, starting with the undeformed beam. However if the analysis is conducted instead starting with the undeformed beam incorrectly at rest, the response is as shown in Figure 3. This amplitude modulation on top of the steady-state constant-amplitude harmonic response will persist forever. For damped structures the amplitude of this modulation will decay with time, with the decay rates being proportional to the magnitude of the applied damping.
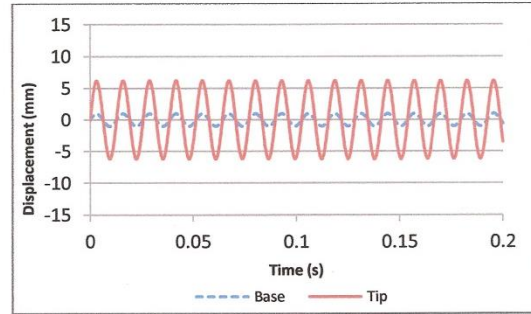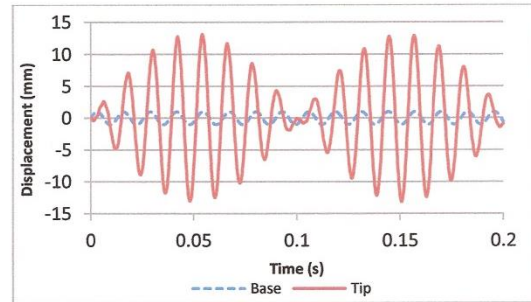

Figure 2: Undamped Beam Steady State Response

Figure 3: Undamped Beam Response without Initial Velocity

The range of permissible conditions to remove the transient includes all conditions which are found on the steady state solution. In the case of the beam, these range from a zero velocity condition in the most deformed configuration to the maximum velocity field in an undeformed beam. While any of these conditions can be used, the easiest to implement in finite element software is the undeformed condition with the maximum initial velocity field. In this case the undeformed structure is modeled and an initial velocity field is applied to each node. When damping is not included, the beam response will be either in-phase with the excitation or 180 degrees out of phase depending on the if the forcing frequency is below or above the natural frequency. Therefore, since the initial displacement is zero, the base motion can be modeled simply as a sine function. For cases where the response is approximately uni-modal, the relative shape of this initial velocity field is the same as the eigenvector corresponding to the mode which is excited. The eigenvector can easily be obtained through finite element modal analysis; however, the amplitude is indeterminate. One must estimate the approximate response and scale the velocity field to that value. While this approximate initial condition will not produce the exact steady state solution, it will most likely produce a better result than ignoring the initial velocity altogether.

3

The modeler should be aware of two common pitfalls when calculating and applying the initial velocity field. First, the correct initial velocity must be applied to each degree-of-freedom (DOF) at every node. While it is obvious, that initial transverse velocity must be applied to the beam, one must also apply proper initial rotational velocity to each node, since Euler-Bernoulli beam elements in FEA use C^1 shape functions based on both displacement and rotation DOFs. The result of neglecting the initial rotational velocity field causes transients with high frequency mode shapes to appear. While these high frequency modes do not produce much displacement, they are very evident in the tip acceleration history shown in Figure 4. Interestingly, even when no Rayleigh damping is applied to the model, these high frequencies diminish with time due to insufficient time step size. If the time step size was reduced these high frequency motions would persist longer.
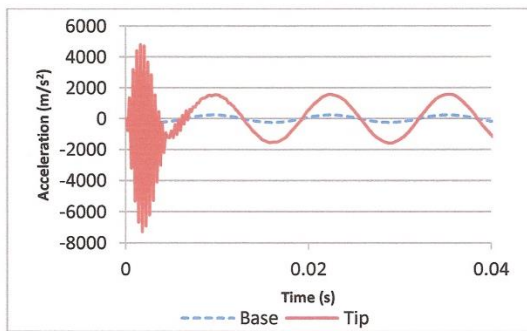

Figure 4: High Frequency Transients

A second pitfall is selection of the proper reference frame for applying the initial velocity field. The eigenvectors are calculated in a reference frame that is fixed to the base. However, velocities must be applied in the inertial frame. Therefore, the initial velocity of the base must be added to the velocity determined through modal analysis. Taking these factors into account

$$\overline{v_0}(x) = E_1 \cdot \overline{eig}(x) + \overline{A}\omega$$

Equation 8: Initial Velocity Field (Undamped)

5. MODELING STRUCTURES WITH DAMPING

When damping is present, additional factors must be considered. First, unlike the undamped model, the damped model will converge to the steady state solution as simulation time is increased. The time to arrive at the steady state solution will decrease as the magnitude of damping is increased. For our model, we will use first and second mode damping ratios of 10% each for purposes of illustration. This implies that at the first and second modal frequencies, 10% of the transient response will be removed with each cycle. This will be implemented in the finite element model through Rayleigh damping with α=96.49 and β=4.91e-5.

Just as with the undamped model, a proper initial excitation, displacement and velocity need to be applied to each DOF at each node to eliminate the transient response. Figure 5 shows the result of beginning the simulation with zero initial velocity throughout an undeformed model. As with the undamped beam response presented in Figure 3, the damped beam response initially starts out smaller than steady state, then grows to a larger response than steady state. This solution differs from the undamped response since the transient component of the response is damped out as the simulation proceeds in time until the steady state condition is achieved.
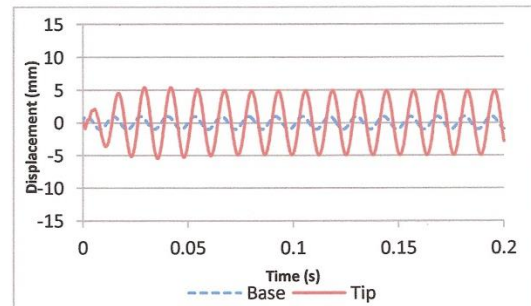
Figure 5: Damped Tip Displacement without Initial Velocity

Damping complicates the calculation and application of initial conditions by introducing a phase difference between excitation and response. If the excitation is applied in phase with the response, even a model with the correct initial deformation and velocity will yield an initial transient as shown in Figure 5. Since moderate damping is present in Figure 5, the solution arrives at steady stare within the simulation time.

Figure 6: Transient Due to Phase Difference

It remains easiest to begin the simulation at the moment where the structure is undeformed. The base motion then must

4   Copyright © 2013 by ASME

Appendix F-5

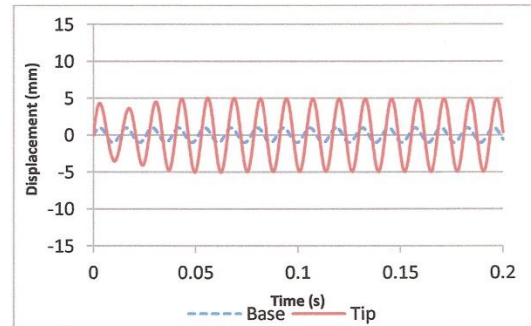be shifted by the phase lead or phase lag. Generally this can be implemented in finite element software as a sum of sine and cosine functions rather than a pure sine function as used for the undamped case.

Since the base must be out-of-phase with the beam motion, it is no longer at its maximum velocity at the start of the simulation. Therefore, initial base velocity will be the maximum velocity multiplied by the cosine of the phase difference. Additionally, a different multiplier must be used for the damped case. The new equation for the velocity at each node is:

$$\overline{v_0}(x) = E_2 \cdot \overline{eig}(x) + \overline{A}\omega \cos\psi$$

Equation 9: Initial Velocity Field (Damped)

Much like the eigenmode scaler, no procedure exists for calculating the phase difference for an arbitrary structure, but one can start with an initial estimate and iteratively refine this choice. When the proper phase shift is accounted for, the result is a simulation which begins at steady state as shown in Figure 7. There are two important features worth noticing in Figure 7. The response now lags the base by a phase angle ψ and the system no longer oscillates about zero. The fact that the oscillation is not about zero is due to the fact that the shift in the phase of the base excitation resulted in an initial start point not at the center of its cycle.
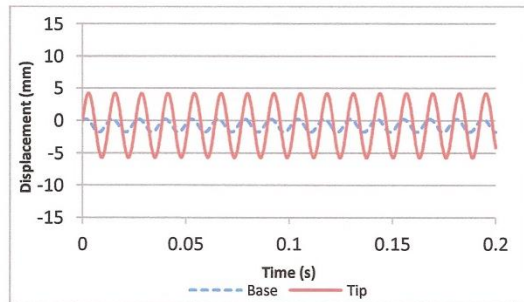

Figure 7: Damped Beam Steady State

6. APPLICATION TO CIRCUIT BOARD MODEL

The principles outlined above were applied to a 2D finite element model of a circuit board with several leadless chip resistor (LCR) packages mounted on the top side of the board, as shown in Figure 8. Model geometry and material properties are omitted here in the interest of brevity. This board was clamped at the two edges and subjected to a harmonic vibration near its natural frequency at the two edges, with a constant-amplitude harmonic excitation with peak acceleration of 1G. The aim of using this model in this paper is to explore the challenges in implementing the modeling strategies outlined above to minimize the transient response of the board displacement due to a dynamic acceleration loading. The ultimate future goal of the model is to extract the correct steady-state dynamic stress-strain response of the solder interconnects with the shortest possible response window, in order to minimize the computational burden.

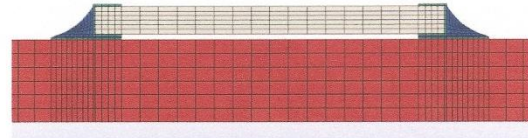**Figure 8: Model of Circuit Board with LCR Packages**

Figure 9: Detail of LCR Package on Circuit Board

When the simulation is started from an undeformed state with no initial velocity, the model's response is shown in Figure 10. As in the beam's response in Figure 3, the transient response amplitude begins at zero, but overshoots the steady state amplitude.
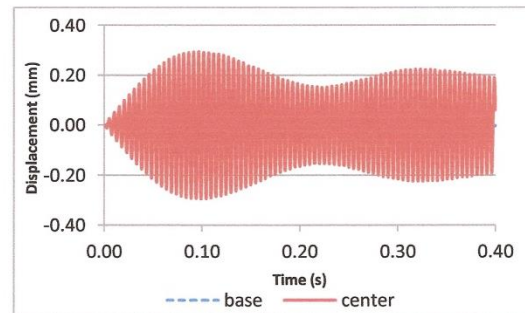

Figure 10: LCR Board Center Displacement without Any Initial Velocity

The same principles outlined for the beam in Section 3 can be applied to this more complex model. The eigenvector is obtained from the FEA modal analysis. The scale factor for the initial velocity field can be estimated either from experimental data (if available), or from simpler approximate analytic models (such as a clamped-clamped beam in this case), or by an iterative parametric FEA approach based on the trends observed from the first few cycles. When a reasonably accurate initial velocity field is applied to the finite element model, the result shown in Figure 11 is obtained. The large initial transients are clearly minimized and the model is nearly at steady state from the onset of the simulation.
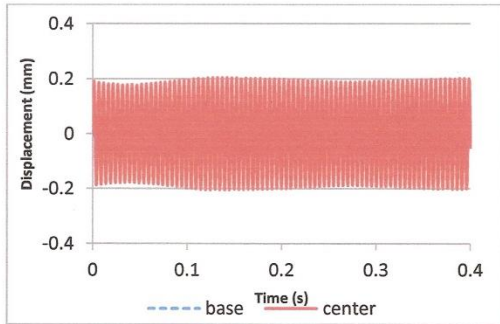
5

Appendix F-6

Figure 11: LCR Board Center Displacement with Satisfactory Initial Velocity Field

7. SUMMARY

In this paper, strategies for minimizing the transient response during time-domain finite element analysis of structures under dynamic vibratory loading were discussed. As an example, approximate initial conditions were extracted via frequency domain modal analysis and from theoretical solutions for a simple cantilever beam. Similar principles were employed to obtain the steady-state initial conditions for a more complex circuit card assembly. Moreover, the effect of damping and its associated factors such as phase difference on the transient and steady-state response was considered.

In the future, the same principles will be applied to more complex three-dimensional damped structures for a significant reduction of the computational burden for time-domain FEA dynamic response analysis. The goal is extraction of more accurate dynamic stress-stain response of solder interconnects due to dynamic excitation of complex electronic systems.

REFERENCES

[1] Jih, E., and Jung, W., "Vibration Fatigue of Surface Mount Solder Joints", IEEE InterSociety Conference on Thermal Phenomena, pp. 246-250, 1998

[2] Yu, D., Al-Yafawi, A., Nguyen, T., Park, S., and Chung, S., "High-cycle Fatigue Life Prediction for Pb-free BGA under Random Vibration Loading," *Microelectronics Reliability*, No. 51, pp.649-656, Oct 2010

[3] Upadhyayula, K. and Dasgupta, A., "Physics-of-Failure Guidelines for Accelerated Qualification of Electronic Systems," *Quality and Reliability Engineering International*, Vol 14, pages 433–447, 1998.

[4] Chen, Y., Wang, C., Yang, Y., "Combining vibration test with finite element analysis for the fatigue life estimation of PBGA components," *Microelectronics Reliability*, Volume 48, Issue 4, Pages 638-644, April 2008

[5] Zhou, Y., Al-Bassyiouni, M., and Dasgupta, A., "Harmonic and Random Vibration Durability of SAC305 and Sn37pb Solder Alloys," *IEEE Trans Components & Packaging Tech*, Vol. 33, No. 2, pp. 319-328, 2010.

[6] Zhou, Y., Al-Bassyiouni, M., and Dasgupta, A., "Sources of Fatigue in Random-Vibration Durability of Surface Mount Interconnects," InterPACK ASME Conf. Proc. 143, 2009

[7] Meirovitch, L., *Fundamentals of Vibrations*, New York: McGraw-Hill, 2001

[8] Barnoski, R. L., "Response of Elastic Structures to Deterministic and Random Vibration," Air Force Flight Dynmaics Laboratory, Wright-Patterson AFB, OH, 1965.

Appendix F-7

Appendix G

A Description of the Test Specimen Finite Element Model

1. Overview

The original intent of performing a finite element analysis (FEA) on the test specimen was to create a model which would allow the investigators to understand the effects several types of vibration had on the stress time history at the failure site. The model described in this Appendix was to serve as a global model designed to capture the dynamics of the card throughout the structure. It was to be calibrated to match the data acquired during characterization testing. A follow-on local model was to be created which would model the failure site location in more detail. The dynamics to define the boundary of the local model would be extracted from the global model.

This document will describe each section of the global model. It would be critically important for anyone wishing to perform further work on the model, but could also be useful to anyone who wishes to perform time-domain dynamic analysis using FEA. This document assumes moderate familiarity with ABAQUS/CAE. Reference to the ABAQUS/CAE User's Manual [23] may be necessary. Figure 65 shows the entire model assembly.
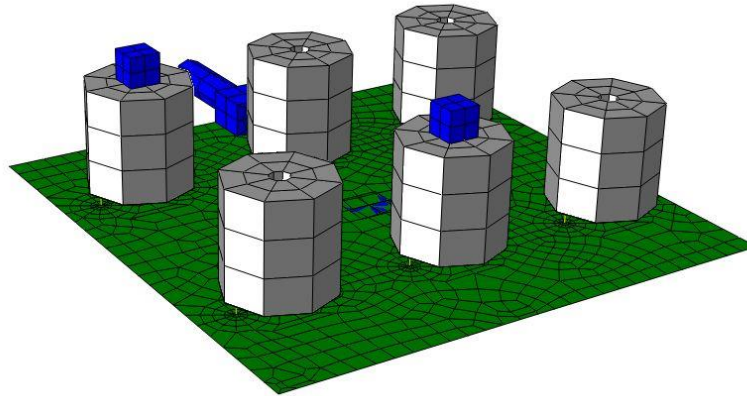
Figure 65: Full Model

2 Geometry and Properties

2.1 Circuit Board

The circuit board was modeled as a 101.6 mm x 101.6 mm shell meshed with 1510

S4R elements. Shell element thickness was 1.7 mm. Density was 2 g/cm^3.

Orthotropic material properties for FR-4 material were obtained from Stuart Douglas'

Master's Thesis [24] and are listed in Table 10 and Table 11. Both tables display the

same information just in two different forms.

Table 10: Board Elastic Properties

E_1 (MPa)	E_2 (MPa)	E_3 (MPa)	ν_{12} (MPa)	ν_{21} (MPa)	ν_{23} (MPa)	ν_{32} (MPa)	ν_{13} (MPa)	ν_{31} (MPa)	G_{12} (MPa)	G_{23} (MPa)	G_{13} (MPa)
19000	19000	9000	.14	.14	.39	.18	.39	.18	3700	2900	2900

Table 11: Board Compliance Matrix (ABAQUS Format)

D1111 (MPa)	D1122 (MPa)	D2222 (MPa)	D1133 (MPa)	D2233 (MPa)	D3333 (MPa)	D1212 (MPa)	D1313 (MPa)	D2323 (MPa)
21535	4868	21535	4752	4752	10755	3700	2900	2900

Mass proportional Rayleigh Damping with α=2000 was applied. The proper value

was determined by adjusting α until the standard deviation of the board center's

acceleration response in the FEA model approximately matched the standard

deviation of the experimentally measured acceleration response at the board center.

Figure 66 and Figure 67 compare FEA and experimental acceleration history at the

center of the board for α=600 and α=2000. Table 12 compares the standard deviation

for a 1 second time history. One can clearly see that α=2000 is a better match than

α=600. In fact, damping slightly higher than 2000 would be required to exactly
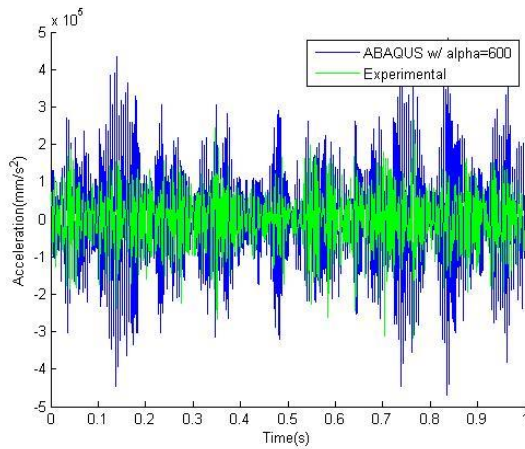
match the standard deviation values.
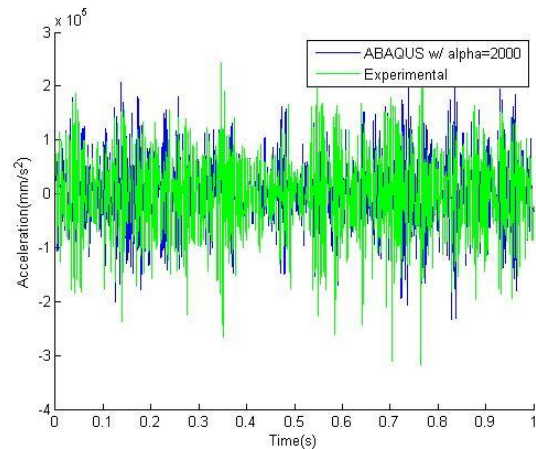

Figure 66: FEA and Experimental Comparison for α=600

Figure 67: FEA and Experimental Comparison for α=2000

Table 12: Standard Deviation Comparison

	Standard Deviation
Experimental	7.01E+04
FEA (α=600)	1.42E+05
FEA (α=2000)	7.31E+04

In addition to the peak accelerations being too high, a low damping value causes

response transients to persist in the response over several cycles. Notice the response

in Figure 68 has a 'blocky' appearance where large or small amplitudes will be

present for several cycles in a row. Transition from small to large amplitude

accelerations takes several cycles to complete. Compare Figure 68 with Figure 69

where a larger damping value is used. In this case, transition from large to small

Appendix G-3

amplitudes is accomplished cycle-to-cycle giving a much more random appearance.

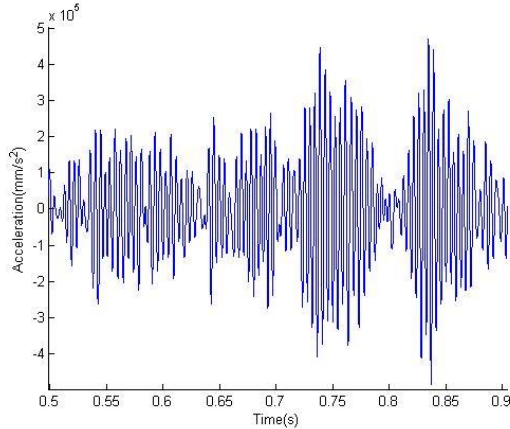The overall trend observed with the higher damping value matches experiment.
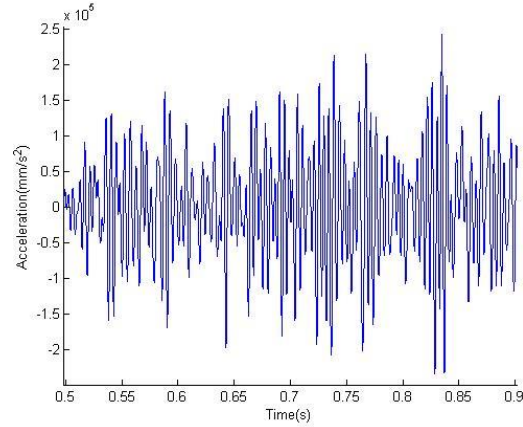

Figure 68: FEA Response with α=600

Figure 69: FEA Response with α=2000
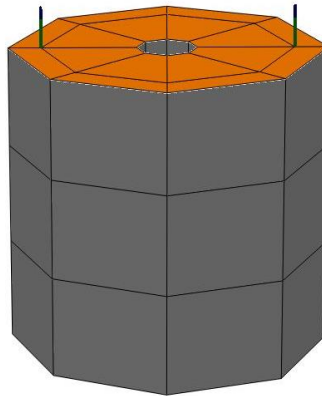
2.2 Inductor

Figure 70: Inductor and Leads

Considerable simplification was made to model the inductor. The inductor was

treated as a body of uniform density and two leads attaching the inductor body to the

circuit board. The inductor body (grey material in Figure 70) was modeled as thick

walled cylinder with 21 mm outside diameter, 4 mm inside diameter, and 20.52 mm

length. It was meshed using 48 C3D8R brick elements. The total component body

mass of 23 g was uniformly distributed over the volume using a material density of

3.36 g/mm^3. It was desired that the inductor body would behave rigidly so isotropic

elastic properties with E=100,000 MPa and v=0.3 were used. Rayleigh damping with

α=200 was used although analysis did not proceed to the point of determining the

correct alpha value.

In order to provide additional flexibility for attaching the leads to the inductor body,

rotational degrees of freedom on the bottom surface were required. Since 3D brick

elements were used for the body, only translational DOF were available. In order to

add rotational degrees of freedom, a bottom surface of the inductor body (orange

material in Figure 70) was modeled with 16 S4R shell elements. In order that this

shell have minimal effect on the component mass and continue to approximate a rigid

body, the shell was specified as 1 mm thick with elastic properties of E=100,000

MPa, v=0.3 and a density of 0.1g/cm^3. This shell was constrained to the inductor

body using a tie constraint. Each node of the shell had its translational DOFs tied to

the corresponding node on the lower surface of the inductor body.
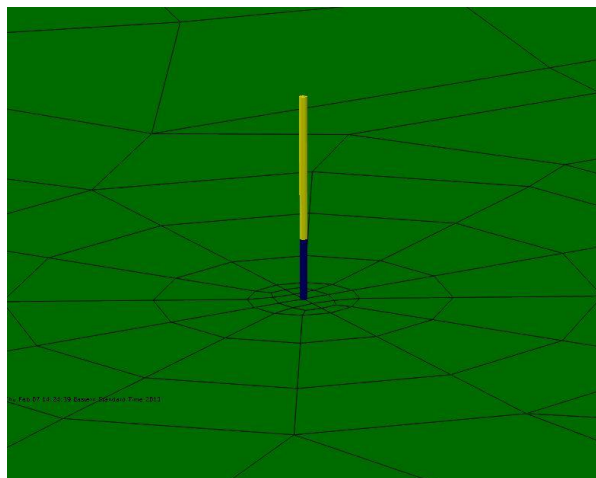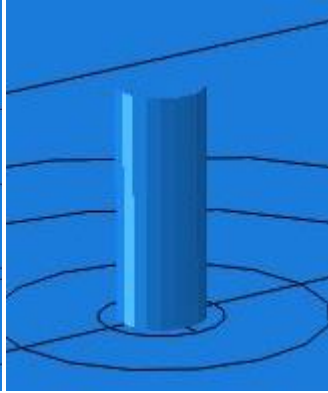
2.3 Leads

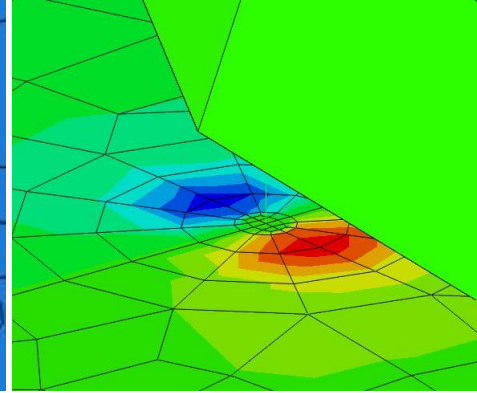**Figure 71: Lead on Circuit Card (Inductor Removed)**

Each lead (two per component) was modeled as two separate parts. One part represented the portion of the lead embedded in the circuit card (blue in Figure 71). Since the circuit card was modeled using shell elements the nodes represented the mid-plane of the circuit card. As such, the embedded portion of the beam was modeled as half the thickness of the circuit card (0.85 mm). The second part of the lead (yellow in Figure 71) represented the exposed portion of the lead between the circuit card and the inductor body (2 mm). It was thought the embedded portion of the lead would bend very little compared to the exposed portion of the lead since the embedded portion was constrained by the card. The elastic properties for this section of the beam were crafted to be extremely stiff so elastic properties of E=150,000 MPa and v=0.3 were used. The exposed portion of the beam used standard copper isotropic elastic properties of E=118,410 MPa and v=0.3. Density for all segments of the lead was 8.9 g/cm^3. The embedded lead segment was constrained to the circuit board and the exposed lead segment. The exposed lead segment was constrained to the embedded lead segment and the inductor body bottom surface shell. For the constraint between the circuit card and the embedded lead, a multi-point constraint (MPC) was used to tie the node at the end of the embedded segment of the lead to the 12 nodes on a 0.75 mm circle on the board around the lead. The effect of this constraint was to distribute the forces from the lead to an area slightly larger than the lead rather than to a single point. Figure 72 shows the MPC. Please note the beam diameter in Figure 72 is not to proper scale in order to show the MPC. The lead in Figure 73 is shown to scale. Figure 74 shows the strain in the board due to flexure of the lead.
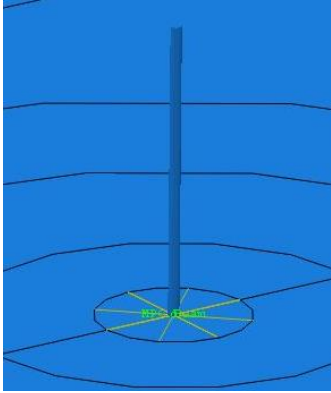
| Figure 72: Lead MPC (Lead Not to Scale) | Figure 73: Lead to Circuit Card (Proper Scale) | Figure 74: Lead to Circuit Board Strain |

Observation of the lead/board connection and lead/inductor connection led the modeler to believe there was considerable rotational compliance at both connections. Furthermore, the component construction caused one lead to be significantly stiffer than the other. In order to model these effects, it was decided that the translational DOF at the connections should be rigidly joined together, but rotational compliance should be built in. A linear torsional stiffness for each rotational DOF was used. For the embedded lead/exposed lead and exposed lead/inductor shell constraints, Abaqus' connector builder tool was used. This allowed independent relationships between all six degrees of freedom to be defined for the two nodes being connected.

Torsional spring stiffness's were estimated by experimentally determining the natural frequency of a 25.4 mm length of lead extending from the stiff side of the component, the compliant side of the component and soldered into the board. Measured values are in Table 13. A 25.4 mm lead (with accelerometer mass) was then modeled in Abaqus with a torsional spring at the boundary. Calculated natural frequencies for several boundary stiffness values are given in Table 14. Stiffness values from Table

14 corresponding to the natural frequencies in Table 13 were then used to estimate the stiffness required at each connection. Stiffness in the direction of first mode inductor bending was the main concern. Stiffness on the other rotational DOFs were of a secondary concern and were merely estimated. Stiffness orthogonal to the first mode bending was approximated as that of the stiff lead for both leads. Torsional stiffness was estimated as 10,000 for the lead/inductor connection and 100,000 for the lead/board connection. When compared to the experimental data, first mode natural frequency of the inductor was found to be slightly low using the numbers directly calculated. All stiffness values were adjusted upward by 25% in order to match the experimental natural frequency. Final values are shown in Table 15.

Table 13: Measured Natural Frequency

Location	Frequency (Hz)
Inductor Compliant Lead	97-125
Inductor Stiff Lead	160-167
Lead / Board	230

Table 14: Stiffness to Natural Frequency Correlation

Stiffness (N-mm / rad)	Frequency (Hz)
1000000	241
100000	240
10000	230
5000	220
1000	170
900	165
500	138
350	121
300	115
250	106

Table 15: Rotational Stiffness for Lead Connections

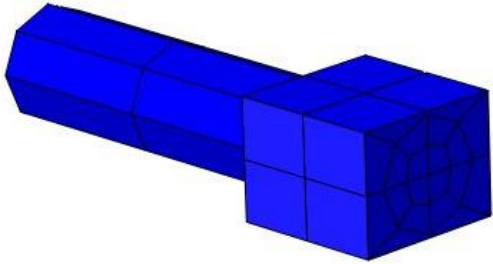|	Torsional Stiffness (N-mm / rad)		
	M1	M2	M3
Lead / Inductor Compliant Lead	1200	400	10000
Lead / Inductor Stiff Lead	1200	1200	10000
Lead / Board	10000	10000	100000

2.4 Accelerometers

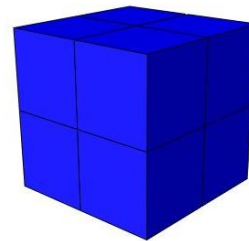**Figure 75: Dytran 3263A2T Model**

Figure 76: Dytran 3133A3 Model

Two types of accelerometers were modeled. Both aimed to mimic the proper mass and mass distribution of the accelerometer used during the test. Cables were neglected in the model. The Dytran 3263A2T (shown in Figure 75) was mounted to the circuit card in two places. The Dytran 3133A3 (shown in Figure 76) was mounted on top of two of the inductors. The mass of the inductors was uniformly distributed over the accelerometer volume. The Dytran 3263A2T was modeled with a density of 0.169 g/cm^3 while the A3133A3 was modeled with a density of 0.370 g/cm^3. Both were modeled with C3D8R elements.

3 Boundary Conditions
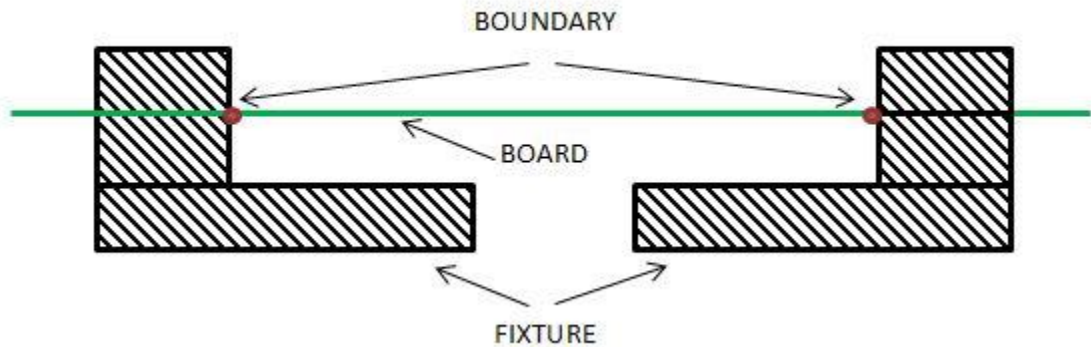
3.1 Initial (Static) Boundary Condition

Figure 77: Boundary Location

Figure 78: Boundary Rotation

The boundary was modeled at the point where the circuit card contacted the fixture as shown in Figure 77. At this point, the fixture attempts to form a perfect clamped condition, however some flexibility is still allowed. In order to model this condition, acceleration on all DOFs along the boundary was fixed at zero except for the rotational DOF whose axis parallels the fixed edge of the card as shown in Figure 78. As a boundary it was left free to rotate; however, within the interaction module a linear rotational spring connected to 'ground' was defined on this DOF at each node on the boundary. This stiffness was adjusted in order to create a good first and second mode natural frequency match between the model and experiment. 3000 N-mm/rad was found to produce the best match. This connector was applied

individually to all 50 nodes on the boundary. Figure 79 depicts the 25 boundary
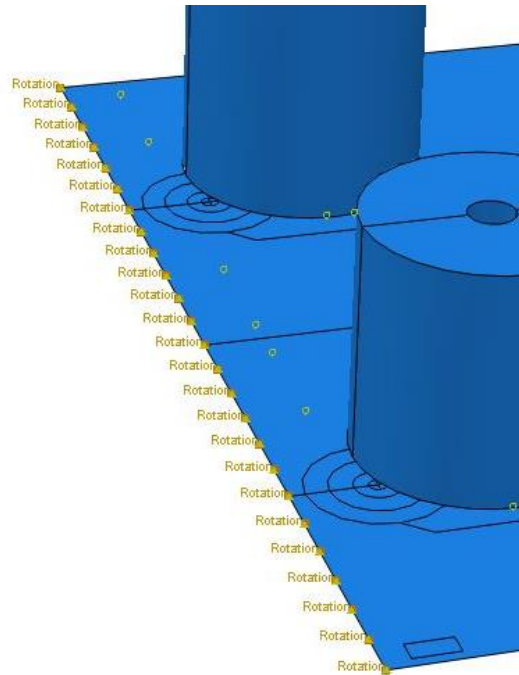
constraints on one of the boundaries.

Figure 79: Boundary Constraints

3.2 Dynamic Boundary Condition

For the dynamic analysis, motion for all boundary nodes was defined by an

acceleration amplitude history for the activated DOF. For example, if out-of-plane

vibration was desired, X and Y translation would have 0 acceleration while the Z

degree of freedom would have an acceleration amplitude history specified. The

amplitude history is created in the Abaqus amplitude manager. It can be specified in

a number of ways. In order to create a random vibration on the boundary, a tabular

type must be used. Appendix D gives details on the creation of a random time history

with the desired characteristics. Figure 80 shows an example Abaqus amplitude

specification. The first 100 points of this amplitude are plotted in Figure 82. The

amplitude must be longer than the time period of the simulation.   Figure 81 shows

the specification for a Z axis (out-of-plane) random vibration. Notice the AR2 and

AR3 angular accelerations are defined as 0 to fix the boundary in these rotations.

AR1 is not defined. This rotation is constrained within the interaction module as a

linear torsional spring accounting some flexibility in the fixture. Since this boundary

condition is for out-of-plane motion, A1 and A2 were fixed by defining 0 acceleration

on those DOF. A3 is the desired random vibration. A value of 9810 is used to

convert the 'zaxis-z-a-filter' amplitude from g units to mm/s^2 units. The amplitude

specified at the bottom is the time history. If vibration conditions on two or more

axes are required, multiple boundary conditions will be needed so that different

amplitudes can be used. If a DOF is defined by a separate BC, that DOF must be
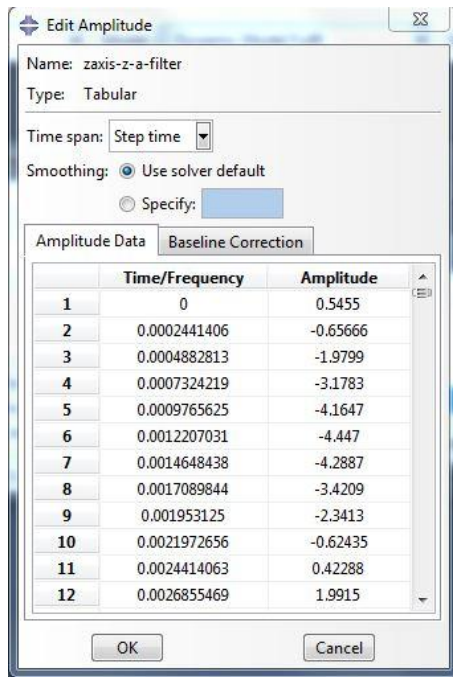
unchecked in other BC specifications.

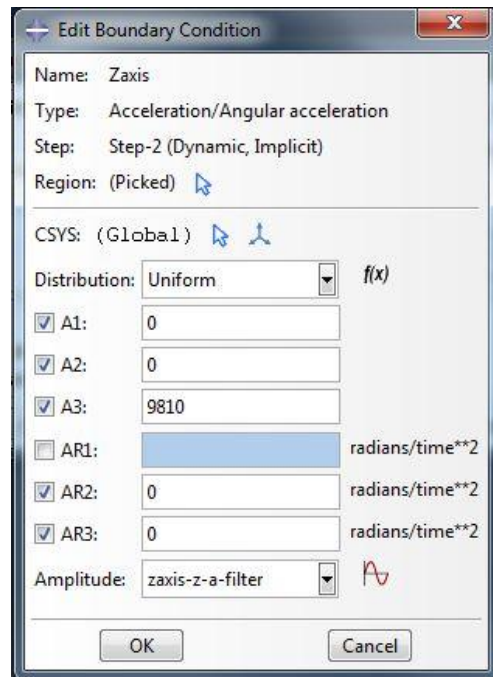**Figure 80: Tabular Amplitude Specification**

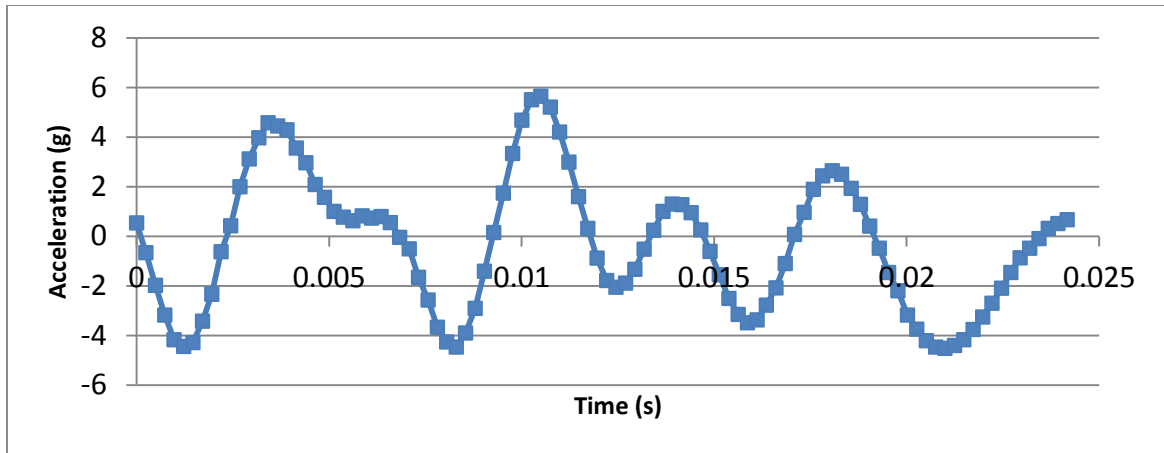**Figure 81: Boundary Condition Specification**

Figure 82: First 100 Points in 'zaxis-z-a-filter' Amplitude

4 Analysis Procedure

This model used two different analysis procedures within the step module. The linear perturbation frequency procedure was used to extract natural frequencies and modes shapes. The dynamic-implicit procedure was used for the time-domain dynamic analysis. Automatic increment size may be used for the dynamic-implicit procedure; however, a maximum increment size should be specified. If no maximum is specified, the solver may allow increments with a time step large enough to clip the peaks of the boundary acceleration. Figure 83 shows the effect of peak amplitude clipping if larger time steps are used. As a general rule I ensured at least 10 time steps were used per cycle at the highest input frequency. Since 320 Hz was the top of the durability profile, a maximum time step of 3.125E-4 s was required. I used a time step of 2.4414E-4 s (4096 Hz) since this was the time step which defined the amplitude history. In this way Abaqus would directly use the values from the history rather than linearly interpolating between values.
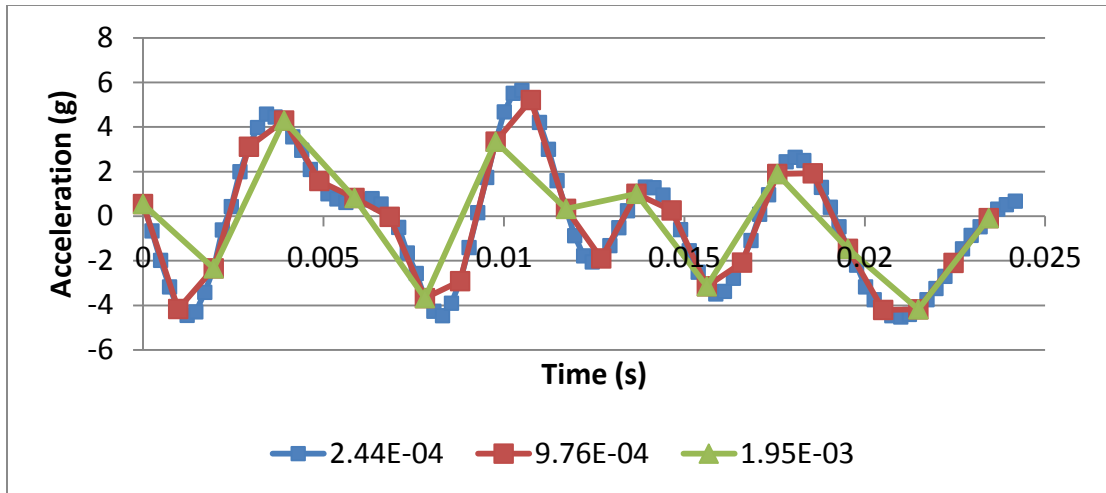
Appendix G-13

Figure 83: Amplitude Clipping with Large Time Steps

5 Conclusions

Table 16 compares the experimentally measured natural frequencies to those derived from the FEA model. The experimentally derived natural frequencies were a primary agent used to calibrate the FEA model.

Table 16: Natural Frequency Comparison

	Experiment	FEA Model
Mode IA (Component 1)	80.0	80.8
Mode IB (Component 5)	82.0	82.0
Mode II (Board 1st Mode)	176.0	175.9
Mode III (Board 2nd Mode)	214.0	216.5

When boundary acceleration was derived from experimental data (i.e. table acceleration) very good agreement was found between the experimentally measured board response and FEA calculated board response. As an example, Figure 84 shows the first 0.1s of acceleration at the center of the board as measured during the experimental characterization and through FEA. The FEA model captures most of the low frequency motion of the card (near the first mode frequency), but fails to

Appendix G-14

capture the high frequency motion detected by the accelerometer during the
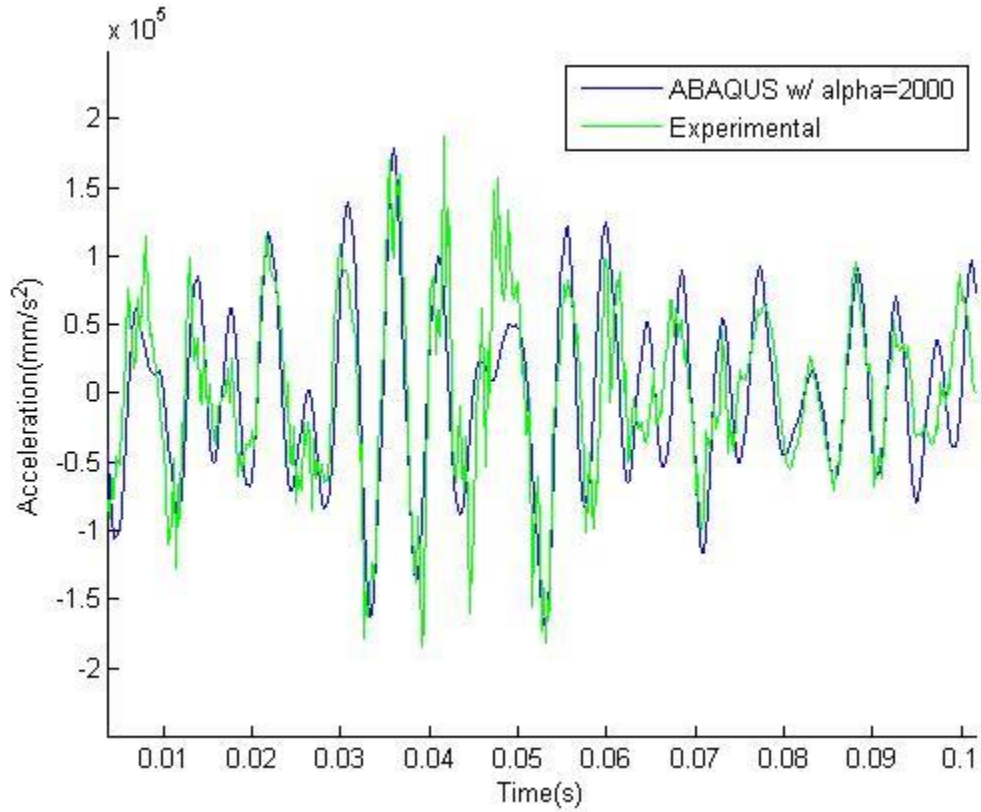
experiment.

Figure 84: FEA and Experimental Board Response

Work was terminated on this model before completion. In order to complete this

global model, a proper damping value for the inductor would need to be determined.

This could be accomplished by adjusting the α-value for the inductor material until

FEA component response amplitude approximately matched experimental component

response amplitude. Revisions to the board damping may be necessary if inductor

damping deviated significantly from the assumed value used when determining the

board damping.

Bibliography

[1] Department of Defense Test Method Standard, "MIL-STD-810G, Environmental Engineering Considerations and Laboratory Tests," 2008.

[2] IEEE Power Engineering Society. Nuclear Power Engineering Committee; IEEE Standards Board, IEEE-344, IEEE Recommended Practice for Seismic Qualification of Class 1E Equipment for Nuclear Power Generating Stations, New York: Institute of Electrical and Electronics Engineers, 2004.

[3] SAE Technical Standards Board, SAE J1211, Handbook for Robustness Validation of Automotive Electrical/Electronic Modules, Warrendale, PA: SAE International, 2009.

[4] SAE Technical Standards Board, SAE J2837, Environmental Conditions and Design Practices for Automotive Electronic Equipment: Reference Data from J1211 Nove 1978, Warrendale, PA: SAE International, 2009.

[5] International Organization for Standardization, ISO 16750, Road Vehicles - Environmental Conditions and Testing for Electrical and Electronic Equipment, Geneva, Switzerland: International Organization for Standardization, 2003.

[6] U.S. Navy, "NAVMAT P-9492, Navy Manufacturing Screening Program," 1979, pp. 9-14, 16.

[7] E. Habtour, Drake, G.S, Dasgupta, A., Al-Bassyiouni, M. and Choi, C., "Improved Reliability Testing with Multiaxial Electrodynamics Vibration," in *Proceedings of the Annual Reliability and Maintainability Symposium*, Jan. 2010.

[8] C. Choi, M. Al Bassyiouni, Dasgupta, A. and Osterman, M., "PoF Issues in Multi-DoF Vibration Testing: ED Shakers and RS Shakers," in *IEEE ASTR09 Workshop*, New Jersey, Oct 2009.

[9] D. Smallwood and D. Gregory, "Evaluation of a Six-DOF Electrodynamic Shaker System," in *Proceedings of the 79th Shock and Vibration Symposium*, Orlando, FL, 2008.

[10] H. Himelblau, M. Hine, A. Frydman and P. Barrett, "Effects of Triaxial and Uniaxial Random Excitation on the Vibration Response and Fatigue Damage of Typical Spacecraft Hardware," in *Proceedings of the 66th Shock and Vibration Symposium, SAVIAC*, Arlington, VA, 1995.

[11] W. Whiteman and Berman, M.B., "Fatigue Failure Results for Multiaxial Versus Uniaxial Stress Screen Vibration Testing," *Journal of Shock and Vibration,* vol. 9, pp. 319-328, 2002.

[12] R. French, Handy, R. and Cooper, H.L., "A Comparison of Simultaneous and Sequential Single-Axis Durability Testing," *Experimental Techniques,* pp. 1-6, September-October 2006.

[13] D. Gregory, F. Bitsie and D. Smallwood, "Comparison of the Response of a Simple Structure to Single Axis and Multiple Axis Random Vibration Inputs," 2009.

[14] E. Habtour, Choi, C., Osterman, M. and Dasgupta, A., "Novel Approach to Improve Electronics Reliability in the Next Generation of US Army Small Unmanned Ground Vehicles Under Complex Vibration Conditions," *Journal of Failure Analysis and Prevention,* pp. 86-95, 2012.

[15] M. Aykan and Çelik, M., "Vibration fatigue analysis and multi-axial effect in testing of aerospace structures," *Mechanical Systems and Signal Processing,* vol. 23, pp. 897-907, 2009.

[16] TEAM Corporation, "TE6-900 Data Sheet," June 2010. [Online]. Available: http://www.teamcorporation.com/documents/brochures/Tensor%20TE6-900.pdf. [Accessed 14 January 2013].

[17] E. Habtour, "Time-to-Failure Results for CALCE C11-02 Project," Unpublished raw data, 2011.

[18] L. Meirovitch, Fundamentals of Vibrations, New York: McGraw-Hill, 2001.

[19] R. L. Barnoski, "Response of Elastic Structures to Deterministic and Random Vibration," Air Force Flight Dynamics Laboratory, Wright-Patterson AFB, OH, 1965.

[20] B. Lent, "Practical Considerations of Accelerometer Noise," 2007.

[21] A. Halfpenny, "A Frequency Domain Approach for Fatigue Life Estimation from Finite Element Analysis," in *International Conference on Damage Assessment of Structures*, Dublin, 1999.

[22] M. Ernst, C. Choi and A. Dasgupta, "Computational Strategies to Minimize Transient Response During Time-Domain Analysis of Structures Under Vibratory Loading," accepted by *Proceedings of the ASME 2013 International Technical Conference and Exhibition of Packaging and Integration of Electronic and Photonic Microsystems*, Berlingame, CA, 2013.

[23] Dassault Systems Simulia Corp., "Abaqus/CAE 6.10-EF User's Manual," Dassault Systems, Providence R.I., 2010.

[24] S. Douglas, "High Accelerations Produced through Secondary Impact and its Effect on Reliability of Printed Wiring Assemblies," Master's Thesis; Department of Mechanical Engineering, University of Maryland, College Park, MD, 2010.